ULTRASOUND TISSUE DISPLACEMENT AND TISSUE ELASTICITY IMAGING

BY

ERIC CHUNG JAY CHEN

B.S., University of Illinois, 1990
M.S., University of Illinois, 1992

THESIS

Submitted in partial fulfillment of the requirements
for the degree of Doctor of Philosophy in Electrical Engineering
in the Graduate College of the
University of Illinois at Urbana-Champaign, 1995

Urbana, Illinois

UNIVERSITY OF ILLINOIS AT URBANA-CHAMPAIGN

THE GRADUATE COLLEGE

JULY 1995

WE HEREBY RECOMMEND THAT THE THESIS BY

ERIC CHUNG JAY CHEN

ENTITLED ULTRASOUND TISSUE DISPLACEMENT AND TISSUE ELASTICITY IMAGING

BE ACCEPTED IN PARTIAL FULFILLMENT OF THE REQUIREMENTS FOR

THE DEGREE OF DOCTOR OF PHILOSOPHY

W. O'Brien
Director of Thesis Research

Timothy N. Pratt
Head of Department

Committee on Final Examination†

W. O'Brien
Chairperson

W. K. Jenkins

Anton Cetin

Leon A. Frizzell

† Required for doctor's degree but not for master's.

O-517

ULTRASOUND TISSUE DISPLACEMENT AND
TISSUE ELASTICITY IMAGING

Eric Chung Jay Chen, Ph.D.
Department of Electrical and Computer Engineering
University of Illinois at Urbana-Champaign, 1995
W. Kenneth Jenkins and W.D. O'Brien, Jr., Advisors

In this dissertation, we investigate the feasibility of using high frequency ultrasound, to measure tissue motion and tissue elasticity for medical imaging applications. Ultrasound provides a means for non-invasive imaging of soft tissues, providing soft tissue contrast that can not be achieved using conventional X-ray or tomographic imaging.

A two-dimensional correlation search algorithm is used to track local tissue displacements from radio frequency (RF) ultrasound echoes and from digitized ultrasound images. The accuracy of displacement imaging is investigated as a function of various imaging parameters such as ultrasound frequency and target size.

Ultrasound elasticity imaging consists of three basic steps: 1) measurement of tissue displacement, 2) estimation of tissue stresses and strains, and 3) recovery of tissue elasticity. Tissue strains and tissue elasticities are obtained from reconstructed tissue displacement fields and experimental measurements of applied stresses. Ultrasound elasticity measurements were compared with independent Instron load cell elasticity measurements.

Several examples of tissue displacement imaging of breast tumors in human breast cancer patients and ultrasound elasticity measurements of tissue phantoms (soft gels), and samples of bovine muscle and fat tissue are provided.

ACKNOWLEDGMENTS

Special acknowledgment to Dr. Ron Adler who helped tremendously with acquisition of clinical data and provided useful suggestions. He provided access to high quality clinical data and answered many questions via e-mail from the department of Radiology at the University of Michigan hospital.

Thanks to Dr. Paul Carson and Professor Jan Novakofski for help in collecting clinical ultrasound and Instron data and for many helpful suggestions on manuscripts.

Thanks to my co-advisor Professor Jenkins for giving me the opportunity to work with him on an undergraduate honors project, in the computer lab and on publishing papers. Thanks to my advisor Professor O'Brien for giving me many important opportunities: IEEE conference presentations, grant proposals, journal reviews and social events.

I also thank my colleagues in the Bioacoustics Research Laboratory and in the Digital Signal Processing Laboratory their help and encouragement.

Generous financial support was provided by the National Institutes of Health (NIH) through the Radiation Oncology Training Program (ROT)

TABLE OF CONTENTS

LIST OF TABLES

LIST OF FIGURES

CHAPTER 1

INTRODUCTION

In this chapter we describe several potential medical and industrial applications of elasticity imaging. In addition, the forward and inverse problems in elasticity imaging are defined, and the inverse problem to be solved in ultrasound elasticity imaging is formulated.

1.1 Significance

The ability to image tissue motion and tissue elasticity is of great diagnostic value. The turbulent flow of fluid tissues, such as blood through an artery, can provide important clues in detecting intravascular plaque buildup and in monitoring the development of atherschlerosis and coronary heart disease [1]. Invasion of normal tissues by malignant cancer, such as schirrous carcinoma of the breast, can result in the formation of stone hard tumors, with much stiffer elasticities than normal tissues [2, 3, 4]. The capability to image tissue motion and differences in tissue elasticity thus provides extremely useful clinical information that is **currently not attainable by any other means.**

Information on tissue elastic properties, in particular, also has tremendous potential for commerical applications in the giant food science and health care sectors. Almost every major technical journal on food science contains articles on food texture or tenderness. Fundamental tests to measure material properties of food often consist of punch or shear tests or axial compressions [5, 6]. Many food texture parameters such as springiness, hardness, cohesiveness or fracturability are strongly related to tissue elastic properties [7, 8]. Objective quantitative measurements of food mechanical properties are of the utmost interest to the food science industry. Food manufacturers are extremely interested in studying the correlation between objective measurements of food mechanical properties and parameters from consumer taste panels such as tenderness, juiciness and

cohesion, important parameters that are typically used to describe the sensory perception of taste.

Objective measurements of food mechanical properties are also of interest in maintaining proper food quality control and in assessing the viability of new foodstuffs. Development of objective quantitative measurements of food mechanical properties is critical to the establishment of standardized rating scales that would allow subjective sensory perception and taste of foods to be quantified in a systematic manner and is considered one of the most important problems in the food technology industry. As a specific example, food elasticity is generally considered to be correlated to the sensory attributes of chewiness, tenderness and hardness with correlation values ranging from approximately 0.40 to 0.70 [6, 8, 9]. Many devices have been developed in the meat science industry to measure meat tenderness. Recent studies indicate that ultrasound image texture and tissue elasticity measurements could form the basis for a new USDA grading system, which is currently based on marbling fat [10, 11, 12].

Changes in tissue elasticity are often strongly correlated to the onset of tissue pathology or disease. This makes tissue elasticity information extremely useful for early detection of cancer, coronary heart disease and liver cirrhosis. Some cancers such as scirrhous carcinomas of the breast, for example, appear as extremely hard nodules, while fluid filled cysts can be much softer than surrounding tissues [4]. Ultrasound imaging of tissue elasticities would provide a non-invasive and relatively inexpensive means for early detection of such cancers [2].

The consistency of the uterine cervix is of great interest in obstetrics and gynecology. In pregnancy the uterine cervix is softer than in the non-pregnant state. To date, only inexact and bulky analog mechanical instruments have been proposed to measure tissue fibroelasticity [13]. Atherosclerosis and other vascular diseases are characterized by the accumulation of plaque in arteries, which can lead to vessel occlusion, increased strain on the heart and the development of serious coronary conditions. Plaque buildup can also lead to dramatic changes in the elastic properties of arterial walls. Constitutive relations

for the human aorta have been studied; the development of high-frequency intravascular imaging probes would allow arterial wall elasticity to be measured [1, 14].

Changes in arterial wall mechanical properties are also believed to be linked to hypertension. A decrease in the radii of arteries is characteristic of hypertension and is believed to be related to arterial wall stiffness [15]. Development of artificial heart and vascular prostheses also requires a comprehensive understanding of intravascular elastic properties. Knowledge of lung elastic properties are extremely useful in the understanding of the mechanics of breathing. Lung tissue distortion and non-uniform distribution of pleural surface pressure may be caused by the shape of the lungs and chest wall. Pressure-volume (PV) curves and spirometric tests are current standard methods of characterizing the stress-strain relations of the lung [16, 17].

Tissue elasticity information is also valuable in treating subcutaneous edema, a disease of the skin where swollen tissues are known to lose elasticity [18], in cirrhosis of the liver which can significantly reduce liver elasticity, and in viscoelastic stress and load analysis of human articular cartilage since the measured compliance for normal and degenerate cartilage has been found to be significantly different [19]. Considering the prospective size of consumer and patient populations, the potential diagnostic and commercial value of tissue elasticity imaging is both extensive and immense.

1.2 Motivation

Ultrasound provides a relatively inexpensive, safe and non-invasive method of imaging patients in real-time without the use of ionizing radiation. There are no known bioeffects in humans due to diagnostic ultrasound imaging [20, 21, 22]. Ultrasound video images can typically be acquired in a few seconds, compared with imaging times on the order of 30 minutes for magnetic resonance imaging (MRI) or computed tomography (CT). Diagnostic ultrasound imaging is non-invasive and does not require injection of radioactive dyes or contrast agents or insertion of catheters. The newest top-of-the-line ultrasound imaging systems currently cost on the order of $200,000 - $300,000, and most standard ultrasound exams can be performed at a cost of less than $100-$500 to the

patient [23, 24]. The cost of most MRI systems starts in the range of 1-2 million dollars with costs to the patient on the order of $500-$1000 per scan [23, 25]. Because of the relatively low cost and short acquisition time of ultrasound compared with MRI, CT and other imaging modalities, ultrasound imaging equipment and facilities are available at nearly every hospital. Diagnostic ultrasound imaging is performed without subjecting the patient to harmful ionizing radiation or x-rays.

1.3 Scope

Ophir et al. [4] have proposed a new technique, termed elastography, for imaging the elasticity of soft tissues. One-dimensional longitudinal strain distributions are reconstructed from cross-correlation analysis of received ultrasound RF A-line echoes acquired before and after the tissue is compressed. Two-dimensional strain images are generated by repeating one-dimensional measurements at several different lateral positions over the tissue. Elastograms, or images of tissue elastic moduli, are formed by combining information about tissue strain distributions with experimental or theoretical tissue stress distributions.

O'Donnell et al. [3] have proposed a more complicated two-dimensional model which estimates both longitudinal and shear components of stress and strain. A Fourier speckle tracking technique is used to estimate local tissue displacements. Two-dimensional elasticity distributions are then produced from finite element analysis of tissue displacements and initial boundary conditions. Parker et al. [26] and Lerner et al. [27] have proposed a technique called sonoelasticity, where soft tissues are vibrated instead of compressed. Sonoelasticity employs the idea of inducing oscillations in tissue using a vibrating external source. The resulting frequency response of tissues is converted into images of tissue stiffness or elasticity using conventional color Doppler techniques [28, 29].

Tissue displacement distributions for a given applied stress, can be computed theoretically by solving the forward problem. That is, given the elasticity distribution of the tissue and knowledge of the applied stress field, we compute the resulting tissue displacement field or tissue strain field. The tissue strain field is obtained from the derivative

of the tissue displacement field. In this case, the elasticity and stress distributions are the known quantities and the strain and thus displacement distribution (field) are the unknowns.

To produce images of tissue elasticity, the elasticity distribution of the tissue must be computed by solving the inverse problem. In this case, the tissue strain field due to a known applied stress is measured experimentally. For the inverse problem, the stress and strain distributions (fields) are known (or estimated) and the tissue elasticity distribution is the unknown. Experimental solution of the inverse problem consists of essentially three steps:

- Ultrasonic measurement of tissue displacement.
- Estimation of tissue stress and strain distributions.
- Estimation of tissue elasticity distribution.

In the present study, a correlation search algorithm is used to measure tissue motion in two scenarios: tissue displacement imaging of breast tumors in human patients and ultrasound elasticity imaging of tissue phantoms and of muscle and fat tissue samples. One- and two-dimensional tissue displacement fields are computed from correlation analysis of ultrasound RF echoes and from frame to frame correlation of ultrasound video images. Tissue strain distributions are estimated from the gradient of tissue displacement fields. Tissue stress distributions are measured experimentally using a computer-controlled compressing device and a scale. The Young's modulus of elasticity of tissue samples is estimated by comparing stress and strain values, at several different applied stress levels. The accuracy of displacement imaging is investigated as a function of various imaging parameters in calibrated tracking measurements. The accuracy of elasticity measurements is established under controlled test conditions using an Instron load cell device, Daedal computer-controlled positioning system, and ultrasound tissue equivalent phantoms.

CHAPTER 2

ULTRASOUND TISSUE DISPLACEMENT IMAGING

In this chapter we describe an ultrasound correlation search algorithm used to measure tissue motion. Motion can be decomposed into three major components: 1) translation, 2) rotation and 3) deformation. The correlation search algorithm and a hybrid correlation search algorithm described in this chapter are used to track translational and rotational motions. Deformations are discussed in Chapter 4. This chapter discusses three important topics: 1) a cross-correlation motion tracking algorithm, 2) an incremental tracking strategy used to improve tracking accuracy, and 3) an algorithm for tracking limited rotational motion.

2.1 Fundamentals of Ultrasound Imaging

Ultrasound is very high frequency sound. Ultra means extreme, and sound is mechanical radiant energy that is transmitted by longitudinal pressure waves in water or air (in some cases there may be shear waves as well). In diagnostic imaging, acoustic pressure or sound waves are transmitted in the frequency range of 1-10 MHz. In biological tissues, the speed of sound is typically on the order of 1540 m/s [30], resulting in a wavelength of approximately 0.1-1.0 mm. This is typically the upper limit of resolution seen in most ultrasound imaging systems. Diagnostic ultrasound images typically suffer from a noise phenomenon known as speckle. Speckle in ultrasound images is seen in the form of a granular textured pattern and results from scattering of the ultrasound wave as it propagates through tissue. Speckle noise is also seen in optical and laser imaging systems. In addition, the signal to noise ratio (SNR) in ultrasound images is often relatively low due to attenuation of the signal as it passes through lossy tissues and to speckle noise.

Medical ultrasound provides a useful tool for imaging different types soft tissues. While conventional X-ray images are useful in imaging the location of bones inside tissue, they are not capable of differentiating between different types of soft tissues such as

muscle, fat and liver. The principle of X-ray attenuation is used to produce contrast in most X-ray and computed tomography images. X-ray and CT images are essentially spatial maps of X-ray attenuation. The contrast mechanism in medical ultrasound is acoustic impedance which depends on tissue density and speed of sound. For soft tissues with comparable densities, ultrasound images can be roughly thought of as spatial maps of the speed of sound. A significant problem in imaging malignant breast cancers and soft tissue tumors is that in many cases, the tumor area will often not have a significantly different (X-ray) attenuation or speed of sound than the surrounding tissue. However, it is known that many cancers, such as scirrhus carcinoma of the breast, produce tumors with a much different **elasticity** than the surrounding tissue [31]. In fact, differences in elasticity between breast cancers and normal tissue may span **several orders of magnitude**, producing immense dynamic range and contrast, which increases the margin for error in ultrasound tissue elasticity estimates [3, 32].

2.2 One-Dimensional Ultrasound Displacement Imaging

Ultrasound can be used to non-invasively measure tissue motion [11, 33]. Tissue motion could be the flow of blood through an artery or the movement of lung or chest wall motion due to the beating of the heart. There are two primary methods of detecting tissue motion using ultrasound. These include Doppler and correlation based techniques [34]. In Doppler ultrasound a sinusoidal, high frequency ultrasound wave is modulated onto a radio-frequency (RF) carrier and transmitted towards the target tissue. The frequency shift in the received signal can be used with knowledge of the speed of sound and Doppler angle to estimate the displacement or velocity of the target. Doppler techniques suffer from several limitations. These include problems estimating the Doppler angle, aliasing and the ability to measure only the component of velocity in the direction of the ultrasound beam.

To avoid these problems a time-domain correlation technique is used to measure tissue motion. The accuracy of the correlation technique to track tissue displacements has previously been established [35, 36]. To estimate tissue displacement, two ultrasound

echoes are acquired sequentially from a moving target. To track the displacement of the tissue inside a particular range gate, a portion of the first echo signal, corresponding to the tissue of interest, is selected or windowed out from the first ultrasound echo. The windowed signal is compared with identically sized template regions (windows) in the second echo. The location of the template inside the second echo producing the best match is used to determine the displacement and velocity of the tissue of interest. A normalized correlation coefficient is used as a measure of similarity.

2.2.1 Correlation coefficient

The correlation coefficient provides a measure of the similarity between two variables or sets of data [37]. The correlation coefficient values are limited to the range of -1.0 to 1.0. A correlation coefficient value of 1.0 or -1.0 means that the two variables are linearly dependent (the data in the two windows are related by a constant). Positive correlation values indicate that there is a positive linear relation between the two variables (if one variables increases, so does the other), while negative correlation values indicate a negative linear relationship between the variables (as one variable increases the other variable decreases). Correlation values near 0.0 indicate little or no relation between the two variables.

If x and y represent two variables or windows of data, then a normalized correlation between the two variables can be computed according to Equation (2.1) [38, 39].

$$\rho_{xy} = \frac{Cov(x,y)}{\sqrt{Var(x)Var(y)}} \tag{2.1}$$

Here the covariance function represents the correlation or degree of linear relatedness between the variables x and y with the mean values first subtracted, while the variance functions normalize the result to have amplitude less than or equal to 1.0. The covariance

and variance functions are defined in Equations (2.2) and (2.3).

$$Cov(x,y) = E[(x-\bar{x})(y-\bar{y})] \tag{2.2}$$

$$Var(x) = E[(x-\bar{x})^2] \tag{2.3}$$

where x, y and $\bar{x}$, $\bar{y}$ are two variables and their mean values, respectively.

If x, y are two different ultrasound echoes, then the discrete version of the correlation coefficient, shown in Equation (2.4), can be used [40]. That is,

$$\rho_{xy}(k) = \frac{\sum_{i=1}^{M}(x(i)-\bar{x})(y(i+k)-\bar{y})}{\sqrt{\sum_{i=1}^{M}(x(i)-\bar{x})^2 \sum_{i=1}^{M}(y(i+k)-\bar{y})^2}} \tag{2.4}$$

where $x(i), y(i)$ represent two M length windows of data in the ultrasound echoes x, y, k represents the position of the template inside the second echo, and $\bar{x}, \bar{y}$ are the mean amplitude values in the windows $x(i), y(i)$.

2.3 Two-Dimensional Ultrasound Displacement Imaging

Two-dimensional ultrasonic imaging of tissue motion using cross-correlation is sometimes called speckle tracking, although the concepts remain the same as for the one-dimensional case. Two-dimensional speckle tracking algorithms estimate tissue motion by comparing speckle patterns in serially acquired ultrasonic images. The speckle patterns are used as landmarks or registration points to determine relative motion. To estimate local tissue displacement, a window of data corresponding to the tissue region of interest (ROI) is selected from an initial ultrasound image. This window of data is compared with identically sized windows of data (templates) in a successive ultrasound image until a best match is found. The position of the window in the initial scan and the position of the best match window in the successive scan are used to compute a two-dimensional displacement vector representing the net displacement of the ROI. In this

manner, the velocity of tissue motion can also be determined if the elapsed time between scans is known.

The correlation coefficient is used to determine the best match. If x and y are two different images then the discrete version of the correlation coefficient, shown in Equation (2.5) can be used [39].

$$\rho_{xy}(k,l) = \frac{\sum_{i=1}^{M}\sum_{j=1}^{N}(x(i,j)-\bar{x})(y(i+k,j+l)-\bar{y})}{\sqrt{\sum_{i=1}^{M}\sum_{j=1}^{N}(x(i,j)-\bar{x})^2 \sum_{i=1}^{M}\sum_{j=1}^{N}(y(i+k,j+l)-\bar{y})^2}} \tag{2.5}$$

Here $x(i,j), y(i,j)$ represent two M $\times$ N windows of data in the ultrasound images x, y, the variables (k,l) represent the pixel coordinates of the template region in the second image and $\bar{x}, \bar{y}$ are the mean pixel values in the windows x, y.

2.4 Incremental Tracking

The accuracy of tissue speckle tracking relies heavily on the assumption that tissue samples produce speckle patterns that do not significantly change as the tissue is translated. The tracking of local tissue motion is valid only to the extent that the speckle patterns or landmarks being used remain constant. However, it is known that the speckle patterns in high frequency ultrasound images decorrelate or change as tissue translations are increased [41]. Decorrelation of speckle patterns can result in significant errors in tissue speckle tracking [42, 43].

To minimize speckle pattern decorrelation, we have adopted an incremental tracking strategy [42]. Using this strategy, tissue regions are tracked incrementally over short distances. The incremental displacements can then be summed to compute a large net tissue displacement. Using this tracking strategy, tissue regions can be tracked over larger distances and the problem of speckle pattern decorrelation can be reduced.

As a specific example, suppose it is desired to track a particular tissue region on videotape data over a displacement on the order of 5.0 mm. It is known that tissue speckle patterns show signs of decorrelation for tissue displacements as small as 1.0 mm or less [41,

42, 43]. Instead of acquiring video frames of the tissue region before and after the 5.0 mm displacement, where the tissue speckle patterns have already undergone significant decorrelation, a number of intermediate frames are acquired. The displacement of the tissue region can then be incrementally tracked over smaller displacements and summed to produce an estimate of the net displacement. Assuming three intermediate frames were acquired, then the incremental displacements might be on the order of 1.0 mm, effectively reducing tracking errors due to speckle pattern decorrelation. This approach assumes that acquiring intermediate data is feasible. We have found that this is normally the case when using video data since commercial frame-grabbing systems can digitize video data at a rate of 30 frames per second.

2.5 Accuracy of Motion Tracking

The accuracy of ultrasound tissue motion tracking has been investigated with calibrated motion experiments using a high precision, computer-controlled positioning system and tissue mimicking sponges. To simulate axial and lateral tissue motions, an ultrasound imaging transducer (ATL 5.0 MHz, 742A ATL servo-controlled rotary system) was translated using a high precision Daedal motorized positioning system (precision of 1 μm for axial and lateral motions). The Daedal system was used to simulate five types of translational and rotational motions. The positioning system is computer controlled and has five degrees of freedom, three translational and two rotational. Serial frames of tissue motion were digitized using a Targa-16 frame grabbing system. The results of this study indicate that regions as small as 1.0 mm $\times$ 1.0 mm can be tracked with less than 4% error for displacement distances up to 2.0 mm. In addition, the test tracking experiments further demonstrate significant improvement in tissue motion tracking using the incremental tracking strategy compared with those for conventional tracking methods. A 'C' program was written to implement frame-to-frame correlation tracking of tissue motion. Using incremental tracking, 1.0 cm $\times$ 1.0 cm ROIs were tracked over distances exceeding 10 wavelengths ($\lambda \simeq 1.0\ mm$) with approximately 20% relative tracking error

compared with an over 250% relative tracking error for conventional net tracking of tissue motion. The results of this study have been published in two conference papers [35, 39].

The impact of six important imaging parameters on the accuracy of two-dimensional tissue speckle tracking have been investigated in depth by Chen et al. and Ramamurthy et al. [42, 43]. These parameters include

- magnitude of tissue motion
- direction (axial or lateral) of tissue motion
- dimensions of tissue region being tracked
- ultrasonic frequency of interrogation
- digital sampling frequency
- signal type (ultrasonic RF or envelope detected)

Of particular interest was the effect of various tissues on speckle tracking. The speckle characteristics and internal morphology of various tissues alter the performance of speckle tracking in liver, muscle and fat tissues. In addition, the presence or absence of resolvable internal structures also affected speckle tracking performance.

The performance of tissue speckle tracking was investigated using porcine liver, muscle, fat and woolen sea sponge samples in calibrated tissue tracking measurements. The two-dimensional performance of tissue speckle tracking was quantified in each of the four tissue types for tracking in the axial and lateral directions and for ROIs of various dimensions. Tissue motion tracking performance was best in comparatively heterogeneous tissues such as muscle and worst in homogeneous tissue such as liver. These results are further discussed in Chapter 3. The impact of various important imaging parameters on tissue motion tracking accuracy was recently published in [42].

2.6 Rotational Motion Tracking

This section describes a rotational correlation search algorithm used to track rotational motion in 1) a calibrated phantom, and 2) clinical data from a breast tumor patient. Several different algorithms including optical flow techniques have been studied for tracking rotational motions. A number of these are reviewed in [44].

2.6.1 Rotational correlation search algorithm

To track rotational motion an ROI is selected from an initial ultrasound image (image A). The ROI is assumed to rotate through an angle θ, after which a second image is acquired (image B). Our goal is to estimate the angle of rotation θ.

The rotational correlation search algorithm consists of four steps:

1. Two windows of data (W_1 and W_2), corresponding to the ROI before and after rotation are selected from image A and image B.

2. W_1 is rotated in 1.0 degree increments to produce rotated versions of itself W_ϕ.

3. After each 1.0 degree rotation, a correlation coefficient is computed between W_ϕ and W_2 .

4. The angle ϕ, producing the maximum correlation coefficient, is assumed to be the rotation angle θ.

In other words, the ROI W_1 is rotated through a series of angles ϕ and at each angle, a correlation coefficient $\rho(\phi)$, is computed between W_ϕ and the reference W_2. The assumption that the ROI position before and after rotation is provided (step 1) is one of the limitations of this algorithm. Step 2 is achieved by rotating the rectangular coordinates of each of the matrix values of W, by the angle ϕ, and then applying a nearest neighbor interpolation. W_ϕ is therefore obtained by geometrically rotating W about its center, and then resampling at the original grid points. For points that do not fall exactly on the original grid points after rotation, the value of the nearest neighboring pixel is

used. After rotation, pixels dropping out of the image due to the rotation (particularly pixels near the corners) that need to be replaced by pixels rotating into the image are assigned values of 0 intensity. A major difficulty is that by assigning unknown pixels along the image periphery a 0 intensity, causes an image cropping effect (Fig. 2.1).

The effect of the image cropping is to reduce the correlation coefficient for any given rotation, depending on the degree of image cropping, since pixels containing 0 intensity will not contribute to the sum in Equation (2.5).

To remove this effect completely, the window W_1 is selected from image A, using dimensions 150% the size of the original ROI (step 1). After rotation (step 2), the oversized (150%) image is reduced back to the original ROI dimensions (step 2b). This eliminates the image cropping problem, since the 0 intensity pixels along the periphery of the 150% image are actually unneeded.

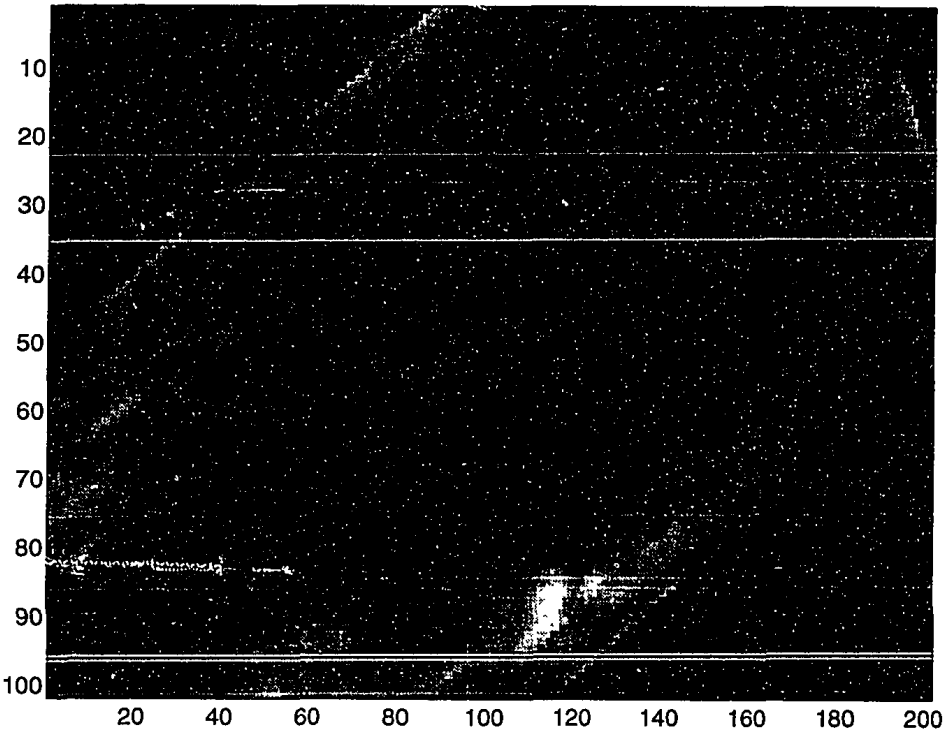

Figure 2.1: Cropping effect.

Several of the key steps are illustrated in Fig. 2.2. Figure 2.2(a) represents the original ROI. Figure 2.2(b) represents the oversized 150% window W_1 containing the

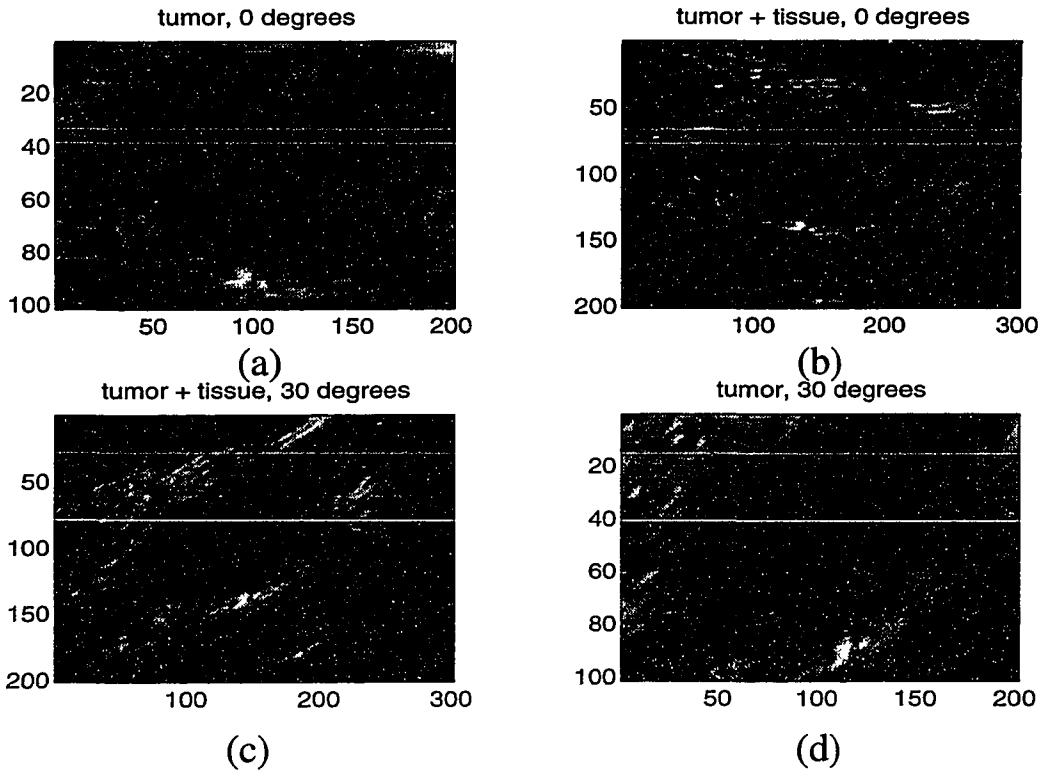

Figure 2.2: Illustration of steps. (a) Tumor, (b) tumor plus surrounding tissue, (c) tumor plus surrounding tissue after rotation, (d) tumor only after rotation.

ROI and surrounding tissue (step 1). Figure 2.2(c) is the oversized 150% window W_1 after rotation (step 2). Figure 2.2(d) is the window W_1 after reduction back to the original ROI dimensions (step 2b).

2.6.2 Calibrated phantom results

Ultrasound B-scan images of a fine pore sponge before and after a 2.0 degree rotation were acquired using a 5.0 MHz ATL imaging transducer. Rotational motion was simulated by rotating the transducer using a computerized positioning system. Both the imaging and positioning systems used to acquire these images are described in detail in Chapter 3.

Figure 2.3 illustrates several of the key steps in applying the rotational correlation search algorithm to track the rotation of the sponge phantom. Figure 2.3(a) represents the original ROI. Figure 2.3(b) represents the oversized 150% window W_1 containing the ROI and surrounding tissue (step 1). Figure 2.3(c) is the oversized 150% window W_1 after rotation (step 2). Figure 2.3(d) is the window W_1 after reduction back to the original ROI dimensions (step 2b).

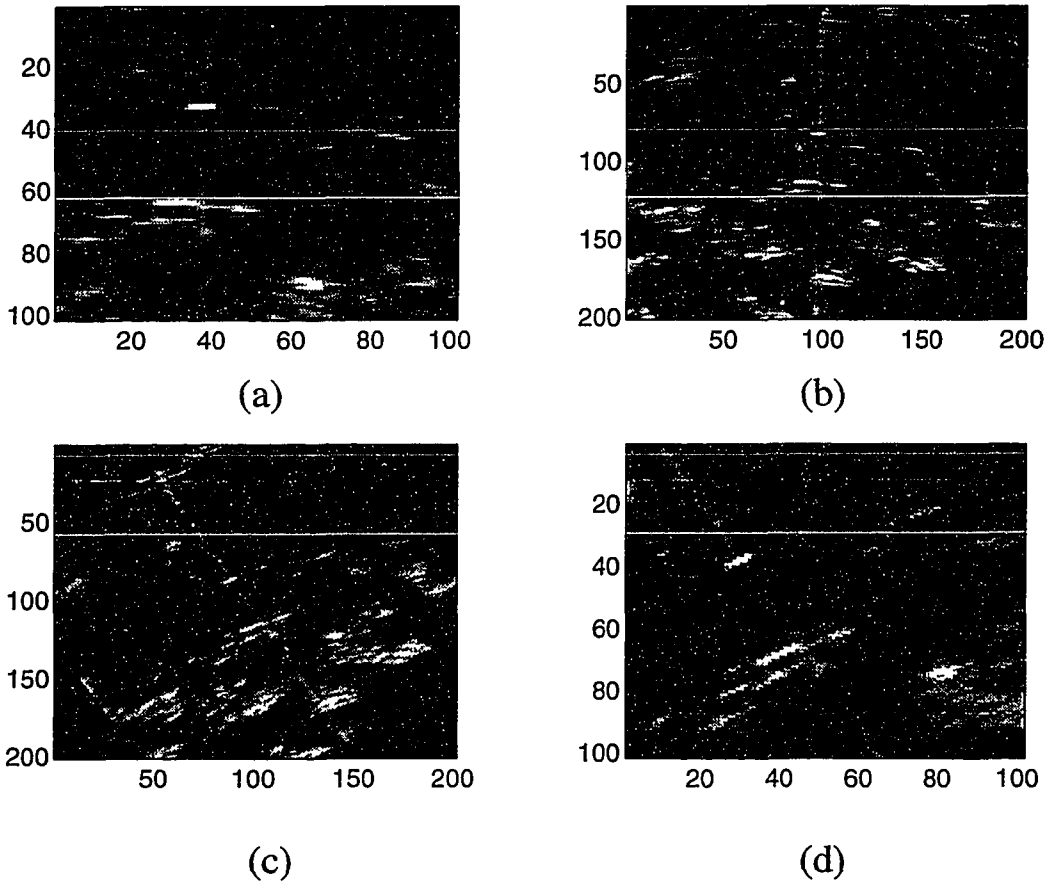

Figure 2.3: Sponge phantom rotational motion example. (a) The original ROI, (b) ROI plus surroundings, (c) ROI plus surroundings after rotation, (d) ROI only after rotation.

Figure 2.4 depicts the correlation function $\rho(\phi)$ obtained from the rotational correlation search of the sponge phantom. The correlation function has a peak at ϕ = -2.0°, although the correlation function has a broad central lobe.

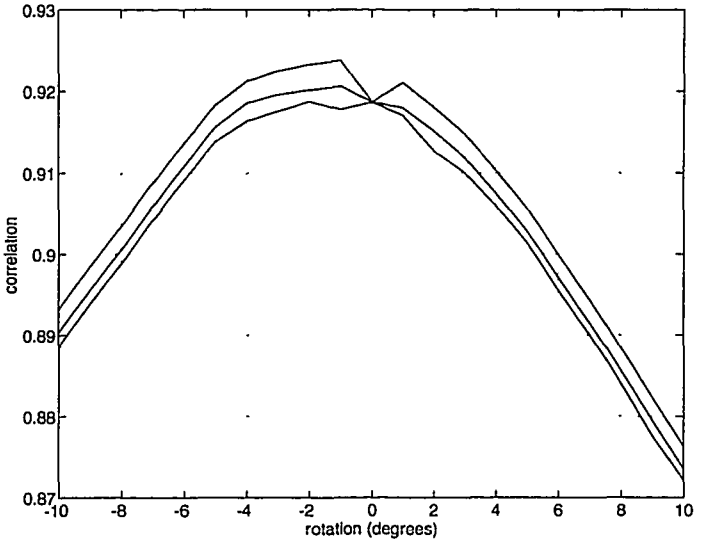

Figure 2.4: Correlation function for nearest neighbor, bilinear and bicubic interpolations.

Three different interpolation algorithms were used in the rotational correlation search: 1) nearest neighbor interpolation, 2) bilinear interpolation and 3) bicubic interpolation. Nearest neighbor interpolation selects the intensity of the nearest pixel (in a 9 pixel neighborhood) for image pixels that do not fall on the original grid points after rotation. Bilinear interpolation performs a linear filtering operation using an 11×11 filter kernel, which provides a uniformly weighted average of the pixels in the kernel region, for image pixels that do not fall on the original grid points after rotation. Bicubic interpolation performs a linear filtering operation which provides a weighted average using the same sized kernel function, with closer pixels weighted more heavily according to a cubic function.

The correlation function was computed for three different interpolation algorithms. The results, shown in Fig. 2.4, indicate that there was not a significant difference in the rotational correlation functions using the three interpolation algorithms. Bilinear interpolation provided marginally higher correlation coefficients. For ultrasound images, information contained in the image texture depends in part on the speckle spot size determined by the focusing characteristics and bandwidth of the transducer. For the standard B-scans used, a typical speckle spot size could be between 8-12 pixels. Since all

pixels within a single speckle spot would be strongly (and roughly equally) correlated, this might explain why a linear uniformly weighted average performs reasonably well.

2.6.3 Breast tumor results

Ultrasound images of a breast tumor before and after an unknown rotation were acquired using a 7.5 MHz linear array transducer (Acoustic Imaging, Phoenix, Arizona). These data were obtained from the department of radiology at the University of Michigan hospital. Clinical protocols used in obtaining these data will be described in detail in Chapter 5.

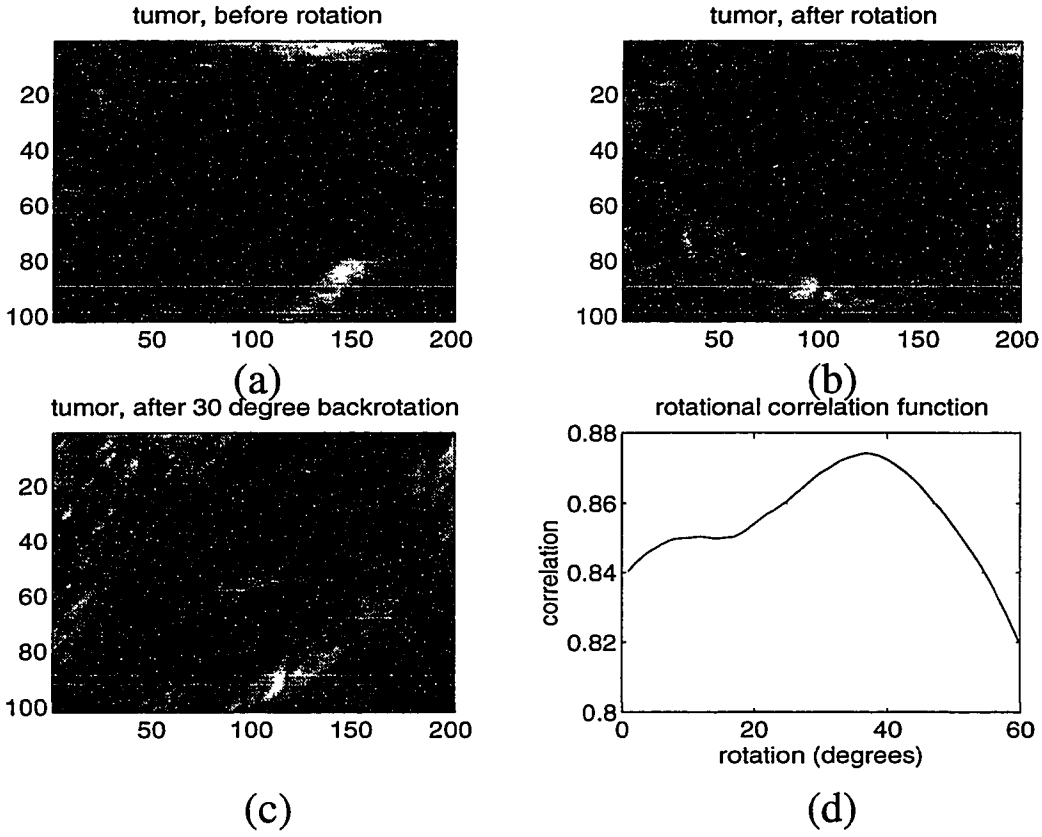

Figure 2.5: Tumor rotational motion example. (a) Breast tumor before rotation, (b) tumor after rotation, (c) tumor in part b) back-rotated by 30 degrees, (d) correlation function for tumor rotation.

Figures 2.5(a)-(b) show an ROI containing a tumor before and after an unknown rotation. Figure 2.5(c) is the ROI in (b) backrotated by 30°. Figure 2.5 is the rotational correlation function. The best correlated match occurs at an angle of approximately 30°. Although the actual angle of tumor rotation is unknown, visual comparison of the back-rotated and original ROIs in (a) and (c) indicate the estimated angle is reasonable.

CHAPTER 3

ACCURACY OF DISPLACEMENT AND VELOCITY IMAGING

In this chapter we investigate the accuracy of ultrasound speckle tracking in various tissues. Results from two-dimensional tissue speckle tracking in liver, muscle, fat and sponge samples are presented, while keeping other speckle tracking parameters constant. Speckle tracking performance was characterized both in terms of the magnitude of tracking errors and the percentage of correctly tracked displacement vectors. Speckle tracking in muscle tissue, which contains myofibrils and significant tissue microstructure, produced the highest percentage of correctly tracked vectors and smallest tracking errors relative to other tissues.

3.1 Background

The goal of this work is to investigate the accuracy of ultrasound speckle tracking in various tissues. Two-dimensional speckle tracking algorithms attempt to estimate local tissue motion by matching speckle patterns in serially acquired ultrasonic images. Speckle tracking has been used in ultrasonic blood velocity measurements to detect signs of venous thrombosis and other vascular diseases [38], in non-invasive ultrasonic elasticity imaging of hard tumors to monitor early development of breast cancer [3], in intravascular imaging of arterial walls to measure plaque buildup and the subsequent development of atherosclerosis [1], and in phase aberration correction techniques [45]. The reliability of ultrasonic blood velocity, tissue elasticity and phase aberration correction measurements depends on the accurate performance of speckle tracking.

Elasticity imaging, for example, often requires two-dimensional speckle tracking of small areas of tissue to estimate internal tissue displacement. Tissue displacements are then used to reconstruct tissue strain fields. Errors in speckle tracking resulting in errors in displacement estimates directly influence the accuracy of strain estimates and

ultimately reconstructed elasticity fields. In a similar fashion, measurements of phase aberrations and blood velocity depend on reliable speckle tracking. Thus, it is critical to understand to what degree speckle tracking measurements are reliable and how different factors may affect the reliability of those results. Of particular interest is the effect of various tissues on speckle tracking. In this study, we investigate the performance of speckle tracking in liver, muscle and fat tissues, while keeping other speckle tracking parameters such as ultrasound frequency and region of interest (ROI) dimensions constant. The effect of other important imaging parameters on speckle tracking accuracy have been reviewed in [42].

3.2 Calibrated Tracking Measurements

Four types of samples, three tissues and one sponge, were used in speckle tracking experiments. Tissue samples consisted of porcine muscle, liver and fat obtained from the Meat Sciences Laboratory, Department of Animal Sciences at the University of Illinois. Tissue samples were approximately 150 mm in length and 100 mm by 100 mm in width and height and were vacuum sealed. Tissue samples were packed in ice and transported to the Bioacoustics Research Laboratory for experiments within 24 hr of death. The sponge sample consisted of a standard commercially available fine pore urethane sponge with dimensions of 150 mm $\times$ 100 mm $\times$ 100 mm. Similar sponge targets have been used in previous studies [46] and have been shown to produce reasonable speckle images. A histogram of pixel intensities was also used to verify speckle scattering. Samples were placed below an ATL transducer and secured on top of sound absorbing slabs near the bottom of a water tank. Ultrasound B-scan images of samples were acquired using a 5.0 MHz, 742A ATL servo-controlled rotary system coupled to an ATL MK-500 imaging system. The ATL transducer had a 9.5 mm diameter crystal and used a mechanical sector scan with a 4.0 cm focal distance, and with a focal region extending from 2.0 cm to 6.0 cm. Samples were positioned in the approximate center of the transducer's focal region and were imaged in a manner to cover the entire field of view of ultrasound B-

scans. All measurements were performed at room temperature ($22°C$) and the positions of all tissue samples remained fixed throughout the experiment.

To simulate axial and lateral tissue motions, the transducer was translated using a high precision Daedal motorized positioning system (precision of 5 microns for axial and lateral motions [47]). The positioning system is computer controlled and has five degrees of freedom, three translational and two rotational. Sequentially acquired frames of tissue motion were digitized using a Targa-16 frame grabbing system with a spatial sampling (pixel size) of approximately 0.25 mm per pixel in both the axial and lateral directions. Digitized gray scale images were ported to a Sun Sparc 20 workstation for speckle tracking and analysis. A sequence of ten images was acquired for each tissue. The following speckle tracking parameters were held constant throughout the experiment: ultrasound frequency (5 MHz), magnitude and direction of motion (axial and lateral translations in 1.0 mm increments), ROI size (3.0 mm $\times$ 8.0 mm).

3.3 Performance Criteria

To characterize the performance of speckle tracking in each of the tissues, displacement vectors were computed for ROIs inside the focal region, and speckle tracking performance was calculated in terms of the percentage of correctly tracked displacement vectors. The size of the search region used in both the axial and lateral directions was 1.3 times the magnitude of the actual displacement. Similarly sized search regions were used in previous studies and shown to provide reasonable speckle tracking [43]. Following the convention of previous groups [34], displacement vectors tracked within 30% of the actual displacement in the axial and lateral directions were considered correct. Thirty-two displacement vectors were calculated for each translation. The dimensions of ROIs were 3.0 mm $\times$ 8.0 mm or approximately four resolution lengths in each dimension [41]. The axial and lateral resolutions of the ATL imaging system was estimated to be approximately 0.75 mm and 2.0 mm, respectively, based on the transducer frequency, diameter, focal length and pulse width.

An incremental tracking algorithm was used to measure large displacements. Using this algorithm, large displacements were obtained by summing smaller interframe displacements. For example, a 3.0 mm displacement between frames 1 and 4 in an image sequence is estimated by summing the differential displacements between frames 1-2, 2-3 and 3-4.

The magnitude of tracking errors was computed for all ROIs tracked in all tissues. Tracking error was defined as the geometric distance between actual and tracked displacements and is mathematically defined as

$$e = \sqrt{((x_t - x_o)^2 + (y_t - y_o)^2)} \tag{3.1}$$

where (x_o, y_o) and (x_t, y_t) denote the actual and tracked coordinates of displacement, respectively.

One of the problems encountered in assessing the performance of speckle tracking was whether to characterize tracking performance in terms of tracking error (geometric distance between actual and tracked displacements) or in terms of the percentage of correctly tracked vectors. Tracking errors provide more exact information about the magnitude of errors, yet are less useful in conveying the performance of tracking a large number of vectors. In addition, tracking errors for a single ROI can be misleading if the ROI happens to track very correctly or incorrectly. Performance measured in terms of the number of correctly tracked vectors has been used by previous groups [34]. The drawback of this method is that no specific information is provided regarding the magnitude of errors for vectors that are correctly or incorrectly tracked. ROIs from different tissues may result in the same percentage of correctly tracked vectors for a given displacement. Yet the average magnitude of tracking errors may differ significantly. In fact, tracking errors between two different tissues may differ by as much as 30% for correctly tracked vectors. This difference could be even higher for incorrectly tracked vectors. In addition, the threshold of 30% (vectors tracked within 30% of actual displacement assumed correct)

is arbitrary and the fact that search dimensions were selected to be 1.3 times the actual displacement may positively bias results.

We have chosen to assess the performance of speckle tracking in terms of both tracking error and percentage of correctly tracked vectors. The latter is useful in conveying the performance of speckle tracking for a large number of vectors, while the former provides more detailed information regarding the magnitude of tracking errors. All tracking errors were computed by averaging the errors from at least ten independent, non-overlapping ROIs selected from within the focal region in all tissues. This provided additional insight into the true speckle tracking performance in each tissue. For example, in the axial dimension, while almost all vectors were correctly tracked in all tissues as defined by the 30% threshold, it is clear that the magnitude of tracking errors was largest in fat tissue. This could lead to larger errors in ultrasound displacement and strain imaging in fat compared to those for other tissues. Information about the magnitude of speckle tracking errors in each tissue would not be directly available from plots of the percentage of correctly tracked vectors. Fat samples also produced the widest axial and lateral autocovariance curves compared to those for muscle, liver and sponge, which suggests a larger speckle cell size.

3.4 Speckle Statistics

Tissue autocovariance curves were generated by selecting an axial or lateral line of data passing through the center of digitized images of each tissue type. An autocovariance sequence was computed for each line of data using the sample autocovariance estimator

$$C(k) = \sum_{i=0}^{N-|k|-1} (x(i) - \bar{x})(x(i+k) - \bar{x}) \tag{3.2}$$

and normalized to amplitude values between 1.0 and -1.0. In Equation (3.2) k represents the shift or spatial separation between two points on an ultrasound image and $\bar{x}$ represents

the average pixel value in the image x. The autocovariance curves provide information about how correlated or related two different points, separated by a distance k, in the ultrasound image are. The autocovariance or correlation between two points in an image typically decreases as the distance k between the points increases. An image consisting of random white noise could be expected to have a very narrow autocovariance curve with a peak at $C(0)$ with $C(k) = 0$ for k $\neq$ 0, which indicates that all of the pixels separated by a distance $k > 0$ are uncorrelated. An image of constant intensity would have a flat (or very broad) autocovariance curve $C(k) = 1$, which indicates that all of the information in the image is highly correlated or redundant. The term auto comes from the fact that we are computing the correlation between pixels within the same signal or image.

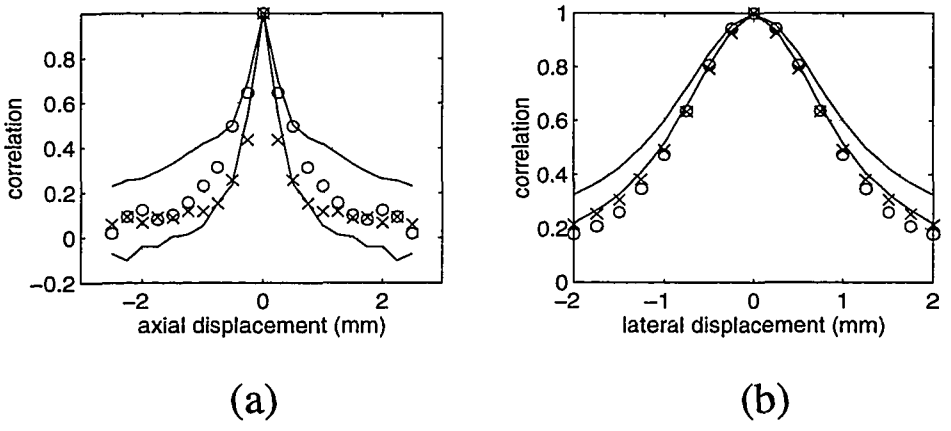

Figure 3.1: Tissue autocovariance curves. Liver (x), muscle (o), sponge and fat (-).

The axial and lateral experimental autocovariance curves for liver, muscle fat and control sponge are shown in Fig. 3.1. Measurements were averaged over five axial and lateral lines of data. Speckle pattern decorrelation for axial and lateral translations of the control sponge are shown in Fig. 3.2. Data points are the average of five independent, non-overlapping ROIs.

Errors in tissue speckle tracking have been categorized into two main types [43]. Jitter errors occur when the position of the actual correlation peak has been shifted inside of the main lobe due to noise. False peak errors occur when the position

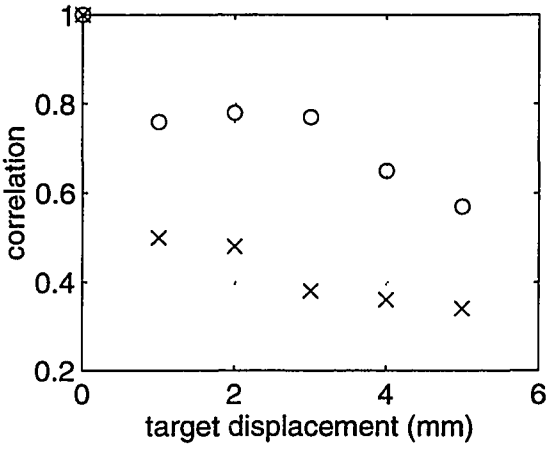

Figure 3.2: Speckle decorrelation curve. Axial translation (o), lateral translation (x).

of the actual correlation peak has been shifted to one of the sidelobes. In tissue speckle tracking a correlation function can be generated and plotted from the correlation coefficients, at each position inside the search area. The location of the correlation peak should correspond to the area of tissue providing the best match with the ROI and this location can be used to compute the displacement of the ROI. Correlation interpolation methods have been suggested to more precisely estimate the exact location of the true correlation peak, which may fall between data points [48]. Tissue tracking correlation functions will often have many of the same characteristics as the tissue autocorrelation curve. An autocorrelation curve with a broad main lobe will make it more difficult to locate the exact position of the peak correlation and will thus contribute to jitter errors [41, 42, 43]. High amplitude sidelobes in the tissue autocorrelation curve will increase errors due to false peaks. Errors due to the classic peak hopping phenomenon can be reduced by using the moment, or center of mass, of the correlation function rather than simply the peak amplitude of the correlation function. The second-order statistics of speckle generated by different tissues should provide an indication of speckle tracking performance [41, 42, 43].

Covariance curves for all tissues were very similar and were within the 95% confidence intervals of one another. Based on the covariance curves, we would not expect speckle tracking performance to be significantly different in the various tissues in tracking over

short distances. This was observed to be the case in both the axial and lateral directions for displacements up to 2.0 mm, where close to 100% and 80%, respectively, of all vectors were correctly tracked in all tissues. At larger displacements, particularly in the lateral direction, the difference in speckle tracking performance increases. For larger magnitude displacements (2.0 mm - 4.0 mm) the covariance curves may be less reliable predictors of tracking performance since the variance of autocovariance estimates was observed to increase significantly for larger lags (displacements). For all tissues, axial covariance curves were between two to four times narrower than for the corresponding lateral covariance curves.

3.5 Results

The performance of speckle tracking depends on a number of ultrasonic imaging parameters including magnitude and direction of tissue motion, ROI dimensions, ultrasonic frequency and tissue type. The two-dimensional performance of tissue speckle tracking was quantified in terms of the percentage of correctly tracked displacement vectors in three different tissue types, while keeping other parameters constant.

3.6 Effect of Tissue Type

Quantitative comparison of speckle tracking performance in each of the tissues in terms of percentage of correctly tracked vectors is shown in Fig. 3.3. Axial speckle tracking accuracy was approximately the same in all tissues. Almost all ROIs were correctly tracked in all of the tissues for displacements up to 3.0 mm. In the lateral direction, for displacements up to 2.0 mm, speckle tracking performance was comparable in all tissues. For larger displacements (2.0 mm - 4.0 mm), speckle tracking accuracy in liver was approximately 10% lower than in the control sponge, and approximately 20% lower than in muscle. Speckle tracking performance can also be plotted as a function of the imaging system axial and lateral resolutions. Axial speckle tracking results are

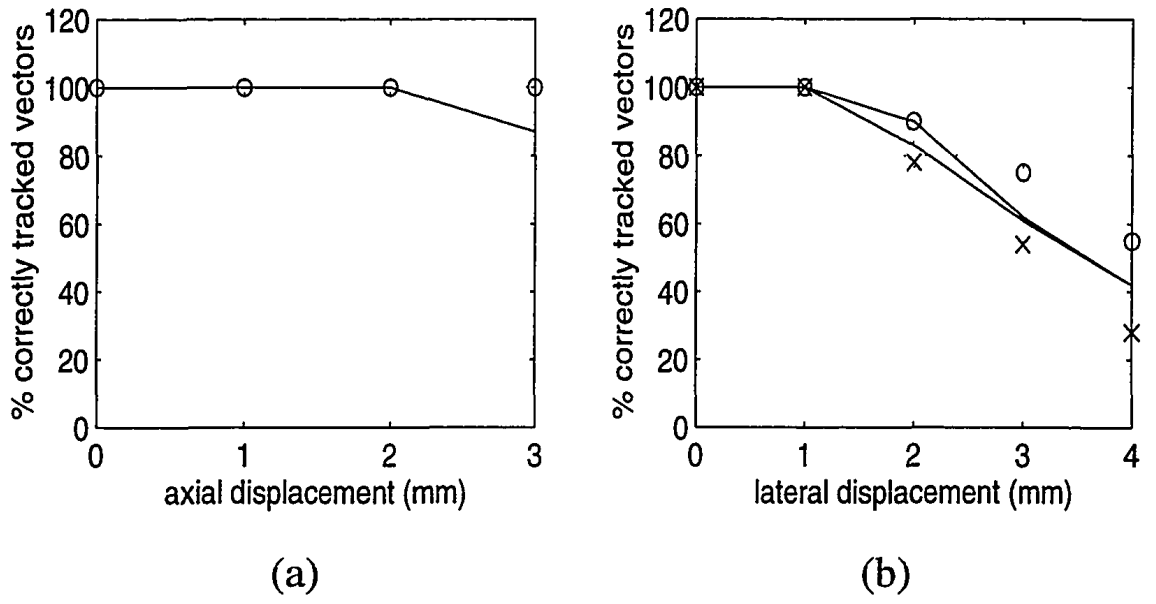

Figure 3.3: Percentage of correctly tracked vectors. Liver (x), muscle (o), sponge and fat (-).

shown over a slightly smaller displacement range so that the maximum translation in both directions is equivalent to approximately four resolution lengths.

All measurements in tissues were compared with measurements of a control sponge. Similar sponge targets have been used by previous groups and have been shown to generate reasonable ultrasound speckle images [46].

Tracking errors appeared to be consistently lower in muscle tissue relative to the control sponge, and consistently higher in fat for both axial and lateral translations. The improved tracking in muscle relative to liver and fat may be due to the presence of a large number of myofibrils, blood capillaries and other muscle tissue microstructures, and the absence of such microstructure in liver and fat.

3.7 Tissue Morphology

3.7.1 Liver

Liver tissue is predominantly composed of hepatic and Kupfer cells. These cells are polyhedral in shape and have dimensions ranging from approximately 200 to 400 microns.

Despite the presence of portal and hepatic veins, liver posseses a relatively homogeneous tissue morphology [49, 50, 51, 52].

3.7.2 Muscle

Muscle tissue posseses a relatively heterogeneous internal tissue morphology, which is attributable to the presence of many well-defined and often acoustically resolvable image structures contained in muscle that appear in the form of long strands and streaks [42]. Muscle tissue is composed of thousands of cylindrical muscle fibers with diameters ranging from 10 to 100 microns and with lengths as long as 30 cm [53, 54, 55]. Inside the muscle fibers are cylindrical elements (myofibrils) 1 to 2 microns in diameter. Myofibrils occupy approximately 80% of fiber volume. Myofibrils are contained in an inner membrane called the sarcolemma, which, in turn, is contained in an outer membrane called the basil lamina. Muscle fibers are grouped in clusters or bundles. Individual muscle fibers are held together by a connective tissue sheet known as the endomysium, which may also contain nerve axons and blood capillaries. Bundles of muscle fibers are contained in a connective tissue known as the perimysium, which is contained inside an outer tissue layer called the epimysium. In scattering theory, muscle is often approximated as a collection of cylindrical fiber elements [56]. The internal morphology of muscle is composed of many layers and tissue structures. A combination of one or more of these structures may provide distinct and acoustically resolvable image structures.

3.7.3 Fat

Animal cells store fatty acids in the form of fat. Most fat in animals is stored in adipose tissue where it can be used to ensure a continuous supply of fuel for animal metabolism. Fat molecules are composed of three fatty acid molecules called triacylglycerols. These molecules have no charge and are largely insoluble in water [55]. As such, fat molecules coalesce into droplets in the cystol (area between cell structures) in most animal cells. Large fat droplets account for most of the volume in adipocytes or fat cells. Adipocytes are believed to develop from fibroblastlike cells. While the exact conversion process is

more detailed, adipocytes are essentially an accumulation of fat droplets that coalesce and are surrounded only by a thin rim of cytoplasm [55]. Fat tissues are therefore largely homogeneous in composition, lacking the presence of distinct or resolvable image structures.

3.7.4 Sponge

A fine pore sponge was used as a control tissue. The sponge contained a large number of small pores with diameters ranging from approximately 1.0 mm to 1.0 cm. The internal morphology of the sponge was predominantly homogeneous containing few distinct or acoustically resolvable image structures.

3.8 Effect of Target Motion

3.8.1 Magnitude of motion

Tissue speckle tracking errors for axial and lateral translations are shown in Fig. 3.4. Tracking errors shown are the average of tracking errors from speckle tracking ten separate, non-overlapping ROIs. Tracking errors appeared to be lower in muscle tissue relative to that of the control sponge, and higher in fat for both axial and lateral translations.

3.8.2 Direction of motion

Tracking performance was observed to be substantially better in the axial direction for all tissues in terms of both magnitude of tracking errors and percentage of correctly tracked displacement vectors. Tracking performance also deteriorated for larger translations, results that are in agreement with previous studies [42, 46].

3.9 Limitations and Problems

Because ultrasonic echoes result from internal tissue variations of acoustic parameters, differences in the variation of propagation speed inside each tissue type may result in

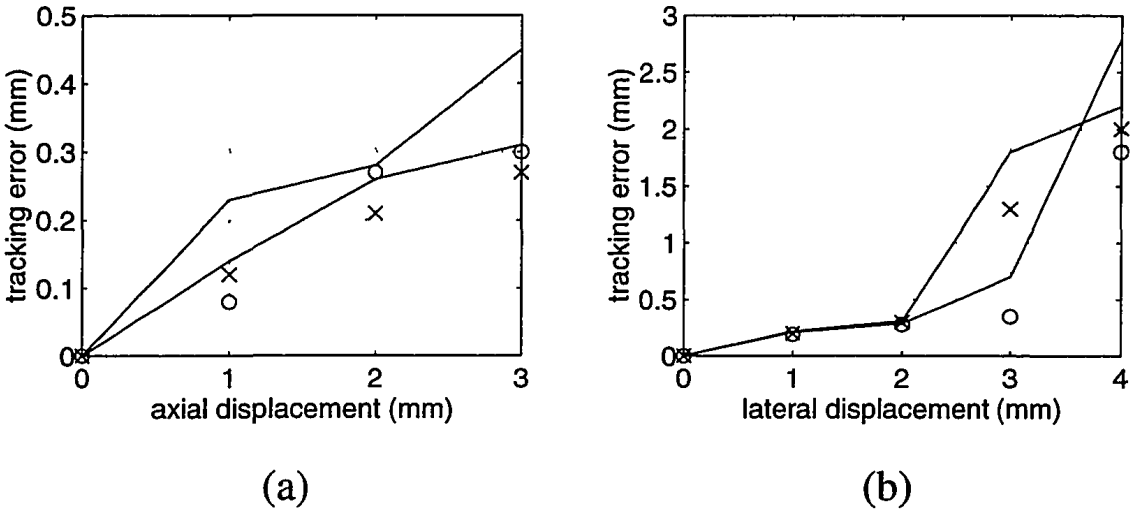

Figure 3.4: Tissue speckle tracking errors. Liver (x), muscle (o), sponge and fat (-).

different signal to noise ratios in the echoes received from each tissue. In addition, attenuation effects could result in a downshift in the center frequency of reflected echoes, thus changing the effective ultrasonic frequency of interrogation and affecting tracking accuracy. The propagation speed for all four sample types is within 5% of each other [30]. Also, the differences in attenuation between liver and muscle are typically less than 10% [57] and downshifts in frequency due to attenuation are typically on the order of only a few hundred kilohertz for a center frequency of 5.0 MHz. Thus, the contribution from these effects should remain relatively small.

Speckle tracking performance will also be clearly dependent on the transducer axial and lateral resolutions and focusing characteristics. Since B-mode images were acquired using a mechanical scan transducer with a fixed focal distance, all ROIs were selected within 1.0 cm of the focal plane, within the transducer focal region (2-6 cm).

A major difficulty in estimating tissue covariance curves was the non-constancy of received B-mode signal levels with increasing range. This problem was also observed in [41]. To reduce this effect, autocovariances were computed only over axial regions where the received signals were relatively constant. However, the short sample intervals had the effect of increasing the variance of autocovariance curves. Results from averaging data

from five different axial signals separated by at least two lateral correlation lengths [58] and taken from different images helped to reduce these variances.

Axial and lateral tissue autocovariance curves may be strongly affected by tissue anisotropies. Since muscle tissue contains a large number of myofibrils and other tissue microstructures which may result in periodic or highly correlated object structure [41], we could expect to see larger differences between muscle axial and lateral covariance curves than for those in liver, fat and control sponge which more closely resemble isotropic media. However, we are less likely to see significant differences in the axial and lateral covariance curves if muscle fibers are randomly oriented, thus providing an equally random medium in both directions. We would expect to see significant differences in axial and lateral covariance curves if the majority of fibers were oriented in the same direction. For the muscle samples used in the study, muscle fiber orientation was observed to be largely random, with fibers neither parallel nor perpendicular to the ultrasound beam. We therefore did not observe more significant differences between muscle axial and lateral covariance curves relative to liver and fat tissue.

It should be understood that using incremental tracking, errors will accumulate with increasing displacement, independent of decorrelation effects. For example, for cases where there is very little or no decorrelation, net tracking will be more accurate. There is therefore a tradeoff between incremental tracking step size and decorrelation effects.

Our results suggest that speckle tracking for ultrasound elasticity imaging in muscle and liver tissues should provide reasonably accurate results for small displacements (1.0 mm - 2.0 mm). For larger displacements, displacement estimates based on direct speckle tracking may be less accurate, particularly in the lateral direction and in fat tissue. Use of an incremental tracking strategy should help to reduce tracking errors due to speckle decorrelation.

CHAPTER 4

ULTRASOUND ELASTICITY IMAGING

This chapter discusses some of the basic terms, equations and assumptions used in elasticity imaging. Two of the important topics discussed are the Poisson ratio and the constrained Young's modulus.

4.1 Tissue Mechanics

Elasticity is the ability of a strained body to recover both its size and shape after deformation. A material that bounces back to its original size and shape after loading is said to behave elastically. A common abuse of notation occurs when we refer to the elasticity of a material when we really intend to discuss its stiffness or elastic modulus.

The longitudinal elastic modulus on a sample of material is defined as the normal stress (force/unit area) on the sample divided by the resulting longitudinal strain (change in length/original length) on the sample

$$E = \frac{\sigma}{\epsilon} \tag{4.1}$$

where E represents the longitudinal elastic modulus, σ is the applied stress and ϵ is the resulting longitudinal strain defined in Equation (4.2).

$$\epsilon = \frac{\Delta L}{L} \tag{4.2}$$

Here ΔL represents the change in length (height) of the sample after a load is applied and L is the initial height of the sample. The stress-strain relation in Equation (4.1) is also well-known to engineers as Hooke's Law. In these studies, our goal was to estimate the global elastic modulus of tissue samples, essentially treating each sample as a single

one-dimensional spring with a uniform spring constant K. For small deformations, the tissue sample obeys Hooke's Law

$$F = Kx \tag{4.3}$$

The elastic modulus or Young's modulus E in Equation (4.1) is analogous to the spring constant K in Equation (4.3). Young's modulus (YM) provides a measure of the stiffness of a material and is valid for only small strains (typically $< 3\%$) [59, 60]. By measuring the strain for several different applied stresses, the stress-strain behavior of the samples can be characterized. Young's modulus acts as a constant of proportionality between the stress and strain on a material, and it can be estimated from the slope of the curve in the linear region of the stress-strain curve.

The Poisson ratio, ν, represents the degree to which a material expands laterally, as it is strained (compressed) axially.

$$\nu = \left| \frac{lateral \;\; strain}{axial \;\; strain} \right| \tag{4.4}$$

The Poisson ratio is limited to values between $0.0 < \nu < 0.5$ [61]. Materials with $\nu = 0$ are termed completely compressible, while materials with $\nu = 0.5$ are termed incompressible. Compressibility roughly represents the degree to which the material obeys a conservation of volume. When completely compressible materials are compressed axially, they do not expand laterally. When incompressible materials are compressed axially, their volume must remain constant and they expand laterally.

Most soft tissues are considered as roughly incompressible materials and are assumed to have a Poisson ratio in the range of $0.45 < \nu < 0.49$ [59]. Intuitively, this means that if the tissue is compressed by 1 unit axially (in the z-direction), it must expand by roughly 0.5 units laterally in both the x and y directions.

4.2 Constrained Young's Modulus

In the preceding discussion and in the sections that follow, the theory is described for one-dimensional measurements. Ideally, for one-dimensional measurements, all samples measured should be bar samples. However, in practice, samples will have a finite height-to-diameter aspect ratio. The exact effect of sample dimensions on test measurements will be discussed in Chapter 6.

In elasticity measurements it is important that samples remain unconfined or unconstrained laterally as they are compressed axially. If samples are constrained laterally then the constrained YM (Y_b) will be larger than the unconstrained YM (Y_o). The constrained YM Y_b, is related to the unconstrained YM Y_o according to the equation

$$\frac{Y_o}{Y_b} = 1 - \frac{2\nu^2}{1-\nu} = C \tag{4.5}$$

where ν represents the Poisson ratio of the material. Therefore, C represents a correction factor between the constrained and unconstrained cases.

4.3 One-Dimensional Displacement Imaging

By applying precise uniaxial compressions to a tissue sample, and by measuring the resulting stress and strain on the sample, discrete points of the tissue stress-strain curve can be obtained. Correlation analysis of digitized ultrasound A-lines acquired after each incremental compression allows the incremental deformation and strain on the sample to be precisely calculated. The equivalent applied stress on the sample is experimentally determined from scale readings.

A one-dimensional tissue displacement profile can be computed by placing multiple, possibly overlapping windows at various positions in a pre-compression ultrasound A-line and tracking the displacement of each window. Larger window sizes provide improved accuracy in displacement tracking, while smaller window sizes provide improved resolution in the tissue displacement profile.

By incrementally compressing a tissue sample, the stress-strain response of the sample can be investigated for very large strains using incremental tracking of tissue displacement.

4.4 One-Dimensional Strain Imaging

Cross-correlation of data windowed from each ultrasound A-line can be used to calculate the displacement of the bottom surface of a tissue sample after the tissue is compressed. As a simple example, the correlation technique can be used to track the position of the top and bottom (endpoints) of the sample before and after compression. By tracking the displacement of the endpoints, the thickness and thus **global** strain on the sample can be precisely calculated (approximately 4% error for displacements up to 2.0 mm as cited in Section 2.5).

A one-dimensional strain profile of **local** tissue strains can be computed again by placing multiple, possibly overlapping windows at various positions in a pre-compression ultrasound A-line and comparing the **relative** displacement of adjacent windows. This is achieved by subtracting the displacement of adjacent windows. Conceptually, we can think of placing a set of N equally spaced markers along the pre-compression A-line. The N markers divide the A-line signal into $N-1$ equally sized segments where each segment represents a small one-dimensional spring or tissue element. By tracking the relative displacement of the markers, we can compute the strain on each tissue element using:

$$\epsilon(i) = \frac{\Delta L(i)}{L} \tag{4.6}$$

where $\epsilon(i)$ represents the strain of the ith tissue element, $\Delta L(i)$ is the difference in displacement between the i and $i+1$ markers and L represents the length of a tissue element. The tissue strain distribution is essentially the derivative of the tissue displacement distribution.

4.5 Uniformity of Stress Distribution

If a small sample of tissue is deformed by a compressing punch, the resulting stress distribution in the tissue sample will be uniform and constant **provided** that the surface area of the compressing punch is greater than or equal to the surface area of the sample. It is generally desirable to use a compressor punch that is larger than the sample to reduce the possibility of stress non-uniformities at the sample edges. In this study, all experiments were conducted with punch surface dimensions larger than sample surface dimensions. One-dimensional tissue stress profiles will all be considered to be uniform and of a constant stress under the assumption of uniform stress distribution. Tissue stresses will be experimentally measured from scale readings and Daedal computer-controlled compressions.

4.6 One-Dimensional Elasticity Imaging

By combining information from tissue stress and strain distributions a one-dimensional profile of tissue elasticity can be computed. A longitudinal profile of the Young's moduli of small tissue elements is obtained by simply dividing the stress on a particular tissue element by the corresponding strain on the same element according to Equation (4.7).

$$E(i) = \frac{\sigma}{\epsilon(i)} \tag{4.7}$$

where $E(i)$ represents the longitudinal elastic modulus of the ith tissue element, σ is the uniform applied stress and $\epsilon(i)$ is the resulting longitudinal strain on the ith tissue element.

CHAPTER 5

DISPLACEMENT IMAGING OF BREAST CANCERS

In this chapter, we investigate the feasibility of using ultrasound to measure tissue motion for cancer detection. Tissue displacement images from eight patients with sonographically apparent breast masses are used to illustrate the technique. The local displacement response of tissues surrounding malignant and benign breast masses is compared, testing the hypothesis that altered mechanical properties may result in motion signatures for many soft tissue tumors relative to their host tissue. In addition, the potential or anticipated influence of various biological and physical factors on tissue motion response is discussed.

5.1 BACKGROUND

Recent studies indicate that breast cancer affects one out of every eight women in the United States [62]. Early detection can greatly improve a woman's chances for survival [63]. It is estimated that approximately 20 percent of breast cancers are missed in conventional mammographic screening [64]. Several risk factors for breast cancer have been identified [65]. These include family history, nutrition and exposure to radiation. Yet in almost 75 percent of women with breast cancer, none of these factors is present [65]. While not present in all mammograms, the presence of a stellate mass in the breast is one of the most distinct mammographic characteristics of a breast malignancy[64,66-71].

5.1.1 Physiology of malignant breast masses

It is believed that cancer cells in the breast stimulate the growth of fibrous tissues. This pattern of growth, termed desmoplastic reaction, is what gives malignant breast masses a dense or hard consistency. Carcinoma cells grow in the path of least resistance. When the surrounding tissues are firm and have a mostly glandular constituency, as found in younger women, the tumor cells tend to grow in clefts between fibrous regions.

When the surrounding tissues are soft and have a more fatty consistency, tumor cells grow in all directions. Many primary malignancies exhibit a stellate (star-shaped) pattern or spiculated appearance [66, 67, 68]. The spiculated appearance of many malignant masses in the breast, with tentacles radiating outward from the tumor into surrounding tissues, is well-documented in the literature [66,72-79].

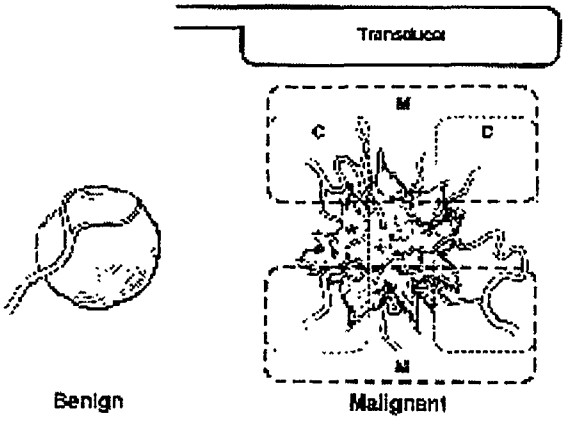

Figure 5.1: Textbook drawings of malignant and benign tumors.

Drawings of idealized infiltrative and benign primary breast lesions are shown in Fig. 5.1 (adapted from [69]). The infiltrative malignant mass is characterized by a stellate configuration with spicules and is reasonably typical of invasive ductal carcinoma. In other cases, the invasion may have longer stellate radial arms due to desmoplastic reaction between the surrounding tissue and the tumor and may include invasion along ducts and other connective tissue surfaces.

The degree of desmoplastic reaction or deformation of surrounding tissues due to bonding between the tumor and connective tissues will alter the tumor and connective tissue responses to palpation. Ultrasound provides a method for real-time imaging of local tissue motion, which may be helpful in diagnosing breast cancer [70]. Ultrasonic

measurement of local tissue motion provides a means of quantifying tumor and connective tissue responses to palpation. This information could be potentially used in the early detection and classification of many developing breast cancers.

Desmoplastic reaction may also alter the mechanical and thus tissue elastic properties of invaded areas. Ultrasonic elasticity imaging, which involves non-invasive ultrasonic measurement of tissue elastic properties, has also been demonstrated as a viable means of imaging small, totally non-palpable objects in simulated gel phantoms of the breast [3, 4, 31, 32].

5.2 METHODS

High frequency ultrasound images of malignant and benign breast masses were acquired from eight patients seen in the Department of Radiology at the University of Michigan Hospital. Information regarding patient age, menopausal status, type and size of mass and biopsy type, and results are shown in Table 5.1.

Patients were scanned using a 7.5 MHz linear array transducer (Acoustic Imaging, Phoenix, Arizona). The transducer was used to perform palpation with the patient supine and the breast stationary. In each case the patient's arm was placed above the head on the side scanned. The term palpation is used to denote a translational motion of the imaging transducer over the breast accompanied by a hand-rocking motion by the physician. The transducer was translated opposite to the direction of palpation, imparting a small shearing force on the parenchymal tissue directly above the mass. We were particularly interested in tracking the motion of parenchymal tissue adjacent to and above masses to see if this could provide a motion signature for each mass. We specifically examined the interface between masses and adjacent tissue in terms of a motion gradient as a possible means to separate infiltrative and non-infiltrative abnormalities. All examinations were performed with informed consent of patient volunteers, under protocols approved by the institutional review board. Breast masses were diagnosed based on ultrasound, mammography and biopsy results.

Table 5.1: Patient information

Patient #	Age	Menopausal	Mass type	Biopsy	Mass diameter
1	42	pre-	fibrocystic	excisional	3.0 mm
2	46	pre-	fibrocystic	aspiration	10.0 mm
3	30	pre-	fibroadenoma	aspiration	40.0 mm, 20.0 mm
4	59	post	fibrocystic	aspiration	13.0 mm
5	35	pre-	breast nodule	none	7.0 mm
6	43	pre-	amelanotic melanoma	excisional	4.8 mm
7	64	post	invasive ductal carcinoma	excisional	18.0 mm
8	78	post	invasive ductal carcinoma	excisional	3.7 mm

Sonographic features considered in diagnosing benign masses included homogeneity of internal echoes, good margination or definition of edges, non-attenuation of sound through transmission of the mass and the presence of strong anterior echoes while features used in diagnosing malignancy included irregular margination of masses, laterally dense boundary echoes (halo), rough or jagged borders, and the presence of posterior shadowing [81-85]. The composition of the breast parenchyma tissues was also characterized for each patient, based on mammography and ultrasound data unless otherwise stated.

Palpation consisted of three types of motion: simple translation, rocking and compression. Continuous ultrasonic scans of the resulting breast tissue motion were recorded on standard VHS videotape. Serial frames of breast tissue motion through a single palpation cycle were digitized using a commercially available Targa version 2.0 frame grabbing system (Truevision). A sequence of three digitized ultrasound images was acquired for each patient. The digitized gray scale images were ported to a Sun Sparc2 workstation for analysis.

Color images of the tissue displacement field resulting from palpation were computed by centering a rectangular grid of equally spaced points, on the lesion in the first frame of each image sequence. A rectangular kernel region was centered on each grid point and the two-dimensional displacement of each kernel region was tracked through the image sequence using frame-to-frame correlation. By tracking the displacement of various

kernels or regions of tissue at each grid point in the field, a map of displacement vectors representing the tissue displacement field can be generated.

These initial results were computed from ultrasound images of the simple translational motion only. Breast tumors were rated for malignancy by a University of Michigan radiologist on a scale of 0-3, 0 indicating the lesion was most definitely benign and 3 indicating the lesion was most definitely malignant. To simplify the display of tissue displacement fields, only the lateral component of tissue motion, which was the same as the direction of palpation, is shown at this time. Blue areas indicate small tissue displacements (0 - 10.0 mm), yellow areas indicate moderate tissue displacements (10.0 mm - 17.0 mm), and red areas indicate large tissue displacements (17.0 mm - 25.0 mm).

The system allows the user to specify the desired spacing between grid points, kernel dimensions and number of frames in the image sequence. The system requires approximately 45 sec to compute the displacement of a single ROI with dimensions of 3.75 cm x 1.25 cm through a sequence of three images.

5.3 Results

The results of this study consist of 1) gray-scale findings based on ultrasound and mammography data, and 2) displacement maps computed using ultrasound motion analysis. A brief synopsis of these findings are presented in Sections 5.3.1 and 5.3.3 with results from three representative patients. The complete findings from all patients in this study are presented in Sections 5.3.2 and 5.3.4.

5.3.1 Ultrasound images of breast tumors (3 sample patients)

Patient A (#2 in Table 5.1) has a solid benign mass with malignancy rating=1. Benign features on the ultrasound image (Fig. 5.2) included homogeneity of internal echoes, good margination or definition of edges and non-attenuation of sound through transmission.

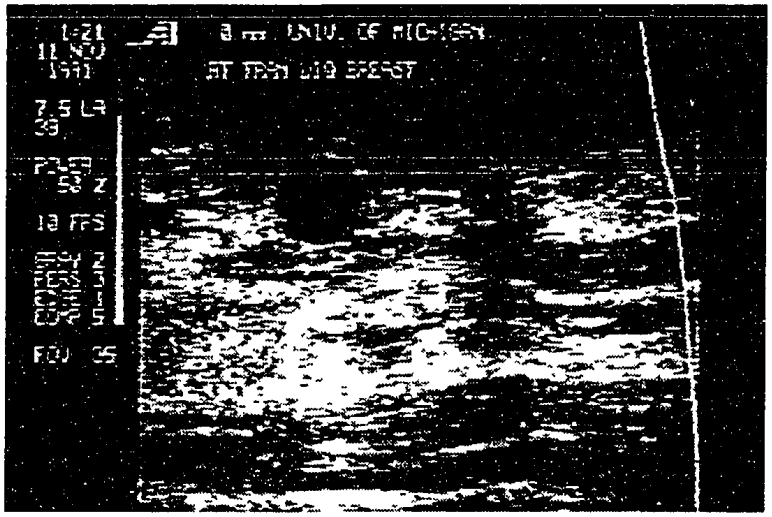

Figure 5.2: Ultrasound from patient A.

The lesion in Patient B (#5 in Table 5.1) contained some benign features, but had irregular margination with suggestion of posterior shadowing. There was poor edge definition with laterally dense boundary echoes (known as halo) compatible with a scirrhus carcinoma with stellate tentacles extending into surrounding tissues (Fig. 5.3). This lesion was given a malignancy rating=2.

Patient C (#6 in Table 5.1) has a lesion which appears to have inhomogeneities of internal echoes with some suggestion of areas of necrosis (Fig. 5.4). It is most likely a metastasis and was given a malignancy rating=3. The lesion appeared to drag adjacent parenchyma when palpated.

5.3.2 Ultrasound images of breast tumors (complete Findings)

The results of this section include findings from ultrasound and mammography data.

Figure 5.5 shows an ultrasound scan of normal breast tissue containing a benign cyst (patient 1, Table 5.1). The mass is well-marginated, anechoic, with well-defined posterior margin and enhanced through transmission, all classic sonographic features of a benign cyst.

Figure 5.6 is a scan of the same plane of the breast at the end of palpation by the physician. The position of the cyst pinpointed by the correlation search algorithm is

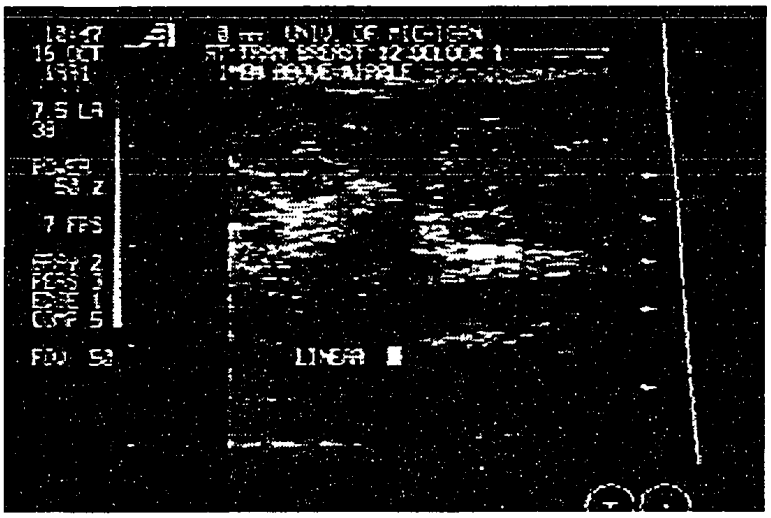

Figure 5.3: Ultrasound from patient B.

highlighted. Motion of a cyst can be seen in ultrasound B-scan images if the cyst is palpated by standard hand techniques. Figure 5.7 indicates the initial and final positions of the cyst shown in Fig. 5.5 and of a section of tissue adjacent to the mass. From Fig. 5.7 it is apparent that there is significant displacement of the lesion due to palpation, but only minimal displacement of the adjacent parenchymal tissue proximal to the transducer.

Gray-scale ultrasound scans for eight patients with breast masses are shown in Figures 5.8 and 5.9. Patient information and biopsy results are summarized in Table 5.1. Patients 1-5 all have solid benign masses based on imaging and biopsy results. Benign imaging features, as discussed earlier, included homogeneity of internal echoes, good margination of edges and non-attenuation of sound through the nodule. The presence of strong posterior echo levels in patients 1-2 and strong anterior echo levels in patient 3 are also typical of benign breast disease, although an area of posterior shadowing was observed below the right mass in patient 3. Mammography results for patient 3 indicated the presence of three nodular densities in the left breast with no suspicious calcifications. A limited ultrasound of the upper, outer quadrant of the left breast in the region of the nodular opacities (Fig. 5.8(c)) revealed two of the solid masses corresponding to the nodules on the mammogram. The largest nodule is indicated by the arrow in Fig. 5.8(c). Needle aspiration biopsy results for patients 1-2 indicated that they were benign

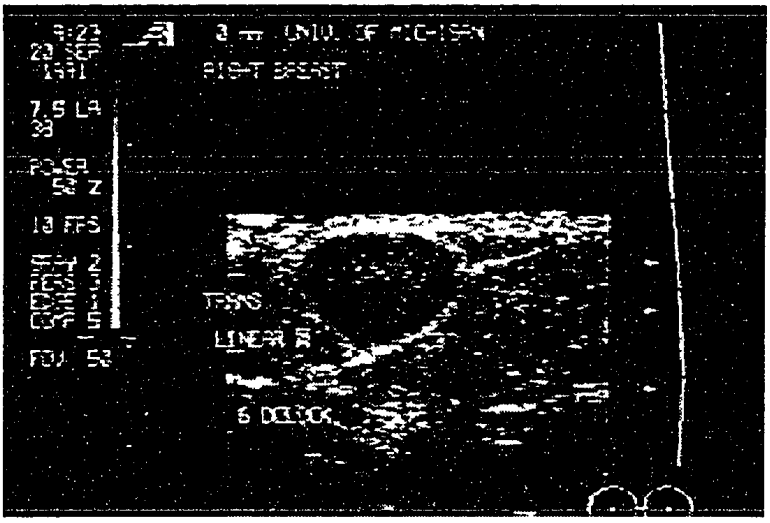

Figure 5.4: Ultrasound from patient C.

fibrocystic masses, while needle aspirational biopsy results for patient 3 revealed myoepithial cells consistent with fibroadenoma. A single 4.2 cm × 3.2 cm × 1.4 cm tissue specimen from patient 1 was also submitted for histological examination. Sectioning revealed a composition of roughly 80% adipose, with one end of the specimen diffusely fibrous and containing a 3.0 mm fluid filled cyst region. The character of the surrounding parenchymal tissue in patient 3 was noted to be composed of a mixture of fatty and fibroglandular tissue based on mammography data and ultrasound images.

Needle aspiration biopsy results for patient 4 indicated a benign fibrocystic mass. Patient 5 had irregular margination with suggestion of posterior shadowing. No biopsy was performed on patient 5; however, this patient was mammographically stable for more than 4 years. The breast parenchyma in patient 4 was characterized as being composed of nodular, moderately dense fibroglandular tissue, while the parenchymal tissue in patient 5 was noted to be composed of predominantly fatty tissues with a small amount of residual fibroglandular tissue.

The lesion in patient 6 appeared to have inhomogeneities of internal echoes with some suggestion of areas of necrosis. Excisional biopsy results for patient 6 indicated it was a metastatic amelanotic melanoma. The lesions in patients 7-8 were irregular marginated masses that appeared to drag adjacent parenchyma when palpated. They had posterior

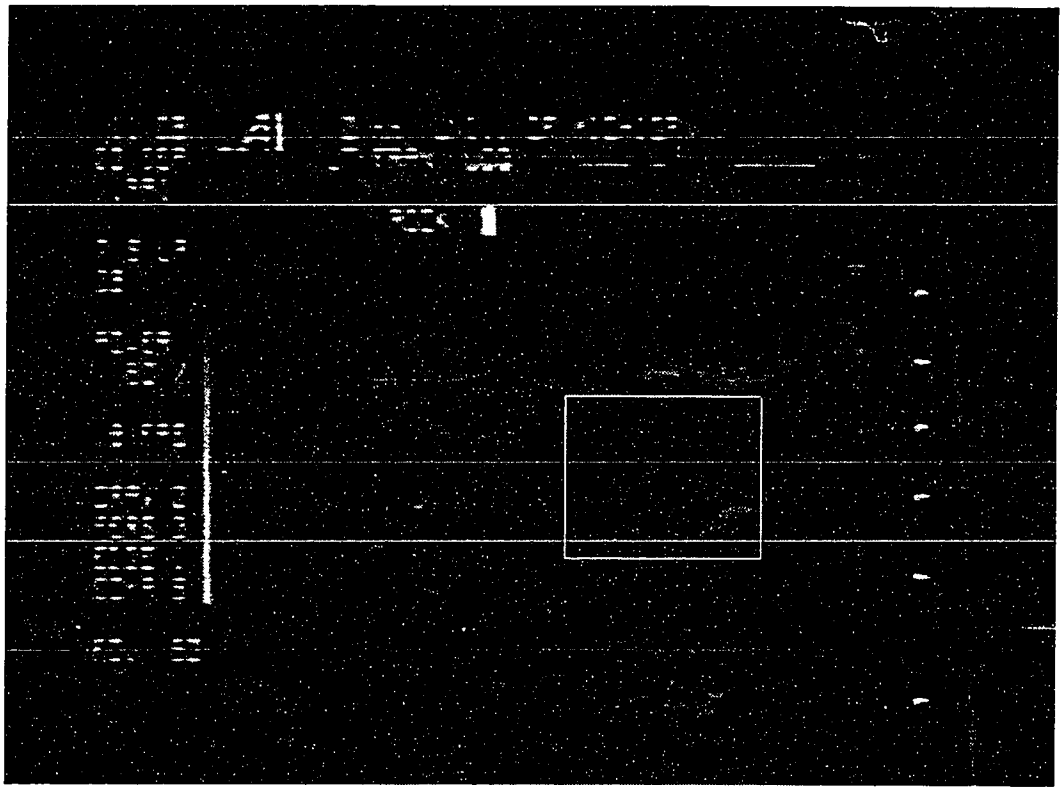

Figure 5.5: Mass before palpation.

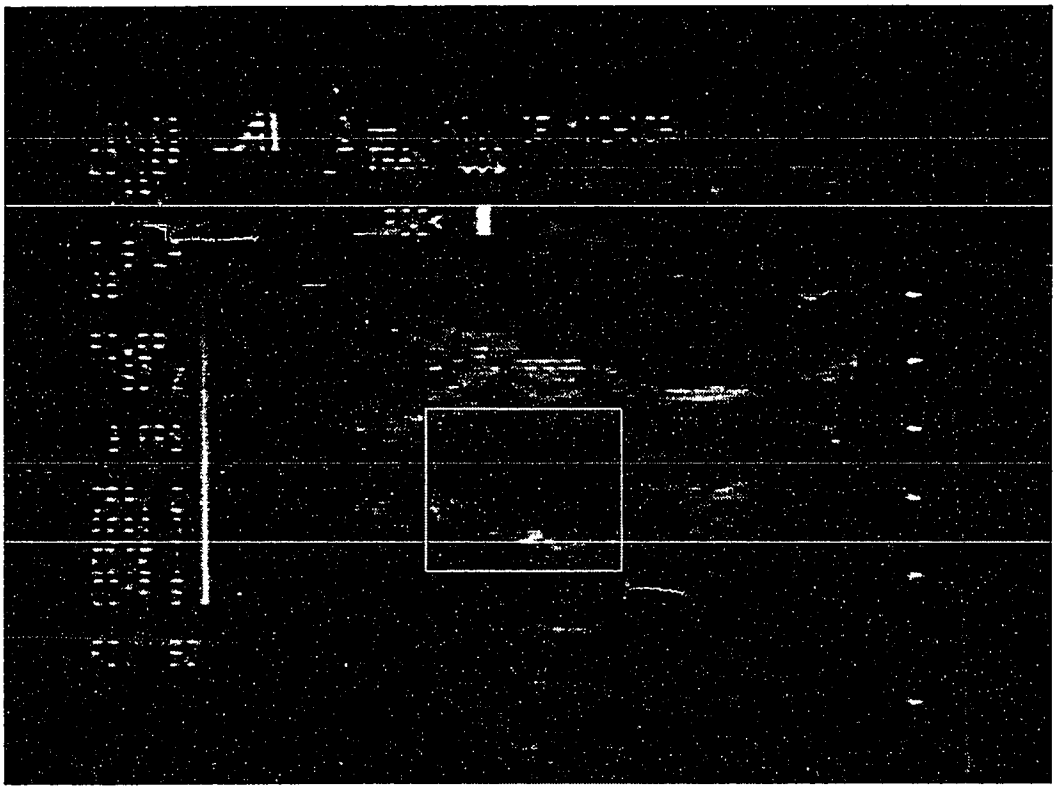

Figure 5.6: Position of mass after palpation pinpointed by correlation search.

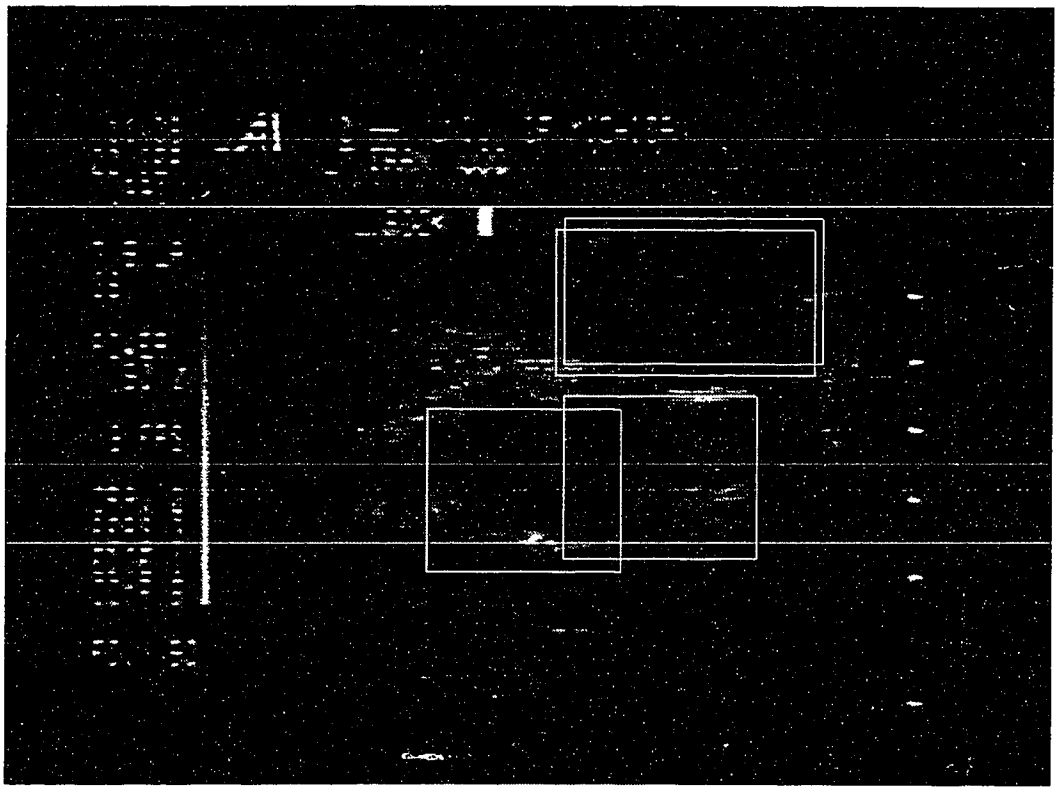

Figure 5.7: Position of mass and adjacent tissue before and after palpation.

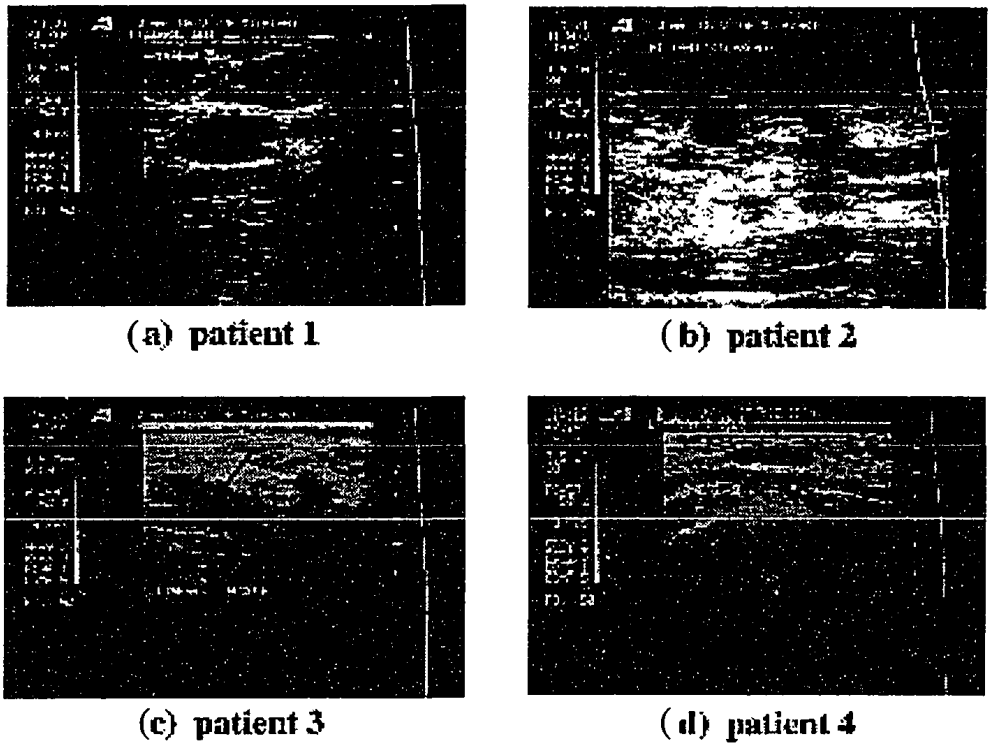

Figure 5.8: Ultrasound images for patients 1-4.

shadowing, halo and other classic sonographic features of malignancy described earlier. Excisional biopsy results for patients 7-8 indicated that they both were invasive ductal carcinomas. The breast parenchyma for patient 6 was characterized as being composed of predominantly fatty tissues, while patients 7-8 were reported to be composed of mixed fatty and fibroglandular tissues.

5.3.3 Displacement images of breast tumors (3 sample patients)

Displacement fields consists of a 100 × 100 grid of points or displacement vectors centered on the lesion at the start of palpation. Orientation is the same as the diagnostic ultrasound images with top to bottom corresponding to depth or axial distance from the transducer and left to right corresponding to the direction lateral to the beam axis. All palpations were from the left to right direction.

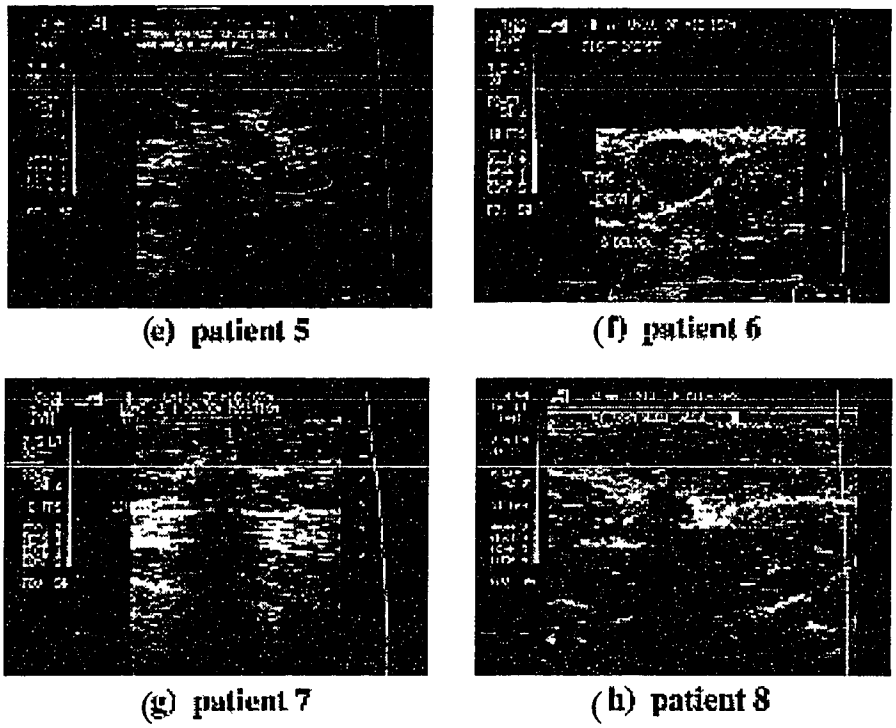

Figure 5.9: Ultrasound images for patients 5-8.

Color images of tissue displacement fields exhibited regions of red then yellow then blue when looking across the color map from left to right. This indicates that the largest tissue displacement occurred for tissues on the left side of tumors and that small displacements occurred in the tissues on the right side of tumors. This is consistent with the left to right palpation and the fact that tissues closest to the point of palpation contact should translate the most, while tissues farthest away should translate the least.

Observing the displacement maps from top to bottom a blue-red border was visible for the benign mass in patient A (see Fig. 5.10), indicating a slip boundary and suggesting shear motion opposite to the direction of palpation. Resolution of the map was approximately 0.25 mm per pixel.

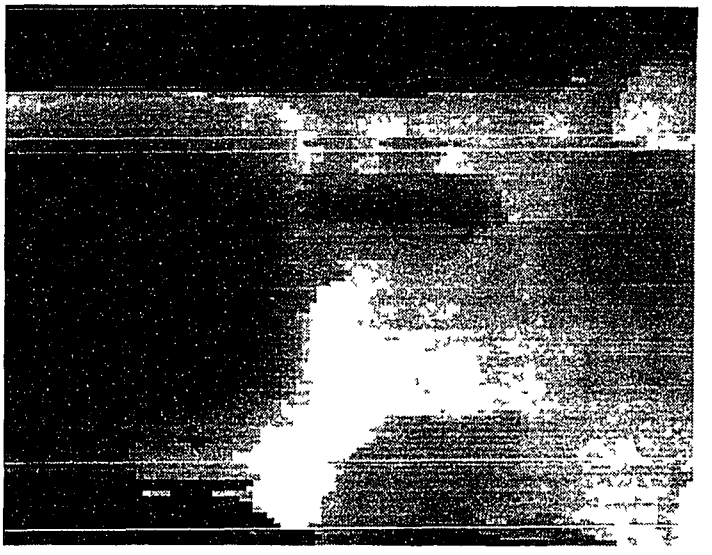

Figure 5.10: Displacement images for patient A.

The gradual shading from blue to light blue to red looking at the displacement field of patient B (Fig. 5.11), from top to bottom, suggests a drag displacement of tissues near the periphery of the lesion with a malignancy rating=2

The displacement field of patient C (Fig 5.12) indicates a total lack of slip boundary, but further shows a very strong dragging of adjacent parenchymal tissues in the direction of palpation, which suggests the possible presence of an infiltrative component to the mass.

5.3.4 Displacement images of breast tumors (complete findings)

Ultrasound computed displacement maps, shown in Fig. 5.13, were generated using a field grid spacing of 0.25 mm per pixel. In each case a rectangular kernel with dimensions approximately equal to the size of the lesion area was used in the correlation tracking. The grid spacing, field sizes and kernel sizes used for all patients are summarized in Table 5.2.

Figures 5.13(a)-(h) are color maps of the tissue displacement field for the corresponding masses seen in Figures 5.8 and 5.9, respectively. Each displacement field consists of

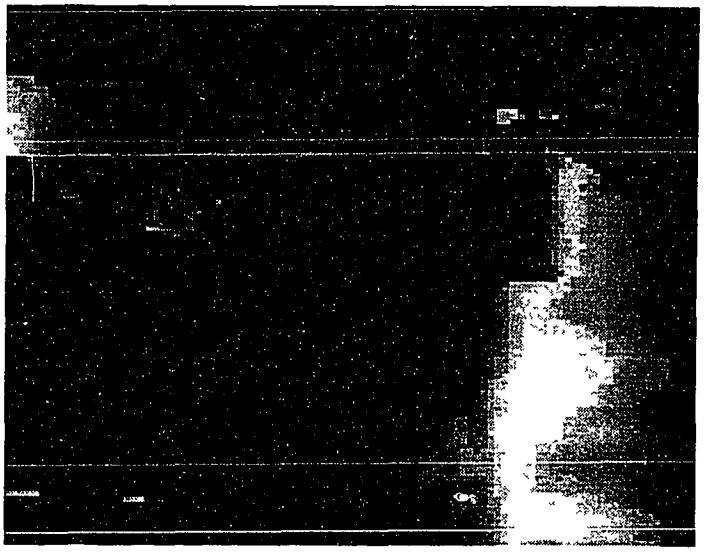

Figure 5.11: Displacement image for patient B.

a 100 × 100 grid of points or displacement vectors centered on the lesion at the start of palpation. A 50 × 100 grid was used for patients 4 and 7 because of the smaller available field of view in the ultrasound images. The orientation of the color maps is the same as used in the diagnostic ultrasound scans with top to bottom corresponding to depth or axial distance from the transducer and left to right corresponding to the direction lateral to the beam axis. All palpations were from the left to right direction. Based on the palpation applied (translational motion of the transducer over breast masses), three types of motions were observed and these included: 1) slip motion (shear motion of adjacent tissue above mass, opposite to the direction of palpation), 2) slight drag (small displacement of adjacent tissue in the direction of palpation) and 3) fixed translation (en-bloc displacement of mass and adjacent parenchyma).

Color maps of tissue displacement fields exhibited regions of red then yellow then blue when looking across the color map from left to right. This indicates that the largest tissue displacement occurred for tissues on the left side of tumors and that small displacements occurred in the tissues on the right side of tumors. This is consistent with the left-to-right palpation and the fact that tissues closest to the point of palpation contact should

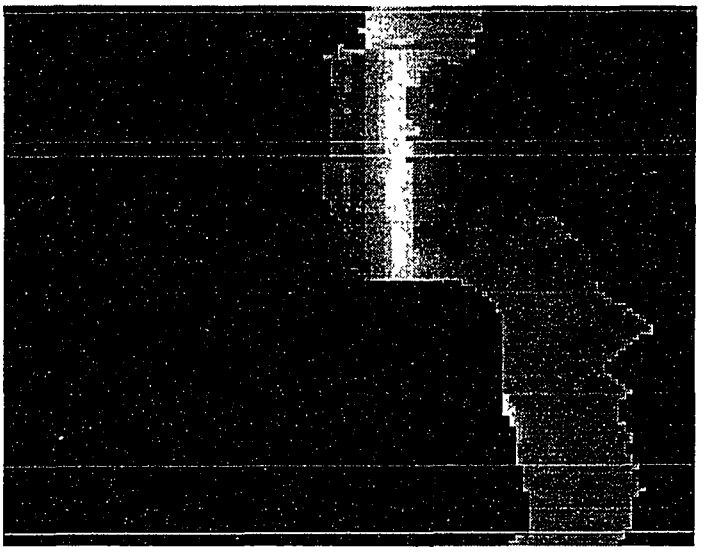

Figure 5.12: Displacement image for patient C.

translate the most, while tissues farthest away should translate the least. In Fig. 5.13(c) the presence of the blue band on the left side of the color map represents the left side of the image in Fig. 5.13(c). Because the starting position of the mass in Fig. 5.13(c) was on the left edge of the image, displacement of tissues to the far left of the lesion could not be estimated.

Table 5.2: Displacement tracking parameters

Patient #	Field size (points)	Grid spacing	Kernel dimensions
1	100 × 100	0.25 mm	25.0 mm × 12.5 mm
2	100 × 100	0.25 mm	10.0 mm × 10.0 mm
3	100 × 100	0.25 mm	25.0 mm × 12.5 mm
4	50 × 100	0.25 mm	18.7 mm × 6.3 mm
5	100 × 100	0.25 mm	15.0 mm × 12.5 mm
6	100 × 100	0.25 mm	20.0 mm × 15.0 mm
7	50 × 100	0.25 mm	12.5 mm × 15.0 mm
8	100 × 100	0.25 mm	10.0 mm × 8.8 mm

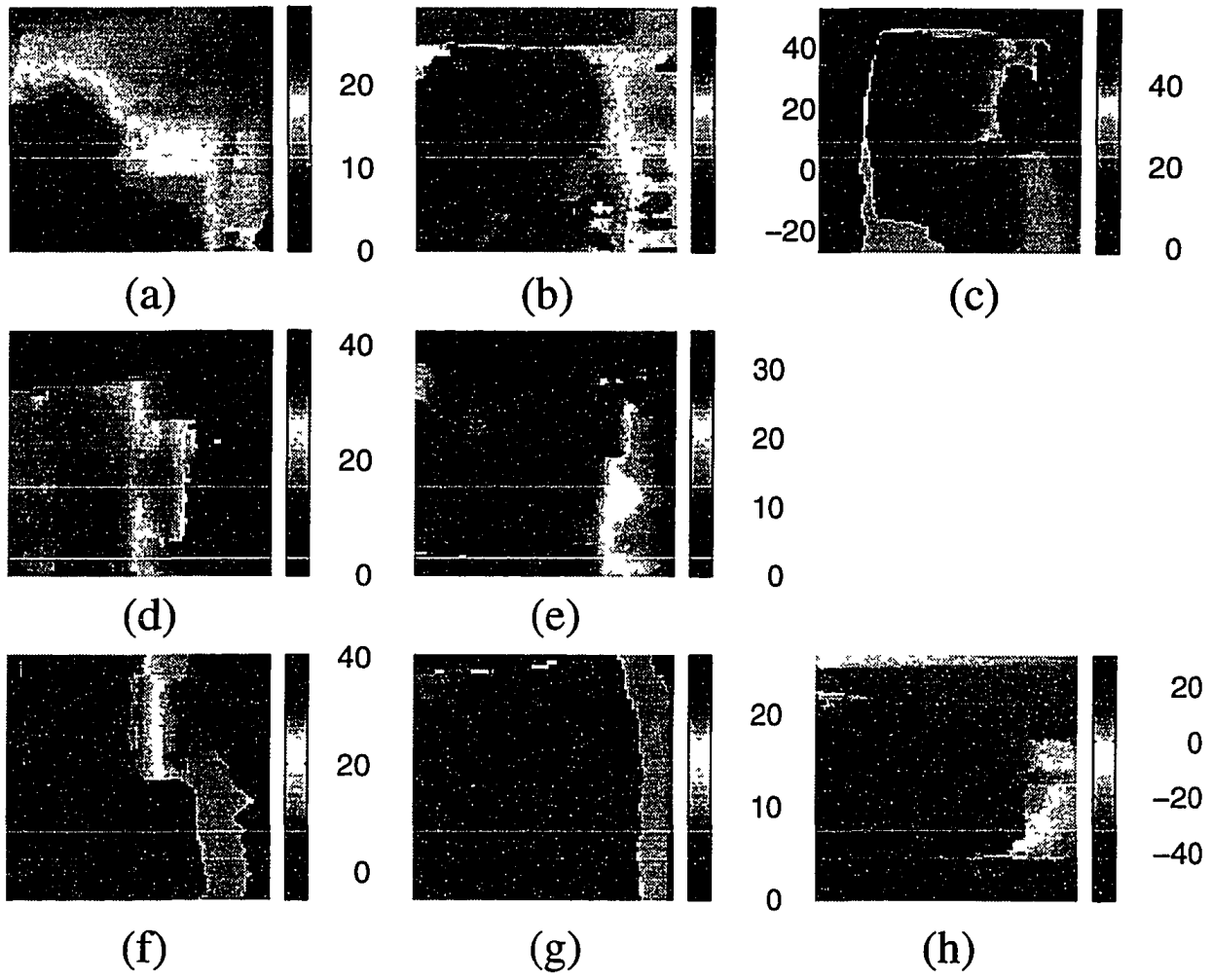

Figure 5.13: Displacement images for patients 1-8.

In order to obtain a more quantitative measure of tissue motion, the average displacement for each patient was computed along the center axial slice of each displacement field. The average displacement was computed in two windows. Window A extended from a depth of 0 pixels to 25 pixels (6.25 mm) and is representative of tissue motion directly above masses. Since the transducer was used to impart a shear force on the tissue directly above masses, motion in this region was of particular interest. Window B extended from a depth of 25 pixels to 100 pixels (18.75 mm) and is representative of the displacement of masses. The adjacent tissue (perilesional) displacement (window A) and mass displacement (window B) for all patients are presented in Table 5.3.

Table 5.3: Mean adjacent tissue and mass displacement

Patient#	Mass type	Perilesional displacement (pixels)	Mass displacement (pixels)
1	benign	28	43
2	benign	13	46
3	benign	34	57
4	benign	25	41
5	benign	10	54
6	malignant	44	56
7	malignant	53	60
8	malignant	14	40

5.4 Clinical Significance

The limited resolution of ultrasound does not allow imaging of any possibly invasive tentacles extending from a tumor site. However, imaging of tissue motion can provide important clues in the early detection of invasive tumor growth into surrounding tissues. The cystic mass in Fig. 5.2 displayed discontinuous motion between the mass and adjacent tissue. Such a feature would be typical of a slip boundary and was present in all cases of fibrocystic disease.

It would be diagnostically useful for a physician to observe the motion of surrounding tissue as a lesion is palpated, since many breast cancers, such as scirrhus carcinoma, infiltrate into surrounding tissues. Palpation of these cancers results in apparent dragging of the adjacent parenchymal tissues. Ultrasound tracking of tissue motion provides a strong tool in aiding the physician in observing motion of adjacent parenchymal tissues and in reducing errors due to visual errors and artifacts.

5.5 Observed Motion Responses

Three basic types of motion were observed (slip, slight drag, fixed translation) and were consistent with the physiological growth patterns of masses and histological information discussed earlier. A red-blue border was visible in all five benign masses indicating

discontinuous motion and consistent with a slip boundary. The presence of light blue regions in patients 5 and 8 (Fig. 5.13) indicates a slight drag with small displacement of adjacent tissue following palpation of the mass. Patients 6-7 (Fig. 5.13) depict fixed translational motion, with en bloc motion of adjacent parenchyma as the mass is palpated and suggestive of an infiltrative component to the mass. This was consistent with histology results which indicated invasive ductal carcinoma and was also compatible with margins seen on mammography.

The quantitative characterizations of the motions observed are consistent with the qualitative results seen in previous studies [69, 71, 72]. The present motion analysis also better defines such motion and perhaps more importantly may eventually allow the remote characterization of lesion boundaries in deeply situated lesions, even with relatively small displacements based on the ability of speckle tracking algorithms to track relatively fine motions [44].

All five benign fibrocystic masses produced motions as might be expected for slip boundaries or no particular anchoring to surrounding tissues. Tissue displacement images exhibited fixed translational motion for two of the three malignant tumors.

In the present study, the transducer was used to impart a shear force on the tissue directly above masses. We were particularly interested in tracking tissue motion in this area in order to investigate the premise that infiltrating malignancies might alter motion responses. Based on our limited patient size, we observed an increased adjacent tissue displacement for malignant masses. This difference was particularly noticeable for patients 6-7 relative to the benign masses (Table 5.3). Although there is considerable variability between patients and masses, our results suggest that palpation of malignancies can result in dragging or fixed translation of adjacent parenchyma, consistent with qualitative expectations. Future studies with increased population sizes will be necessary to ultimately determine if there is a statistical trend towards more translation for malignancies. A normalized index such as relative adjacent tissue motion per mean mass displacement may also be useful since this would roughly quantitate the percent drag of masses and adjacent parenchyma.

5.6 Resolution Versus Accuracy Tradeoff

For color maps of tissue displacement, selecting small kernel dimensions provides more localized motion information. However, the accuracy of correlation tracking is generally inversely proportional to the kernel size [42]. Thus resolution or localization of motion information is traded off against accuracy of results as kernel dimensions are adjusted.

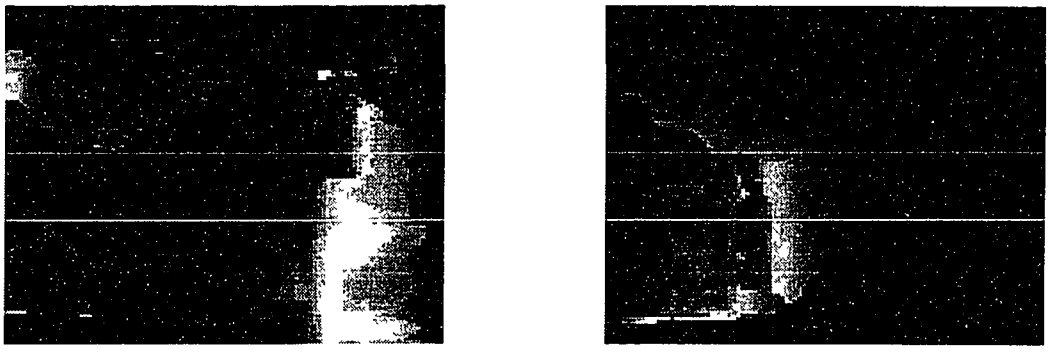

Figure 5.14: Effect of kernel size on displacement images.

Figure 5.14 illustrates the effect of two different kernel sizes on the displacement images, for patient #5. Kernel sizes of 4.0 cm × 2.0 cm and 2.0 cm × 2.0 cm were used. By keeping the grid spacing constant (distance between the center of kernels) increasing the kernel dimensions apparently has the effect of smearing the displacement field. This is apparent in Fig. 5.14 where the lateral kernel dimensions have been doubled, but where the axial dimensions were not changed. Notice that the axial dimension of the displacement fields is not significantly different for the two kernel sizes. The smearing effect using large kernel dimensions results from an increasing amount of overlap for a fixed grid spacing.

The grid spacing can be made arbitrarily small by simply increasing the total number of grid points (and reducing the distance between grid points). The grid spacing is ultimately limited only by the pixel resolution of the digitized ultrasound images (0.25 mm per pixel). A small grid spacing will provide a higher spatial resolution in maps

of tissue displacement and velocity. However, the resulting increase in grid points will require additional computations.

The preliminary results in this chapter are intended as a demonstration of the tissue displacement imaging technique. Displacement fields from breast tumors are used to demonstrate a potentially useful application of the method. It must be stressed that there are many biological and physical factors which can influence the connective tissue motion response to palpation. The structure of the parenchymal tissue surrounding the breast mass can alter the degree of motion response. In addition, the motion response from a stellate mass in a 40-year-old pre-menopausal patient can be expected to be different than the motion response of the same mass in a 75-year-old patient.

The position of the patient during examination and location of the mass within the breast are also important and can influence the motion response to palpation. For example, a thin mass located in a lateral plane or in the lateral aspect of the breast may require a patient to be rotated on her hip in order to obtain a reasonable image of the mass. If the patient is not rotated, then the motion response of the perilesional tissue can be expected to be different for palpations along different aspects of the mass.

Finally, the motion response of tissue to palpation may also be influenced by the character of the tissue adjacent to the mass, whether the mass is situated in a bed of soft fatty tissue or in an area of dense glandular tissue and the fatty constituency of the breast. For example, for the case of a hard inclusion imbedded in an area of fatty tissue, the inclusion can be expected to deform less than the surrounding tissues as the tissue is compressed. Similarly, for the case of a soft tissue inclusion embedded in dense glandular tissue, the opposite will be true and the inclusion will absorb most of the deformation. The motion response to palpation will therefore also depend on the character of the surrounding parenchymal tissues (whether they are soft or stiff) and the relative difference between the tumor and tissue elastic moduli. In our motion studies we observed that larger displacements seemed to occur in patients with predominantly fatty breast parenchyma (patients 5-6), with smaller overall displacements observed in

breast parencyhma containing predominantly glandular tissue or a mixture of fatty and glandular tissues (patients 1-4).

5.7 Limitations and Problems

There is clearly a natural variability of motion responses from patient to patient due to tissue constituencies, tumor size, shape and depth in three dimensions, the imprecise manual palpations applied by different radiologists and out-of-plane tissue motion. A more exhaustive study would have to take these differences into account to determine if these are indeed important variables. The results presented here represent a first step towards representing motion information in a more objective manner. The next step might be to attempt a normalization for major biophysical factors such as separation between driving surfaces on the skin, distance moved, size and distance of masses from surface and basic tissue type surrounding masses. Whether standardization of the applied motion will be more effective than application of a maximum comfortable local stress and compensation with normalization remains to be seen.

Recent research has focused on the development of quantitative methods for applying more precise or known palpations for tumor elasticity measurement. Cespedes et al. (1993), in particular, have experimented with applying a known fixed and uniform compression to the breast using modified mammography equipment and others have designed a technique for interactively determining a good, high stress to be applied quantitatively [73, 74, 75]. In addition, new techniques developed for three-dimensional motion tracking and strain imaging will help reduce problems in tracking and analyzing complex deformations and out-of-plane motions [3, 44, 76].

A new area of research in ultrasound is elasticity imaging. The basic idea in elasticity imaging is similar to displacement imaging. However, instead of tracking the motion of small regions of tissue, the concept is to track dimensional changes in small areas or volumes of tissue as the tissue is compressed. The premise is that this can provide information about tissue mechanical properties. To measure area or volume changes in small rectangular regions of tissue, speckle tracking and Fourier techniques have been

applied to measure tissue displacement fields [3, 4]. Tissue displacement imaging thus also represents a necessary step in the elasticity imaging process.

5.8 Concluding Remarks

It would be diagnostically useful for a physician to observe the motion of surrounding tissues as a lesion is palpated, since many breast cancers, such as scirrhus carcinoma, infiltrate into surrounding tissues. Palpation of these cancers results in apparent dragging of the adjacent parenchymal tissues. Ultrasound tracking of tissue motion would provide a strong tool in aiding the physician in observing motion of adjacent parenchymal tissues, and in reducing errors due to visual errors and artifacts. The limited resolution of ultrasound does not allow imaging of any possible invasive tentacles extending from the tumor site. However, imaging of tissue motion can provide important clues in the early detection of invasive tumor growth into surrounding tissues. Tissue displacement images indicated a dragging of perilesional tissue by the tumor for 3 of 3 malignant tumors. Tissue displacement images further showed the presence of slip boundaries and no dragging of parenchymal tissues in 4 out of 5 benign masses.

Our preliminary results suggest that tissues near the periphery of malignant breast lesions undergo a dragging motion, suggesting that they are being pulled in the direction of motion when the tumor is palpated. This is consistent with the notion that many malignant tumors grow in an infiltrative manner. Perilesional tissues in benign breast tumors displayed a shear motion opposite to the direction of palpation, suggesting a slip boundary and the absence of stellate roots. Tissue displacement images of an invasive ductal carcinoma showed fixed translational motion of the surrounding parenchyma when the tumor was palpated, consistent with histological data and known physiological patterns of growth. Tissue displacement maps of benign fibrocystic masses exhibited slip motion that was present in all cases of fibrocystic disease.

Our present work is essentially based on the following facts and assumptions:

- The presence of a stellate or star-shaped mass is one of the most distinct mammographic features of a breast malignancy.
- Stellate neoplasms alter tissue motion responses to palpation compared to non-invaded tissues.
- Ultrasound provides a means for accurate real-time imaging of local tissue displacements.
- Altered tumor and connective tissue responses can be quantified and potentially used for early detection and classification of breast cancers.

CHAPTER 6

TISSUE ELASTICITY MEASUREMENTS

Ultrasound elasticity imaging is a promising method that may eventually allow early detection of many tissue pathologies. However, before elasticity imaging can be applied to its numerous potential clinical applications, the quantitative accuracy of tissue elasticity measurements must be established. Simple one-dimensional ultrasound elasticity measurements were performed on muscle and liver and compared with independent and established mechanical measurements to investigate both the accuracy and consistency of ultrasound elasticity measurements. In addition, some interesting properties of soft tissue and aspects of the measurement process, which should be considered in elasticity measurements, are discussed. The work in this chapter provides a benchmark comparison between ultrasound and Instron elasticity measurements.

6.1 Background

The goal of this chapter is threefold: 1) to establish the accuracy of ultrasound elasticity measurements under simple test conditions, 2) to provide elasticity values for two important tissues (muscle and liver), and 3) to investigate several interesting aspects of the measurement process that should be considered in elasticity measurements. Tissue elasticity imaging has direct relevance in the early detection of breast and prostate cancers and liver cirrhosis; diseases which are believed to significantly alter tissue elasticity.

Previous measurements of tissue elastic properties are limited and have spanned a wide range of values. Elasticity measurements have been reported for tendon, heart, skin and cartilage; however, quantitative values for muscle, liver and fat are still lacking [59, 60]. To test both the accuracy and consistency of ultrasound measurements, Young's modulus (YM) values for muscle and liver are compared with independent mechanical measurements made using the Instron load cell device. The results of this study have two major implications. First, they contribute to the limited quantitative data currently

available about muscle and liver elastic properties. Second, by comparing ultrasound elasticity measurements with established mechanical measurements, we have a basis for determining the quantitative accuracy of ultrasound elasticity values.

6.2 Methods

Six bovine muscle and three bovine liver samples were were obtained from the Meat Sciences Laboratory, Department of Animal Sciences at the University of Illinois. Muscle samples were excised from the beef longissumus dorsi (LD) muscle of a USDA select grade animal and were approximately 4 cm × 4 cm in length and width, with thicknesses ranging from 1-2 cm. Tissue samples were packed in ice and transported to the Bioacoustics Laboratory for experiments within 48 hr of death. Muscle samples had an angled fiber orientation leaving fibers neither parallel nor perpendicular to the sides. Three fat samples were also obtained following the procedures described above.

Three samples of ultrasound tissue mimicking gel standoff material and two types of sponges were also used in test measurements. Gel standoff samples were made of poly-vinyl-chloride (PVC) shor value #4, and were sliced into rectangles with surface dimensions and sample thicknesses ranging from 2-4 cm. Sample A was cut into a rectangular block with dimensions of 2.0 cm × 2.0 cm × 2.5 cm. Sample B was cut into a rectangular block with dimensions of 2.5 cm × 3.5 cm × 2.5 cm. Sample B2 was cut into a rectangular block with dimensions of 2.5 cm × 2.5 cm × 3.5 cm. Sponge samples consisted of square sections of cellulose and urethane sponge. Sponge samples were sliced into approximately 2.5 cm squares with thicknesses ranging from 3.5 cm to 6.0 cm.

6.2.1 Ultrasound measurements

Ultrasonic elasticity measurements were made using a single transducer setup. Samples were placed on the pad of a Taconic Farms model YG-700 rat scale. A 2.5 MHz circular, unfocused Panametrics transducer with 3.18 cm diameter was attached to the

robotic arm of a Daedal motorized positioning system and aligned to perform uniaxial compressions. The system is computer controlled and has five degrees of freedom. The transducer was positioned to be in light contact with the sample. Precise axial compressions were made in 0.5 mm increments until a total deformation of approximately 5% was reached. After each incremental compression, a 1025 point A-line was digitized at 50 MHz using a model 11401 Tektronix digitizing oscilloscope. Scale readings were used to compute the equivalent applied stress after each incremental compression.

Figure 6.1: Instron load cell device.

Data were then transferred to a Sun Sparc2 workstation. Incremental tissue strains were computed from time-of-flight (TOF) measurements of an ultrasonic pulse using Equation (6.1), where t_i represents the roundtrip TOF of the pulse after the ith compression.

$$\epsilon_i = \frac{\Delta L}{L} = \frac{t_0 - t_i}{t_0} \tag{6.1}$$

Scale readings were used to compute the equivalent applied stress after each incremental compression. By measuring the strain for several different applied stresses, the stress-strain behavior of samples was characterized and the YM was estimated from the slope of the curve in the linear region of sample stress-strain curves. YM values of samples were calculated from the initial linear region (up to 5% strain for tissue samples and 10%

strain for PVC) of the curves using a least squares fit. YM values were calculated from a larger strain range for the PVC samples since they exhibited a larger linear elastic region. All measurements were made at room temperature ($22°C$) after Aquasonic coupling gel was applied to lubricate contact between the transducer punch and muscle samples.

Figure 6.2: Axial punch compression test.

6.2.2 Instron load cell measurements

Precise load-deflection measurements were made using an Instron Universal Testing Instrument, model 1122 (Figures 6.1 and 6.2). Axial compressions were made using a circular 5.7 cm diameter aluminum punch crosshead with crosshead velocity set to 5 cm/min, chart speed set to 500 cm/min and full scale deflection on the chart set to 1 kg.

The Instron crosshead was set to reverse direction when the punch reached a deformation equivalent to approximately 10% of the sample thickness. The surface dimensions of all samples allowed the samples to fit completely under the Instron aluminum punch crosshead which had a 5.7 cm diameter. This enabled a uniform stress to be applied and reduced the possibility of stress non-uniformities at sample edges. Instron punch and sample surfaces were lightly lubricated to prevent bonding between the sample and punch. All measurements were made at room temperature ($22°C$).

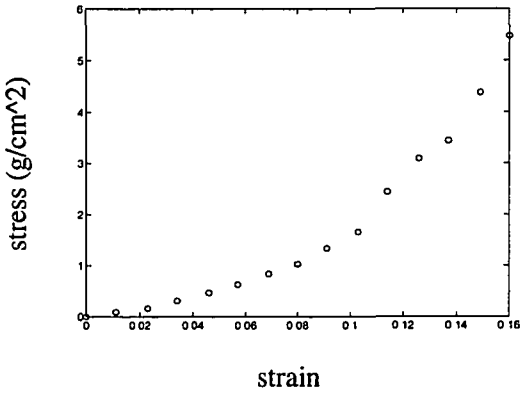

Figure 6.3: Instron muscle sample stress-strain curve.

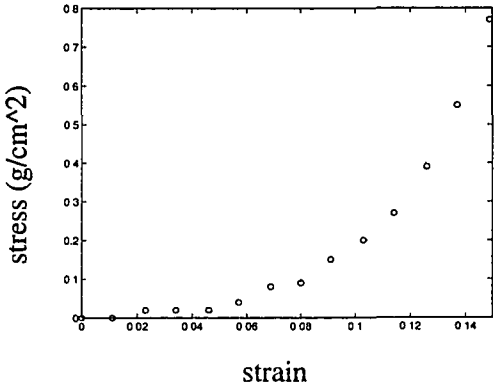

Figure 6.4: Instron liver sample stress-strain curve.

Typical force-deformation curves obtained from bovine LD muscle and liver and PVC sample A with the Instron load cell device are shown in Figures 6.3. - 6.5. The raw data produced by the Instron load cell is a plot of load (kg) versus deformation (mm). The axes in Fig. 6.3. have been normalized to represent stress (Pa) versus strain (dimensionless).

The stress-strain curve obtained from ultrasound measurements of the same muscle, liver and PVC samples are shown in Figures 6.6. - 6.8.

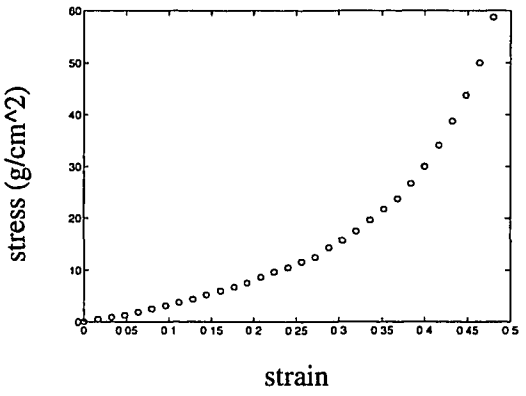

Figure 6.5: Instron PVC sample stress-strain curve.

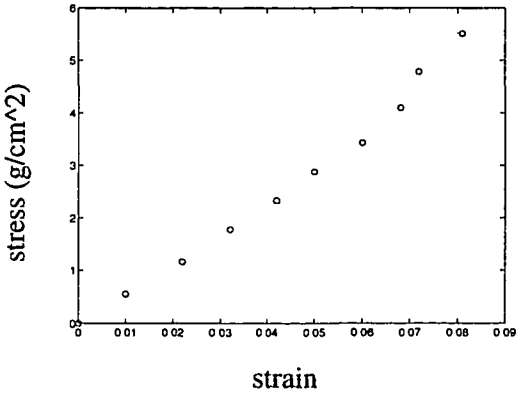

Figure 6.6: Ultrasound muscle sample stress-strain curve.

6.3 Tissue Stress-Strain Curves

The exponential shape of the stress-strain curve in Fig. 6.3 is characteristic of many materials including soft tissues [60]. An initial linear elastic region of the stress-strain curve was observed for tissue strains up to 5%, although a linear region up to about 3% tissue strain was observed for most other samples. The Young's modulus estimated from the initial linear region of this curve was approximately 2.9 kPa. For tissue strains exceeding 10% the deformation enters the non-linear elastic region of the stress-strain curve. As the load is increased, the exponential stress-strain behavior suggests a strain

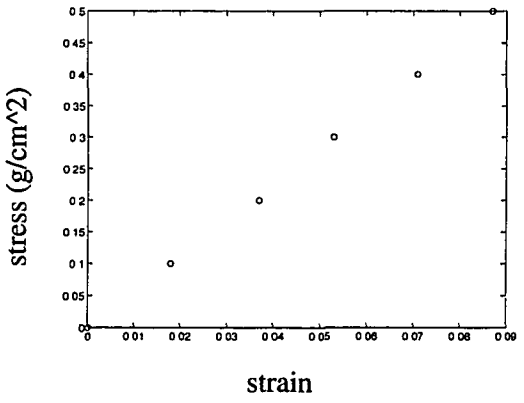

Figure 6.7: Ultrasound liver sample stress-strain curve.

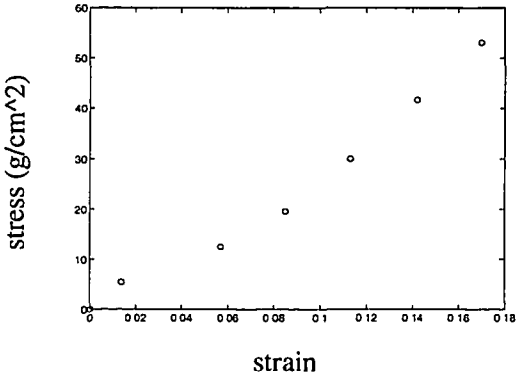

Figure 6.8: Ultrasound PVC sample stress-strain curve.

hardening effect. This strain hardening has also been observed in elasticity measurements of anterior cruciate ligaments, the aorta, psoas major tendon and pericardium [59, 60].

If the sample is compressed further, we will eventually pass the elastic limit of the sample (largest applied stress for which the material will behave elastically) and enter the plastic region of the curve. At this point, the compression on the sample by the load results in permanent plastic deformation of the sample. Even after the load is removed, the sample will not return to its original shape.

Table 6.1: Elasticity values

Sample Type	Sample #	Strain Range for YM	Ultrasound YM (kPa)	R^2	Instron YM (kPa)	R^2	Relative Error
muscle	LD-122I	1-5%	3.15	0.981	1.8	0.986	75%
muscle	LD-122J	1-5%	1.74	0.995	1.6	0.985	9%
muscle	LD-122K	1-5%	1.46	0.984	1.2	0.994	22%
liver	125A	1-5%	0.35	0.988	0.43	0.77	19%
liver	126A	1-5%	0.79	0.993	0.72	0.847	10%
liver	117A	1-5%	0.72	0.949	1.68	0.927	57%
PVC	A	1-10%	30.9	0.957	33.7	0.998	9%
PVC	B	1-10%	30.7	0.932	32.3	0.973	5%
PVC	B2	1-10%	40.1	0.988	53.9	0.990	34%

6.4 Benchmark Comparison

The YM values for all samples measured are shown in Table 6.1. All YM values are unconstrained values. The average ultrasound and Instron YM of muscle samples were 2.12 ± 0.91 kPa and 1.53 ± 0.31 kPa, respectively, with an average relative error of 35%. The average ultrasound and Instron YM of liver samples were 0.62 ± 0.24 kPa and 0.94 ± 0.65 kPa with an average relative error of 29%. The average ultrasound and Instron YM of PVC samples was 33.77 ± 5.49 kPa and 39.97 ± 12.09 kPa with an average relative error of 16%.

Relative errors in YM measurements were typically on the order of 50% (Table 6.1). However, it should be remembered that differences in the YM of different tissues can span an extremely large dynamic range of elasticities [32, 59], so even with a 50% error, differential diagnosis based on elasticity imaging may still be useful. In addition, YM measurements of muscle, liver and PVC showed agreement between the two methods as to which samples were the hardest (PVC) and softest (liver). Ultrasound elasticity measurements thus appear to provide reasonable consistency (high R^2 values indicating consistent YM estimates at different strain levels and ability to differentiate materials with 1 order of magnitude difference in YM, i.e., tissue and PVC), using Instron mea-

surements as a reference. Non-linear behavior of tissue samples probably contributes to differences in YM values. For example, PVC samples exhibited much larger linear elastic regions, and relative errors for these samples were significantly lower (Table 6.1). Differences in measured YM values may also simply indicate a systematic difference or systematic experimental error between the two methods. For example, the Instron device exhibited poor sensitivity and resolution in measuring the lower stresses and strains of the tissue samples. In addition, it was difficult to exactly reproduce initial conditions (initial deformation or strain on samples at contact, etc.,) for both sets of measurements.

6.5 Correction Factor with Constrained YM

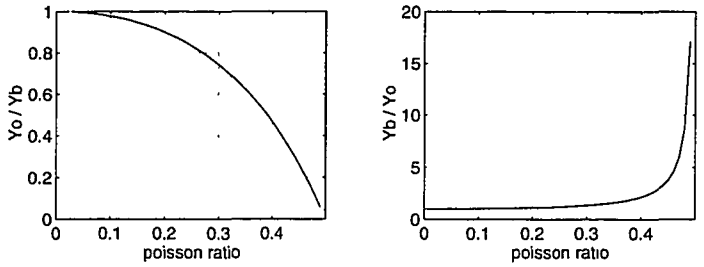

(a) (b)

Figure 6.9: Ratio of YM to constrained YM for different values of ν.

In elasticity measurements, it is important that samples remain unconfined or unconstrained laterally as they are compressed axially. If samples are constrained laterally then the constrained YM (Y_b) will be larger than the unconstrained YM (Y_o). The constrained YM Y_b, is related to the unconstrained YM Y_o according to the equation

$$\frac{Y_o}{Y_b} = 1 - \frac{2\nu^2}{1-\nu} = C \tag{6.2}$$

where ν represents the Poisson ratio of the material. C, therefore, represents a correction factor between the constrained and unconstrained cases. The ratio of Y_o to Y_b is plotted in Fig. 6.9 for various values of ν. In vivo elasticity measurements will more closely

resemble those for the constrained case. For compression made with a small compressor, the situation can be modeled as in the uniform compression case with the tissue below the compressor surface being constrained by the surrounding tissue. In other words, the small compressor case can be modeled as a uniform (large compressor size) compression case with the sample confined. In this case the tissue directly under the small compressor is confined by the surrounding tissue. Therefore a numerical analysis should be performed in these cases (Equation. (6.2)) to account for the small compressor size and constraining effect based on the transducer geometry and size [77].

6.6 Preconditioning

It is also important to consider the effect of preconditioning on tissue elasticity measurements. When cyclic loading/unloading tests are performed on soft tissues (ligament and tendon) hysteresis of tissue stress-strain curves can occur [59]. We have also observed this effect in muscle and liver tissue (Figure 6.10) [78].

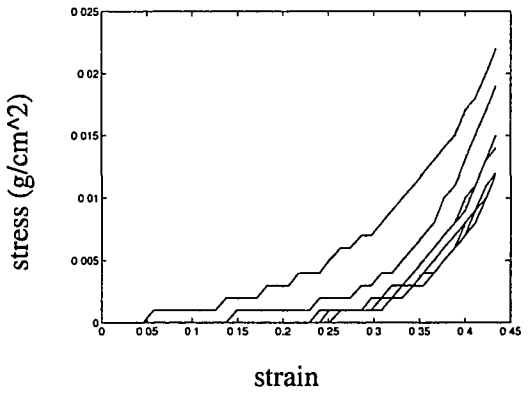

Figure 6.10: Hysteresis effect in compression test of muscle sample.

The YM measurements performed on unconditioned tissue may be indicative of the tissue pseudo-elastic properties and subject to large uncertainties since they are representative of tissue elastic properties during a particular loading cycle. Our initial studies indicate that by subjecting muscle and liver tissue to a specified pre-conditioning cycle

(cyclic loading and unloading), the hysteresis effect can be reduced [78]. It may thus be necessary to first pre-condition tissue in practical elasticity measurement situations.

6.7 Strain Levels

We have observed that YM values computed by averaging measurements from multiple strain levels seem to significantly reduce uncertainties in YM values. Since the present ultrasound measurements are a simple case of elastography [4], where the Young's modulus is estimated from a single point on the stress-strain curve, it may be useful to perform elastography type measurements using multiple compression levels, taking care to maintain strains within the linear elastic region of tissue samples.

It is clear that the strain level applied in elasticity measurements is very important. Because of the strain hardening effect observed for soft tissues, strains outside the linear elastic region will not provide information about true tissue material properties. YM values for large strains will tend to be positively biased and largely stress dependent. Previous studies have shown that large strains may be required in order to achieve a reasonable strain SNR [32]. In addition, clinical application of elasticity imaging and palpation will likely involve high strains. It should be understood that high strain elasticity measurements will provide information only about tissue pseudo-elastic properties (elasticity of tissue at a specific stress or strain level).

6.8 Effect of Sample Dimensions and Sample Thickness

A careful study of the effect of sample dimensions on sample stress-strain curves is important in understanding how tissue elasticity measurements can be affected by tissue sample dimensions as well as tissue material properties.

Figure 6.11 shows the stress-strain response of the three PVC gel standoff samples measured using the Instron and ultrasound techniques.

All three curves exhibited an exponential stress-strain relationship characteristic of many soft tissues. All samples were made of the same PVC standoff material, with square

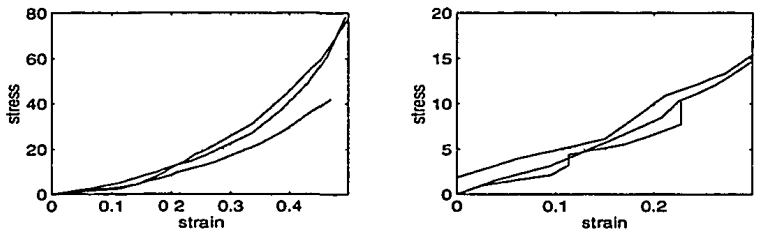

(a) (b)

Figure 6.11: Effect of sample dimensions.

2.0 cm × 2.0 cm identical surface dimensions. To study the effect of sample thickness (height) on stress-strain responses, standoff A was cut with a thickness of 2.5 cm while standoff B2 had a thickness of approximately 3.5 cm. To study the effect of sample surface dimensions, a third sample, standoff B, was cut with 2.0 cm × 3.5 cm surface dimensions and with a thickness of 2.0 cm. The surface dimensions of all samples allowed the samples to fit completely under the Instron aluminum punch crosshead which had a 5.7 cm diameter. This enabled a uniform stress to be applied and reduced the possibility of stress non-uniformities at sample edges. Instron punch and sample surfaces were lightly lubricated to prevent bonding between the sample and punch.

The stress-strain response of all samples was very similar for low strains (1%-10%) for both Instron and ultrasound curves. This supports the hypothesis that stress-strain response should be independent of sample thickness and sample surface dimensions for the case of uniform compressions, since the strain parameter normalizes sample deformation with respect to the initial thickness of the sample as observed in Equation. (6.1). In uniaxial compression tests of gelatin gels, similar results were observed [79].

6.9 Concluding Remarks

Changes in tissue elasticity are often correlated to the onset of pathology or disease. The capability to image differences in tissue elasticity provides extremely useful clinical information that is currently not attainable by other imaging modalities. Ultrasound provides a potentially potent method for non-invasive and relatively inexpensive mea-

surement of tissue elastic properties. It is important to consider the effects of sample dimensions, strain level, and preconditioning in order to obtain unbiased measurements of true tissue material properties.

CHAPTER 7

EXAMPLES OF ELASTICITY IMAGING

In this chapter, several examples of strain and elasticity images are provided from ultrasound data from tissue phantoms, Achilles' tendon and breast tumors from human breast cancer patients.

7.1 Background

Changes in tissue pathology are often strongly correlated to the onset of tissue pathology or disease. Tissue elasticity imaging has direct relevance in the early detection of breast and prostate cancers and liver cirrhosis, diseases which are believed to significantly alter tissue elasticity. Some cancers, such as scirrhus carcinoma of the breast, for example, appear as stone hard nodules, while many benign fluid-filled cysts can be softer than the surrounding tissue. Atheroschlerosis and other vascular diseases are characterized by the accumulation of plaque in the arteries. Plaque buildup can lead to dramatic changes in the elastic properties of arterial walls, and development of elasticity imaging techniques on a microscopic scale could allow for monitoring and early detection of vascular diseases.

Elasticity imaging consists of three basic steps: 1) measurement of tissue motion, 2) computation of internal strains, and 3) reconstruction of elasticity distributions. An elasticity image is generated by acquiring high-frequency ultrasound images of tissue before and after the tissue has been subjected to a small compression (in clinical practice the deformation may be delivered by an ultrasound probe device similar to angioplasty). By tracking speckle motion (step 1), and the relative change in area or volume of different regions of tissue (step 2), information about tissue mechanical properties can be obtained (step 3). Other potential applications include early detection of cardiac dysfunction by monitoring changes in cardiac contractility [80], monitoring of therapeutic processes

which can alter tissue elasticity such as cryotherapy [81], coronary artery diagnosis [82], and early detection of carcinomas of the breast, testes, thyroid and prostate [2, 3, 10].

7.2 Wire Phantom Test

The purpose of this experiment was to measure the displacement field in a homogeneous gel phantom, as the phantom was compressed by a small circular compressor under controlled test conditions. The experimental results are then compared to theoretical predictions. This scenario has direct relevance to ultrasound tissue displacement imaging of breast tumors (Chapter 5), where compressions may be made by a small rectangular or circular transducer.

7.2.1 Methods

A cylindrical tissue mimicking phantom was made using PVC, shor value #4 (previously described, Chapter 6).

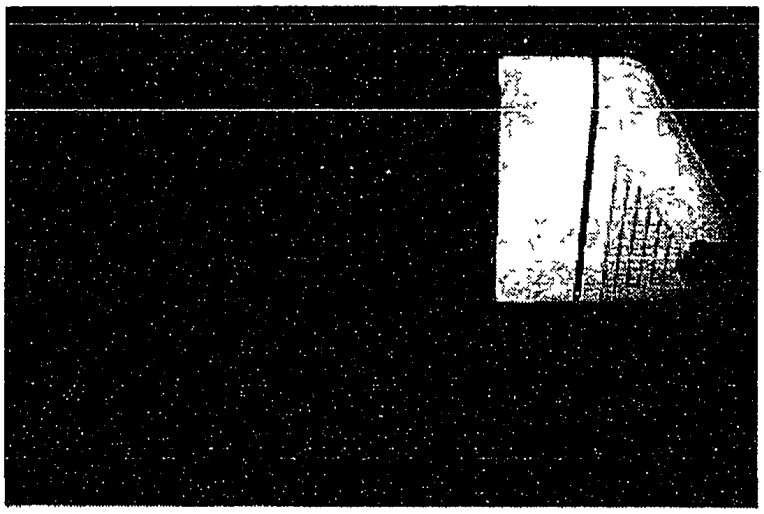

Figure 7.1: Wire phantom.

The phantom was 8.8 cm in height and had a 10.1 cm diameter. Twelve kevlar thread 0.008 inch diameter wires were set in the phantom in three columns with four wires per

column. The vertical spacing between wires was 0.5 cm for the two outer columns and 1.0 cm for the center column (Fig. 7.1).

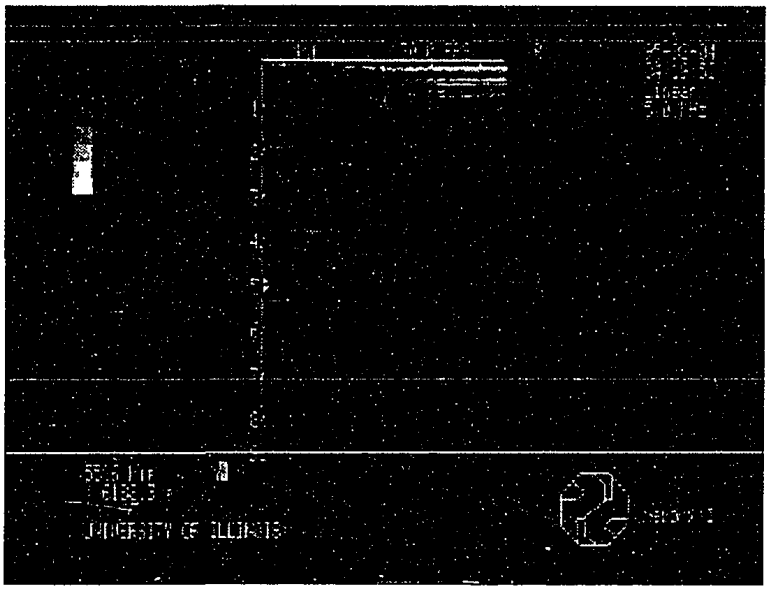

Figure 7.2: Ultrasound image of wire phantom.

Ultrasound images were acquired using a 5.0 MHz, Pie Medical 480 Linear Array Transducer (Fig. 7.2). The array was used to obtain sagittal scans of the phantom as the phantom was compressed by the 5.7 cm diameter aluminum punch of an Instron load cell (Fig. 7.3).

The phantom was compressed to a maximum strain of 10% of its original height. Digitized ultrasound images were acquired before and after compression using a TARGA frame grabber system. Ultrasound images covered a total field depth of approximately 9.0 cm, with focal depth set to 5.0 cm, the approximate position of the center column of wire targets.

Images were ported to a SUN Sparc20 workstation for processing using the previously described correlation tracking programs (Chapter 2).

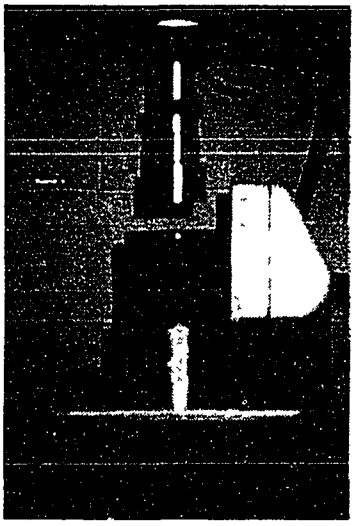

Figure 7.3: Geometry of test measurements.

7.2.2 Results

Results for this experiment are shown in four figures. Figure 7.4 shows the displacement field of the wire phantom computed using a one-dimensional correlation search. The displacement field covers a field of view 7.5 cm x 7.5 cm centered on the center column of wire targets and shows the vertical component of displacement.

For a homogeneous phantom (uniform elasticity) undergoing uniform compression, the magnitude of displacement should decrease linearly with depth. For uniform compression, the following boundary condition should be satisfied:

$$surface\ area\ of\ compressor\ >\ surface\ area\ of\ phantom \tag{7.1}$$

For the homogeneous wire phantom undergoing compression from a small circular compressor, the magnitude of displacement should decrease approximately exponentially according to the equation

$$\sigma(z) = \sigma(0) * \frac{1}{(1+\frac{a^2}{z^2})^{1.5} - 1} \tag{7.2}$$

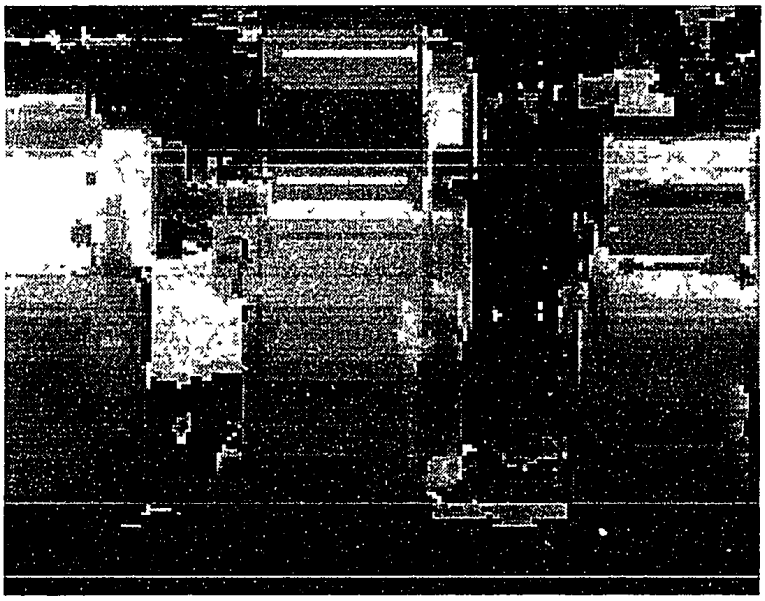

Figure 7.4: Displacement field for wire phantom.

where a represents the radius of the compressor and z represents the depth from the surface of the phantom. The derivation for this equation can be found in the mechanics literature [83] along with equations for rectangular and other compressor shapes. A brief derivation of Equation (7.2) is given in [84], which follows closely the derivation of [83].

In Fig. 7.4, displacement in the phantom decreases with depth from the surface as expected. There are noticeable artifacts along two columns at horizontal positions of 40 and 100 in the image. These artifacts correspond to spatial positions in the phantom where no wire targets were present. Figure 7.4 was computed using a 150 $\times$ 150 grid of points with a 0.25 mm spacing between grid points, a 7.5 mm $\times$ 7.5 mm kernel size and a 1.0 cm search region.

Figure 7.5 provides a comparison between the experimental and theoretical displacements versus depth (following Equation (7.2)) in the wire phantom, along the center column of wire targets. The straight line represents theoretical displacement for uniform compression and the curved line is the theoretical curve for the circular compressor used in this study. The experimental data are relatively noisy (SNR=2.7). The signal to noise ratio (SNR) was computed by taking the mean signal level, divided by the standard

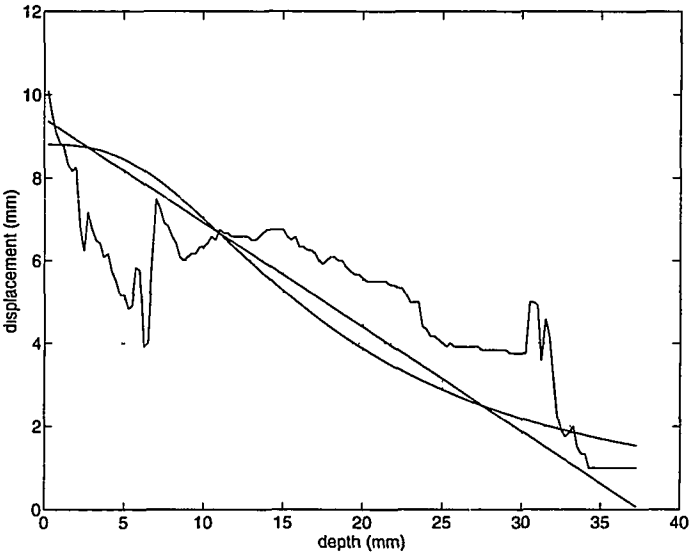

Figure 7.5: Comparison.

deviation following the convention of [3]. Possible sources of error include slippage between the compressing punch and the phantom, curvature of the phantom surface, which was assumed to be completely flat and the fact that a relatively high strain (10%) was used. The wire phantom was observed to have a 1.0 cm dip at the surface, which was due to cooling effects during the synthesis of the phantom. This may also explain why the experimental displacements are lower than expected near the surface of the phantom (0-6 mm).

Figure 7.6 shows a side-by-side comparison of the displacement field in the wire phantom and the maximum correlation coefficient found in computing the displacement at each point in the phantom. These results clearly show the low correlation values at horizontal positions of 40 and 100 where no wire targets were present. Correlation values were between 0.05-0.15 in these regions and between 0.90-0.99 in areas with wire targets. The low correlation values indicate unreliable displacement tracking in these regions and confirm the presence of artifacts in these regions in the displacement image.

Figure 7.7 shows the two-dimensional displacement vector field in the wire phantom computed using a more computationally intensive 2-D correlation search. The field indi-

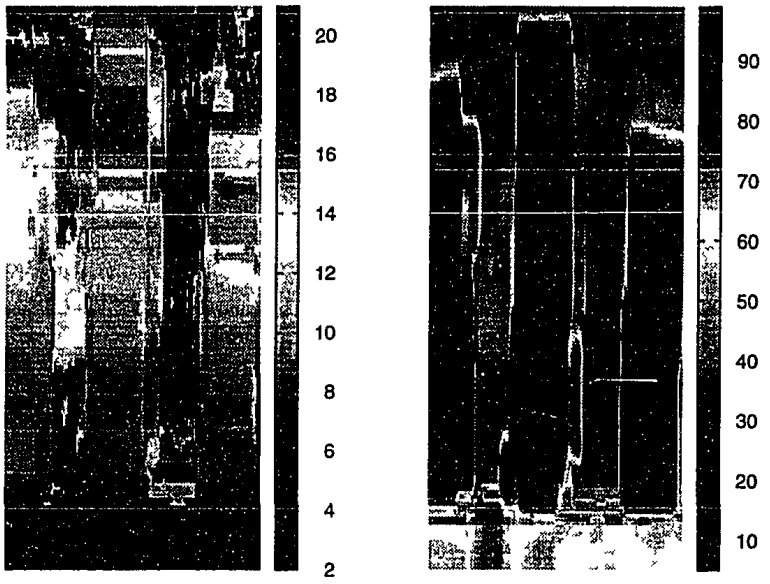

Figure 7.6: Wire phantom displacement field and correlation map.

cates some lateral slippage or movement of the phantom on the right side of the phantom which would occur if the centers of the wire phantom and compressing punch were not perfectly aligned. The vector field consisted of a 30 × 30 grid of points with a 1.25 mm spacing between grid points, a 7.5 mm × 7.5 mm kernel size and a 1.0 cm × 0.5 cm search region. A smaller number of grid points and larger grid spacing were used due to the increase in computation time required for a 2-D correlation search. The computation time for the 2-D correlation search was approximately 20 times longer than for the 1-D search (approximately 4 hr for the 1-D search on a Sparc2 and 80 hr for the 2-D search). The successful implementation of a digital hardware correlator for high speed tracking has been investigated in previous works [38].

7.3 Achilles' Tendon

The purpose of this experiment was to produce an in vivo strain image of the Achilles' tendon before and after compression and passive stretching. Data are collected from two scan orientations (sagittal and transverse), and the strain images of the Achilles' tendon are compared with conventional ultrasound images.

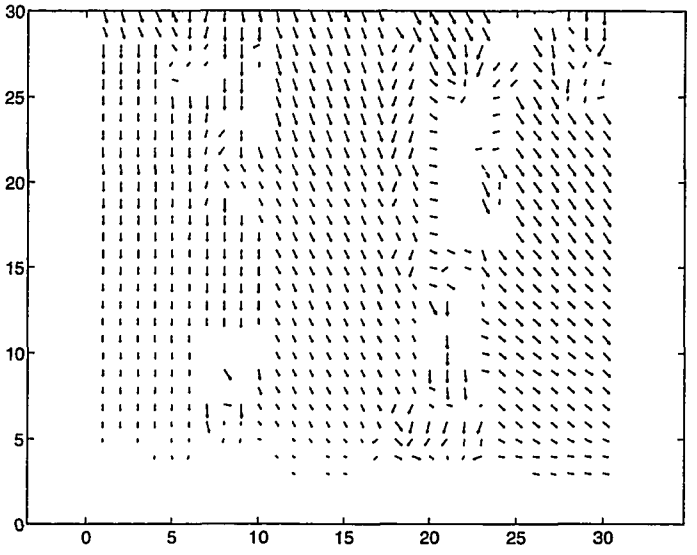

Figure 7.7: Wire phantom 2-D displacement field.

Figure 7.8 shows a textbook drawing of muscle tendon and bone. The tendon is a tough cord or band of dense white fibrous connective tissue that unites a muscle with other structures such as the bone.

Figure 7.9 shows the location of the human Achilles' tendon and tibular bone and is also used to describe the orientation of the scans. For transverse scans, the ultrasound imaging plane is perpendicular to the ankle. For sagittal scans, the imaging plane is parallel to the ankle. Figures 7.8 and 7.9 are adapted from [54] and [85], respectively.

7.3.1 Methods

Sagittal and transverse ultrasound scans of the Achilles' tendon were acquired from a patient volunteer at the Department of Radiology, University of Michigan Hospital, using a 5.0 MHz ultrasound scanner (Siemens Quantum QAD1). Images were binary format envelope detected data, 201 X 433 pixels with a 0.266 mm X 0.266 mm pixel size.

For the transverse configuration, images were acquired before and after compressions were applied by the QAD transducer. Data were acquired with the tissue going from the compressed to uncompressed state. For the sagittal configuration, images were acquired

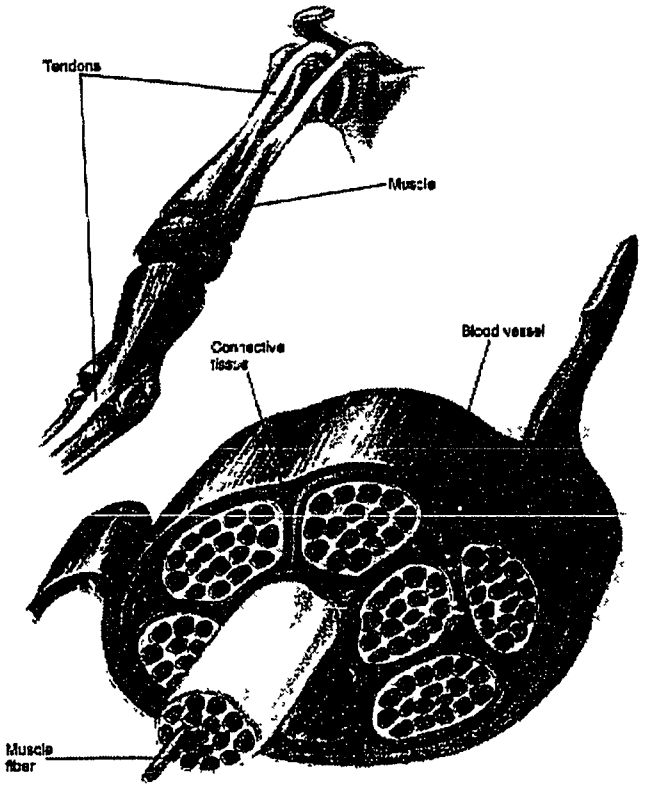

Figure 7.8: Textbook drawing of muscle and tendon (Varder 1988).

with the patient's tendon in the rest state and in a stretched state. The tendon was stretched by having the patient stand and extend their ankle and heel.

7.3.2 Results

The results of this experiment consist of conventional ultrasound images and strain images of the Achilles' tendon of a volunteer patient. Both sets of images show two views of the Achilles' tendon, a sagittal view where the Achilles' tendon is in the imaging plane, and a transverse view with the Achilles' tendon perpendicular to the imaging plane (Fig. 7.10). The transverse scan is used to illustrate some of the limits of the elasticity imaging method in its present state.

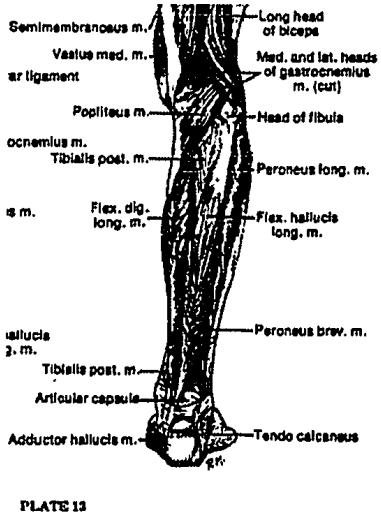

Figure 7.9: Textbook drawing of Achilles' tendon (Stedman 1990).

Figure 7.10(a) is a transverse ultrasound scan of the Achilles' tendon while Fig. 7.10(b) is a corresponding strain image of the same view. The strain image covers a total field of view of 5.0 cm × 10.0 cm. The total dynamic range of the strain image is from 0 to 38.7% strain. The strain image was produced in two steps:

1. First the displacement field for the Achilles' images was computed using a one-dimensional correlation search.

2. Second, the strain field was computed by taking the derivative of the displacement field. The derivatives were approximated by taking finite differences of the displacement field.

In Fig. 7.10(a) there is a thin layer of fat below the skin surface, visible near the top of the image. The bright circular shaped echo midway down and on the left side of the image corresponds to the tibular bone. The Achilles' tendon is weakly visible on the left side of the ultrasound as a circular echo below the skin surface and above the bone echo. In Fig. 7.10(b) the tibular bone is visible as a dark area showing little to no strain. However, the tendon area is not visible on the strain image. This shows some of the sensitivity and limits in strain imaging. The technique is able to detect differences

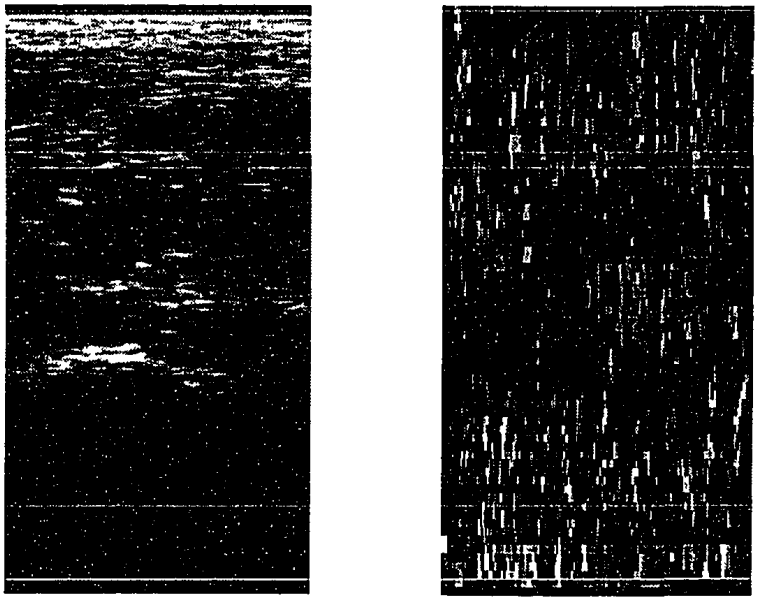

Figure 7.10: Transverse ultrasound and strain images of Achilles' tendon.

between muscle and bone; however, it is not currently sensitive enough to separate muscle and tendon.

Figure 7.11 shows a sagittal ultrasound scan of the Achilles' tendon and a corresponding strain image of the same view. There is a layer of fat below the skin surface, visible near the top of the ultrasound image. The Achilles' tendon in its stretched state is visible on the ultrasound as a horizontal strip below the skin surface and above the bone echo. The tibular bone appears as a slanted horizontal reflector appearing midway down the image. Both the Achilles' tendon and tibular bone are shown on the strain image as dark bands corresponding to low strain regions. The strain image confirms the hypothesis that the tendon has a higher elasticity or stiffness in its stretched state relative to its rest state. These data provide some good examples of the sensitivity and limits of strain imaging.

The high resolution strain image consists of a 69 $\times$ 199 grid of points with a 1.25 mm spacing between grid points, a 0.25 mm $\times$ 12.5 mm 1-D kernel and a 12.5 mm search region.

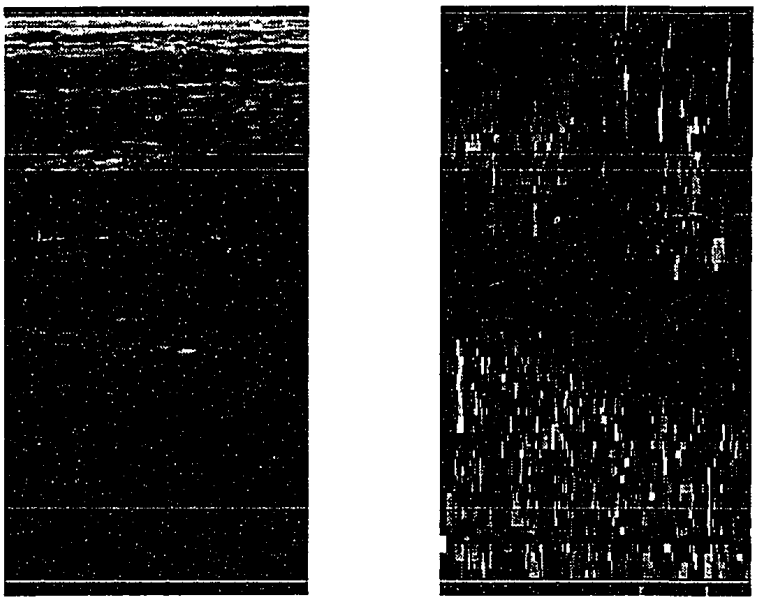

Figure 7.11: Sagittal ultrasound and strain images of Achilles' tendon.

7.4 Tumor Compression Image

The goal of this experiment was to produce an in vivo strain image of a soft tissue breast tumor. Ultrasound images of the tumor are collected before and after a compression is applied. The strain image is compared with the pre-compression ultrasound image.

7.4.1 Method

Digitized ultrasound images of a breast mass before and after compression were applied and acquired using a 7.5 MHz linear array transducer (Acoustic Imaging, Phoenix, Arizona) from a volunteer patient. The transducer was used to perform the compressions with the patient supine and the breast stationary. These data were obtained from the department of radiology at the University of Michigan hospital following the protocols described in Chapter 5.

7.4.2 Results

The results of this experiment consist of conventional ultrasound B-scan images and displacement images of the breast mass.

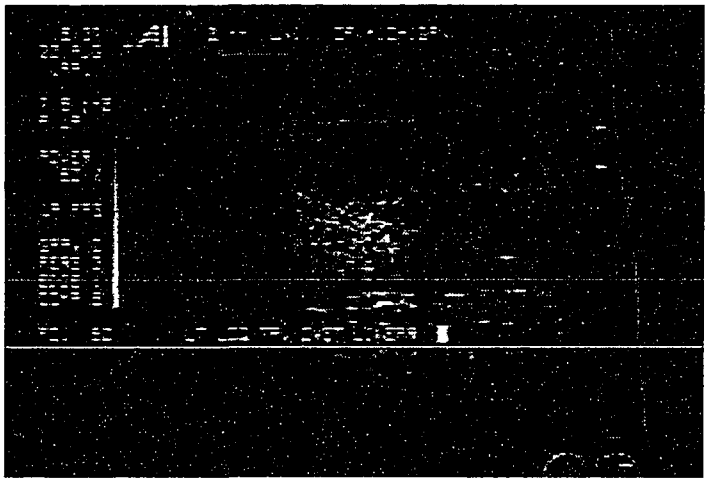

Figure 7.12: Ultrasound image of breast tumor.

Figure 7.12 shows a standard ultrasound B-scan image of the mass. The mass has dimensions of approximately 2.75 cm × 1.75 cm based on the ultrasound image.

Figure 7.13 shows a displacement image of the same mass. The displacement image covers a total field of view of 6.25 cm × 3.75 cm. Displacements values in Fig. 7.13 span a dynamic range from 0.0 mm to 5.0 mm. The displacement image consists of a 25 × 15 grid of points with a 2.5 mm spacing between grid points, a 1.25 cm × 1.8 cm kernel size and a 5.0 mm search region. The mass location extends from depth positions 8 to 9 and lateral positions 10-12 in Fig. 7.14 based on its position in the ultrasound image.

Figure 7.14 is a plot of the axial displacement along the center of the displacement image. The mass location would ideally be located at a depth of 8 in Fig. 7.14 based on its position in the ultrasound image. Figure 7.14 can be divided into three regions: depths 3-8, 8-11 and 11-14. The strain in regions I & III (depths 3-8 and 11-14) can be estimated by taking the derivative of the displacement and are seen by their slopes in Fig. 7.14 to be non-zero. The strain in regions II (depth 8-11) is apparently zero

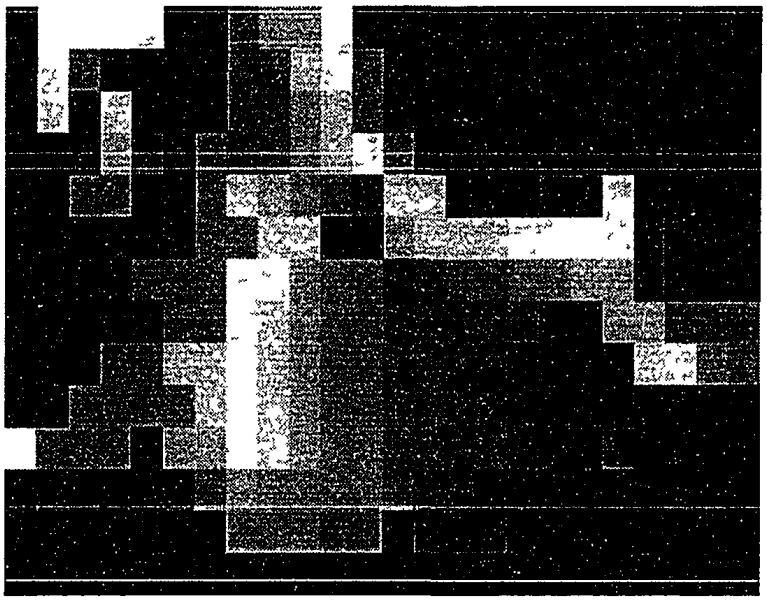

Figure 7.13: Displacement image of breast tumor.

which would be consistent with an incompressible cyst with high stiffness relative to the surrounding breast tissue.

Table 7.1 shows the axial strain computed from slopes the displacement for the different regions in Fig. 7.14. The strain was calculated in two steps:

1. First the displacement field (Fig. 7.14) was computed using a one-dimensional correlation search.

2. Second, the strain field was computed by taking the derivative of the displacement field. The derivatives were approximated by taking finite differences of the displacement field.

A simple linear interpolation was used to compute the best fit slopes in each of the three regions.

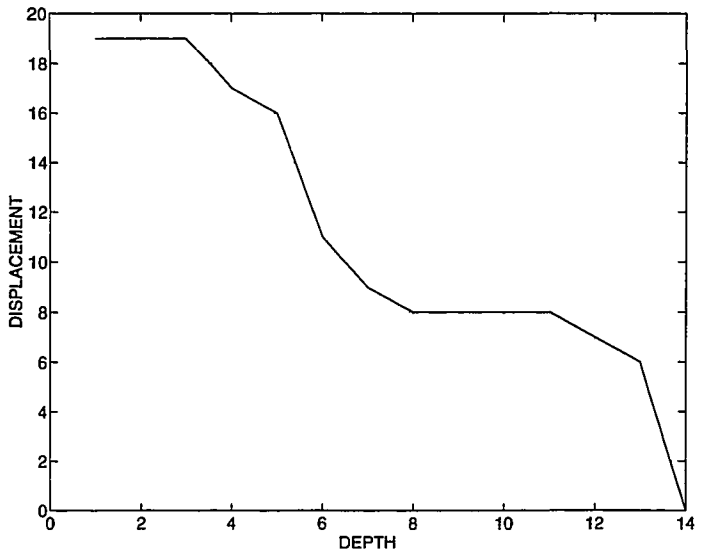

Figure 7.14: Axial displacement plot of breast tumor.

Table 7.1: Axial strain at three depths

Region #	Relative strain
1	2.2
2	0.0
3	2.7

7.5 Inclusion Phantom

The purpose of this experiment was to produce an elasticity image of a homogeneous gel phantom containing a hard circular inclusion, as the phantom was compressed by a large rectangular compressor under controlled test conditions. This scenario has direct relevance to ultrasound tissue displacement and tissue elasticity imaging of hard breast masses or tumors (Chapter 5), where compressions may be made by a small rectangular or circular transducer.

7.5.1 Methods

A homogeneous cylindrical gel phantom, 90.0 mm in diameter and 140.0 mm in length, was made from 5.5% by weight gelatin (Knox Gelatine, Inc., Engelwood Cliffs, NJ). Polystyrene microspheres, 0.4% by weight (Analytical Grade Cation Exchange Resin, AG 50 W-X12, Bio-RAD Laboratories, Hercules, CA) with diameters of 40-120 μm were added to produce ultrasound scattering [3]. A 30.0 mm diameter cylindrical core (a circular longitudinal hole) was hollowed out of the phantom and filled with 12% by weight gelatin to simulate the presence of a hard cylindrical inclusion. The inclusion had a Young's modulus (stiffness) of approximately 2.5 times that of the surrounding material. The value of the Young's modulus was estimated from the approximately linear dependence of the Young's modulus on gel concentration [3, 74]

The phantom was uniformly compressed to a maximum strain of approximately 8.9%. The phantom construction and data acquisition were performed at the University of Michigan. Data were collected for two types of motion: 1) translations and 2) compressions. This section describes the results of the compression data.

The ultrasound tissue equivalent phantom was placed in a holder to secure it from motion and attached to the bottom of a water-filled tank. The phantom was a water-based gel with a preservative added and small particles for linear attenuation and low background scatter (speed of sound = 1540 m/sec). It was originally produced as the background material for a contrast detail phantom from ATS Labortories (Bridgeport, CT, (203) 579-2700). A 7.5 MHz scanhead of a Quantum QAD1 ultrasound scanner (Siemens Quantum, Inc., Seattle, WA) was attached to a positioning system (Precision Data Systems, Englewood, CO) on the tank, which translated the scanhead vertically away from the phantom in individual steps of 0.145 mm. The phantom was then placed in a compression device constructed of two rectangular acrylic plates. A 25 x 110 mm rectangular section was cut out of the top plate for an acoustic window (0.03 mm thick plastic sheet wrap) through which ultrasound images could be made. The phantom was partially compressed prior to the elasticity experiment to prevent any slip during com-

pression. Any vibration in the system was allowed sufficient time to damp out between each step. The entire translation process was recorded continuously on digital tape while the position at each step was verbally indicated on the audio channel of the tape. The tape was then played back and individual frames were selected for transfer of the envelope detected data from the tape to an IBM-compatible 386 computer via a vendor-supplied digital memory dump. These data were then transferred to the University of Illinois for analysis.

7.5.2 Results

The results of this experiment consist of conventional ultrasound B-scan images and elasticity images of the inclusion phantom. Figure 7.15 shows a standard ultrasound B-scan image of the inclusion phantom.

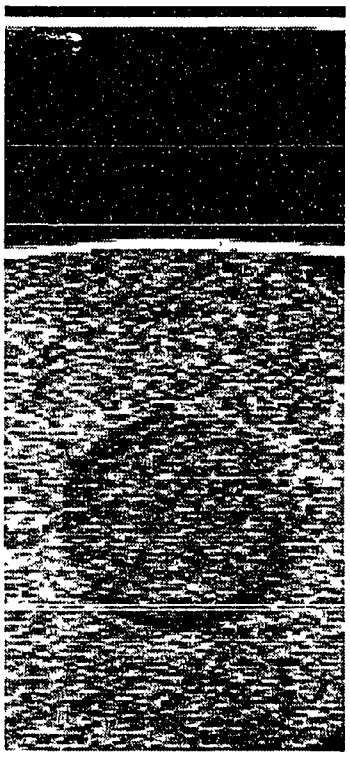

Figure 7.15: Ultrasound B-scan image of inclusion phantom.

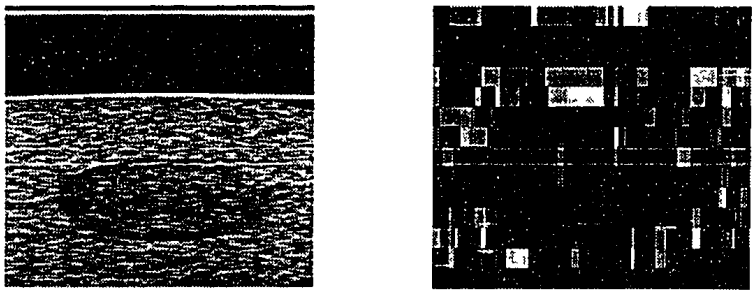

(a) (b)

Figure 7.16: Low resolution strain image of inclusion phantom.

Note the presence of fully developed speckle as found in tissue, which was produced by the addition of fine particles and scatterers to the phantom during construction (Fig. 7.15). The particles produce the speckle texture in the B-scan of the inclusion phantom similar to that found in tissue and were used to simulate tissue conditions for imaging the inclusion. The presence of the inclusion is difficult to see on the B-scan, and the contrast between the inclusion and surroundings is poor. Figure 7.16 is a low resolution elasticity image of the inclusion phantom.

Figure 7.17 is a high resolution elasticity image of the same inclusion phantom. The elasticity image covers a total field of view of 50.0 mm $\times$ 93.75 mm. The elasticity image indicates the presence of a hard 31.25 mm diameter circular inclusion at a depth of 25.0 mm. The contrast to noise ratio defined as the difference between the strain inside of the inclusion and the strain outside of the inclusion normalized to the standard deviation of the strain was approximately 13.

The elasticity image was produced in four steps:

1. First the displacement field for the inclusion phantom was computed using a one-dimensional correlation search.

2. Second, the strain field was computed by taking the derivative of the displacement field. The derivatives were approximated by taking finite differences of the displacement field.

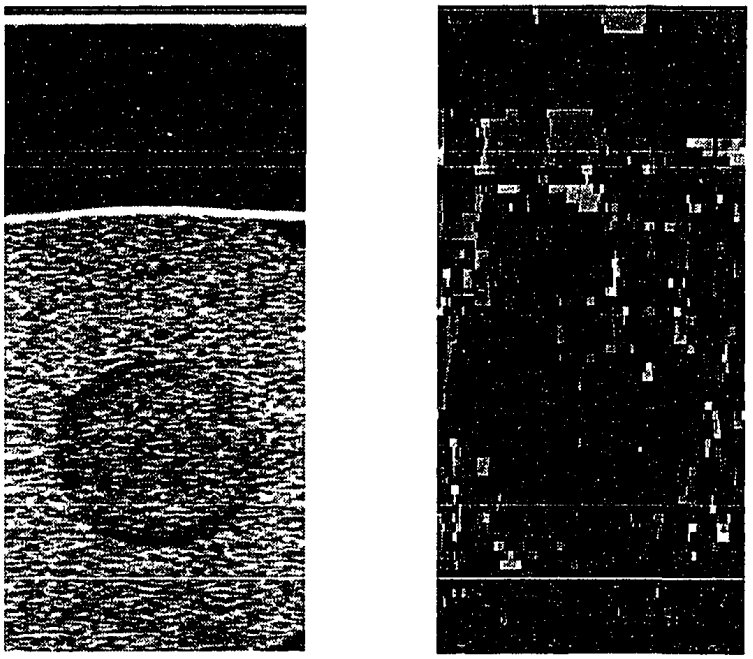

(a) (b)

Figure 7.17: High resolution strain image of inclusion phantom.

3. Third, the stress field was measured experimentally. For this experiment a uniform compression was applied and the stress field was assumed to be constant.

4. Finally, the elasticity image was computed by dividing the stress image by the strain image.

Figure 7.18 shows the strain along the central axis of the inclusion phantom. There is clearly a reduced strain in the region of the inclusion, which extends from a depth of 31 to 56.

Figure 7.19 shows a side-by-side comparison of a low resolution elasticity image and the maximum correlation coefficient found in computing the strain at each point in the phantom. The results indicate good reliabilty in tracking tissue motion.

The high resolution elasticity image consists of a 69 $\times$ 199 grid of points with a 1.25 mm spacing between grid points, a 5.0 mm $\times$ 12.5 mm kernel size and a 12.5 mm search region. The low resolution elasticity image consists of a 14 $\times$ 199 grid of points

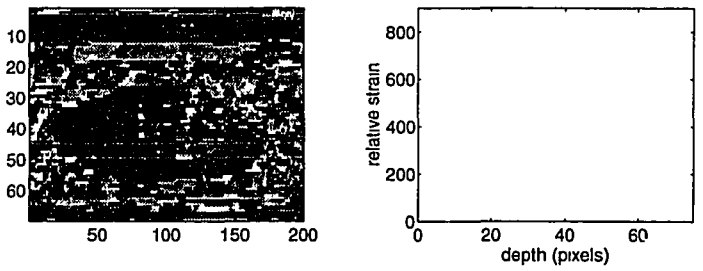

(a) (b)

Figure 7.18: Plot of strain along central axis of inclusion phantom.

with a 6.25 mm spacing between grid points, a 5.0 mm × 12.5 mm kernel size and a 12.5 mm search region. The computation time was approximately 20 hr on a Sparc2 for the low resolution image and approximately 100 hr for the high resolution image.

Figure 7.20 shows the effects of speckle decorrelation versus compression for a homogeneous cylindrical phantom (no inclusion) undergoing uniform compression. The phantom had a 90.0 mm diameter and was compressed to a maximum strain of approximately 10% its original height. Axial displacements were computed from envelope detected data of the phantom being compressed using one-dimensional windows 100 data points (25.0 mm) in size. The solid line represents the average correlation coefficients versus compression (speckle decorrelation) where each data point is the average of 32 measurements. The dashed line shows one of the trials and is a representative sample path. The dotted lines are two standard deviations from the mean and represent the 95% confidence intervals.

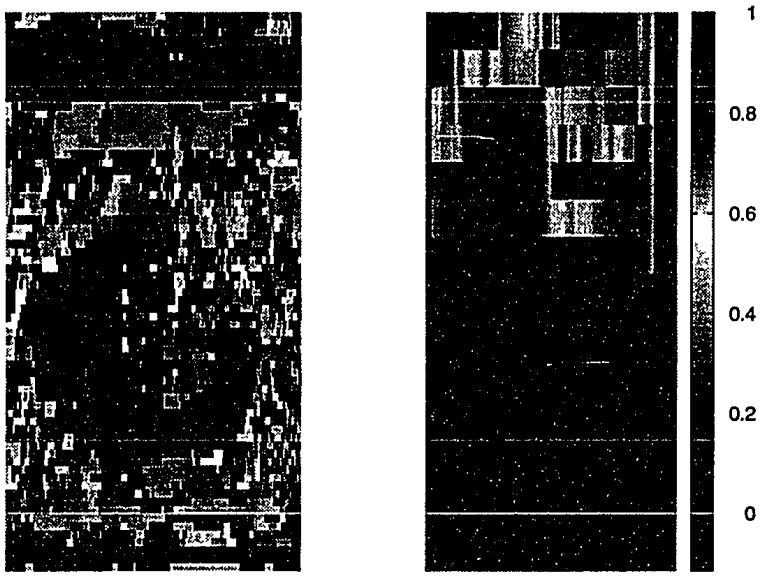

(a) (b)

Figure 7.19: Strain and correlation images of inclusion phantom.

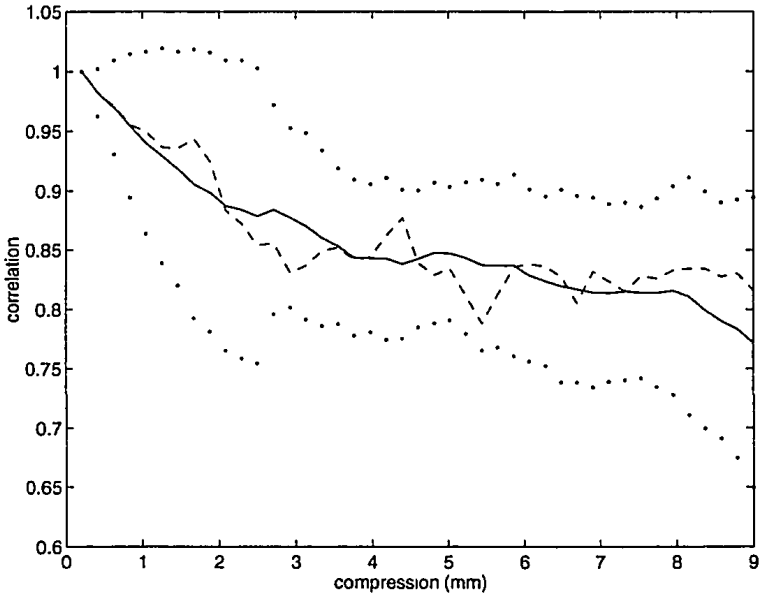

Figure 7.20: Speckle decorrelation vs. compression.

CHAPTER 8

ACCURACY, LIMITS AND TRADEOFFS IN DISPLACEMENT AND ELASTICITY IMAGING

Ultrasound elasticity measurements rely on accurate and precise displacement measurements. The accuracy of displacement data directly influences the accuracy of reconstructed elasticity fields, since elasticity data are usually constructed by processing displacement data. The accuracy of displacement measurements depends on many factors such as deformation size and type, window/kernel sizes and transducer frequency. Selection of specific values can result in tradeoffs between displacement accuracy parameters and fundamental elasticity imaging parameters such as strain resolution and strain SNR. In this chapter, we discuss some of the important parameters and relationships between accuracy, limits and tradeoffs in ultrasound displacement and elasticity measurements.

8.1 Background

In many medical and nonmedical ultrasound imaging applications, data are computed from estimates of tissue displacement. An often overlooked aspect of the process is the importance for the user to understand to what degree the data are reliable. Evaluations are only as good as the data on which they are based. Information derived from tissue displacement measurements can be used to assess tissue elastic properties which have tremendous potential applications. In food science, objective measurements of food mechanical properties are of interest in maintaining proper food quality control and in assessing the viability of new foodstuffs. Medical applications include the early detection of breast and prostate cancers and liver cirrhosis, diseases which are believed to significantly alter tissue elastic properties. The potential of imaging tissue elastic properties is enormous considering the prospective size of consumer and patient populations, the importance placed on quality and cost-effective health care, and the enormous size of food industry and health-care markets.

Therefore, the need for a full understanding of accuracy issues and limitations on tissue displacement measurements has implications for many potential applications.

The accuracy of ultrasound displacement measurements depends on many factors including deformation size and type, window size, transducer frequency and tissue type. In elasticity imaging, the accuracy of displacement measurements also affects the accuracy of reconstructed elasticity fields since they are directly computed from displacement data.

The highest accuracy that can be achieved in displacement measurements using conventional speckle tracking is limited by the Cramer Rao bound [86]. In addition, the digital sampling frequency limits the time resolution in a backscattered ultrasound echo and ultimately the smallest detectable displacement. The sampling frequency and tissue element size also limit the smallest detectable strain in elasticity imaging.

Selection of deformation size, window/kernel sizes, transducer frequency/bandwidth and sampling frequency in displacement measurements can result in tradeoffs between displacement accuracy and fundamental elasticity imaging parameters such as strain resolution, strain dynamic range and strain SNR. In this chapter, we first discuss the influence of several important imaging parameters on the accuracy of displacement measurements. Next, the effects of window sizes, digital sampling frequency and strain level on limiting displacement accuracy, strain resolution and strain SNR are discussed. Finally, several possible tradeoffs in ultrasound elasticity measurements are discussed and related to accuracy issues.

8.2 Accuracy

The impact of six important imaging parameters on the accuracy of two-dimensional tissue speckle tracking have been investigated in depth by Ramamurthy et al. and Chen et al. [42, 43]. These parameters include

- magnitude of tissue motion
- direction (axial or lateral) of tissue motion
- dimensions of tissue region being tracked

- ultrasonic frequency of interrogation
- digital sampling frequency
- signal type (ultrasonic RF or envelope detected)

8.3 Limits

Conventional displacement measurements using speckle tracking usually consist of applying cross correlation or other window matching methods to compute displacements (Fourier methods have also been reported). The precision of cross correlation time shift estimation can be characterized by the mean square error of the time shift estimate. The precision of displacement estimates is generally inversely proportional to the ultrasound signal bandwidth (B), the window size (T) and the signal to noise ratio of the echo signal (SNR) [87]. Ultimate limits on the accuracy of displacement measurements have been investigated using the Cramer Rao Lower Bound (CRLB) [88] under a variety of conditions.

The digital sampling frequency ultimately limits the time resolution of ultrasound echo data. Parilla et al. report that sampling at or above the Nyquist rate can make SNR the limiting factor [89]. The accuracy of displacement measurements can also be limited by low bit quantization [34]. In tissue elasticity measurements, a very high time resolution may be required to achieve reasonable strain estimates [90]. Sample interpolation methods have been applied to obtain time shifts less than the sample period. The interpolation method (parabolic, sinc, quadratic, cubic) can contribute to time shift errors [48].

In elasticity measurements, determination of the appropriate strain level is crucial. O'Donnell et al. report that high strain levels may be required in order to achieve sufficient strain SNR [3]. However, the strain level directly affects the degree of signal distortion between pre-compression and post-compression signals. Elasticity measurements based on correlation methods are accurate only to the extent that segments of the pre- and post-compression signals can be considered as linear translations of one an-

other. As previously discussed, high strains can result in significant signal decorrelation and limit the accuracy of displacement measurements [90].

8.4 Tradeoffs

8.4.1 Time shift estimation error vs. window/kernel size

Ramamurthy et al. have shown that time shift errors typically increase with smaller window sizes using correlation techniques [42, 43] (See also Chapter 3).

8.4.2 Time shift estimation error vs. bandwidth vs. SNR

Foster et al. have reported that time shift errors should decrease with increasing SNR and transducer bandwidth [40]. Cespedes and Ophir have also investigated the effect of bandwidth and SNR on displacement measurements for elastography [90].

8.4.3 Strain resolution vs. window/kernel size

Ophir et al. have noted a classic tradeoff between window size and resolution in elastography measurements [4]. Larger window sizes can improve displacement accuracy but there is a resulting loss in spatial resolution [2, 32].

8.4.4 Strain dynamic range vs. minimum detectable time shift

In elastography type measurements, the strain dynamic range is directly dependent on the minimum time shift estimate. The strain range will typically be in increments of $\frac{C}{2} * \frac{t_m in}{L}$, where $t_m in$ and L represent the minimum time shift and pre-compression length of a tissue element and C is the tissue speed of sound.

8.4.5 Multiple incremental compressions vs. single large compression

Since large strains can improve strain SNR, the use of multiple incremental compressions to achieve a large net strain have been employed in elasticity measurements

of gels-based tissue phantoms and muscle tissue [32, 91]. Multiple incremental compressions attempt to avoid problems with signal distortions and decorrelation that can result from a single large compression. We have previously reported that displacement measurements made over small deformations (translations) and large number of increments showed significant improvement in accuracy vs. those for single large deformation [42].

8.4.6 Depth dependent stress vs. compressor size

Cespedes and Ophir have reported stress field non-uniformities which are strongly dependent on compressor radius [84]. Stress non-uniformities can be largely eliminated in sample measurements if the compressor size is larger than the sample surface dimensions [4, 91]. However, the depth dependent stress problem is complicated since accurate one-dimensional elasticity measurements may require a minimum height-width aspect ratio in order to meet the requirement of a bar sample for true one-dimensional mechanics measurements. In addition, the stress field estimations from simple (circular) compressors [84] assume a homogeneous medium. At present, there are also no convenient methods for measuring internal stresses, although [4] have introduced the concept of the stress meter, where the stress in a layer of tissue of known elastic modulus is computed and used to reconstruct internal stress fields. However, the accuracy of this method still needs to be tested.

8.4.7 Linear vs. non-linear elastic behavior

Current static and quasi-static elasticity measurements have been largely based on the assumption of linear elastic behavior of tissues. In much of the present work, deformations have been limited to low strains in order to maintain linear behavior. As previously discussed, high strains may be required to obtain a reasonable SNR. Using two independent elasticity measures, Chen et al. [91] have observed a strain hardening effect in soft tissue, with non-linear behavior and permanent plastic deformation of tissue at high strains. It should be understood that for high strains, elasticity measurements are representative of only tissue pseudo-elastic properties (elasticity at a specific strain

level) and not true tissue material properties. Current elasticity measurements can also be limited by problems due to stress relaxation, creep and hysteresis effects in repeated compression measurements [78, 91].

CHAPTER 9

CONCLUSIONS

This thesis has investigated topics in the areas of ultrasound displacement and elasticity imaging. The key contributions in these areas are summarized below.

9.1 Contributions

The major contributions of this thesis can be divided into four primary components: 1) an accuracy assessment of ultrasound displacement imaging, 2) an accuracy assessment of ultrasound elasticity measurements, 3) application of displacement imaging to breast cancer detection and 4) application of strain and elasticity imaging to phantom and clinical data.

The accuracy of ultrasound displacement imaging depends on many factors such as ultrasound frequency, magnitude and direction of motion and tissue type. The impact of various imaging parameters on ultrasound displacement and velocity estimates was studied. In addition, the accuracy of ultrasound displacement measurements were investigated in various tissues including liver, muscle and fat. To our knowledge, this represents the first time the effect of different tissue types on displacement accuracy has been investigated in the published literature, and is a key contribution of this work. Some of these results were first presented at the IEEE Ultrasonics Symposium 1991 and 1992 [35, 39] and have since been published [42, 92].

Ultrasound elasticity imaging is a promising new method that may allow the detection of many important tissue diseases such as cancers of the breast and prostate and cirrhosis of the liver, diseases which are believed to significantly alter tissue elasticity. The quantitative accuracy of ultrasound elasticity measurements was investigated and compared with independent and established mechanical load cell measurements. This thesis represents the first reported comparisons between ultrasound elasticity measurements and independent mechanical elasticity measurements. These results were first

presented at the IEEE Ultrasonics Symposium 1994 [91] and have been published [77]. An accuracy assessment of displacement and elasticity imaging is needed to understand both the potential and limitations of this area of research and is, therefore, important. In addition, ultrasound elasticity measurements rely on accurate and precise displacement measurements; therefore, the accuracies of displacement and elasticity imaging are closely linked.

Results in Chapter 5 showed how ultrasound displacement imaging was applied to the problem of breast cancer detection and classification. Displacement imaging was used to test quantitatively the hypothesis that invasion of normal tissues by malignant breast cancer causes connective tissues near the tumor site to become infiltrated, fixing the tumor to the surrounding normal breast parenchyma. This represented the first time in the published literature that motion analysis was used in breast cancer detection. Some of the results in Chapter 7 have been published and will be presented at the IEEE Ultrasonics Symposium 1995 [2, 93].

Results in Chapter 7 showed examples of ultrasound strain and elasticity images of phantoms and clinical data from human patients. Only a handful of elasticity images have been reported in the published literature. Results from the wire phantom data represent one of the first times that internal displacements have been measured in a calibrated phantom and the only time we have seen two-dimensional displacement data displayed. Strain images from the clinical data of the Achilles' tendon and breast cyst have never been produced before, although elasticity imaging of a breast tumor specimen fixed in soft gelatin has been reported.

9.2 Future Work

One of the most significant and most difficult problems that should be investigated in future works is how to measure the stress field produced by small compressor sizes. This problem is important since it more accurately models the clinical situation. Equations for the stress field produced by small compressors in a homogeneous material have been solved analytically in the mechanics literature for simple compressor shapes such as

rectangular and circular [83, 84]. However, this is for the case of homogeneous material (constant elasticity or YM throughout) only. A method to compute the stress field for simple geometries in inhomogeneous materials is needed.

An interesting solution may be the application of iterative or adaptive techniques. For a homogeneous material, the (theoretical) displacement field under a small compressor will be proportional to the stress field based on Hooke's Law. The ultrasound measured displacement field under the compressor (transducer) will differ from the theoretical displacement field and the difference can be called the error. The difference between the theory and the measured data occurs because the measurements are made in inhomogeneous (non-constant YM throughout) material while the theory assumes homogeneous material. Small inhomogeneities (hard or soft areas) can be added and the theoretical displacements recomputed until the theoretical displacement field and measured displacement field match in some sense. The question that remains is how to compute the displacement field given the elasticity distribution and compressor geometry.

Displacement and elasticity imaging involve many tradeoffs between parameters such as window size versus resolution of displacement images versus accuracy. The strain level used is critical in elasticity imaging. Higher strains may be necessary to achieve sufficient strain SNR. However, lower strains are necessary to maintain accuracy in correlation tracking and also for the linear elasticity theory to hold. The determination of optimum strain levels and strategies for accurately tracking displacements under large strains should be investigated. The application of Fourier-based and incremental tracking strategies may be useful for large strains. However, this may result in increased acquisition times because the data are needed over multiple increments. This can result in problems with motion artifacts due to patient motion or breathing during data acquisition.

The issue of tracking rotational motion has largely been avoided in the ultrasound literature. An interesting approach to tracking rotations may involve Fourier domain processing. An alternative to the rotational correlation search algorithm might be to compute the two-dimensional Fourier transforms of the pre- and post-rotated object and

use the phase information to compute the translation component of motion of the object. Once the translation has been computed the correlation rotational search could be used to determine the rotation of the object.

REFERENCES

[1] L. Ryan, G. Lockwood, T. Bloomfield, and F. Foster, "Speckle tracking in high frequency ultrasound images with application to intravascular imaging," in *Proc. IEEE Ultrasonics Symposium*, vol. 2, pp. 889–892, IEEE Ultrasonics, Ferroelectrics, and Frequency Control, 1993. Baltimore, MD.

[2] E. Chen, R. Adler, W. Jenkins, P. Carson, and W. D. O'Brien, Jr., "Ultrasound displacement imaging with application to breast cancer," *Ultrasound, Medicine and Biology*, Aug 1995. in press.

[3] M. O'Donnell, A. Skovoroda, B. Shapo, and S. Emelianov, "Internal displacement and strain imaging using ultrasound speckle tracking," *IEEE Transactions on Ultrasonics, Ferroelectrics, and Frequency Control*, vol. 41, pp. 314–325, May 1994.

[4] J. Ophir, I. Cespedes, H. Ponnekanti, Y. Yazdi, and X. Li, "Elastography: A quantitative method for imaging the elasticity of biological tissues," *Ultrasonic Imaging*, vol. 13, pp. 111–134, 1991.

[5] A. Gent and P. Lindley, "The compression of bonded rubber blocks," *Proc. Institution of Mechanical Engineers*, vol. 173, no. 3, pp. 111–122, 1959.

[6] R. Segars, R. Hamel, and J. Kapsalis, "A punch and die test cell for determining the textural qualities of meat," *Journal of Texture Studies*, vol. 6, pp. 211–225, 1975.

[7] M. Bourne, "Texture profile analysis," *Food Technology*, vol. 32, pp. 62–72, July 1978.

[8] D. Hamann, C. Calkins, and C. Hollingsworth, "Instrumental texture measurements for processed meat products," in *Proc. 40th Reciprocal Meat Conference*, vol. 40, pp. 19–23, American Meat Science Association, 1987.

[9] W. Henry, M. Katz, F. Pilgrim, and A. May, "Texture of semi-solid foods: Sensory and physical correlates," *Journal of Food Science*, vol. 36, pp. 155–161, 1971.

[10] J. Ophir, R. Miller, H. Ponnekanti, I. Cespedes, and A. Whittaker, "Elastography of beef muscle," *Meat Science*, vol. 36, pp. 239–250, 1994.

[11] I. Hein, J. Novakofski, and W. D. O'Brien, Jr., "Ultrasound data acquisition system design for collecting high quality rf data from beef carcasses in the slaughterhouse environment," in *Proc. IEEE Ultrasonics, Ferroelectrics, and Frequency Control*, vol. 2, pp. 1039–1043, IEEE, 1991. Tucson, Az.

[12] V. Amin, D. Wilson, R. Roberts, and G. Rouse, "Tissue characterization for beef grading using texture analysis of ultrasonic images," in *Proc. IEEE Ultrasonics, Ferroelectrics, and Frequency Control*, vol. 2, pp. 969–972, IEEE, 1993. Baltimore, MD.

[13] T. Bakke, "A new mechanical instrument for the measurement of fibro-elasticity, with special reference to its use in the assessment of the consistency of the uterine cervix," *Acta Obstet Gynec Scand*, vol. 52, pp. 277–287, 1973.

[14] E. Krokosky and T. Krouskop, "The determination of the constitutive relationships for the human aorta," *J. Biomed. Mater. Res.*, vol. 4, pp. 525–547, 1970.

[15] E. Feigl, L. Peterson, and A. Jones, "Mechanical and chemical properties of arteries in experimental hypertension," *Journal of Clinical Investigation*, vol. 42, no. 10, pp. 1640–1647, 1963.

[16] R. Carton, J. Clark, J. Dainauskas, and A. Barron, "Estimation of tissue elasticity of the lung," *Applied Physiology*, vol. 19, no. 2, pp. 236–242, 1964.

[17] E. D'Angelo, "Stress-strain relationships during uniform and non-uniform expansion of isolated lungs," *Respiration Physiology*, vol. 23, pp. 87–107, 1975.

[18] M. Mridha and S. Odman, "Noninvasive method for the assessement of subcutaneous oedema," *Medical and Biological Engineering and Computing*, vol. 24, pp. 393–398, 1986.

[19] W. Hayes and L. Mockros, "Viscoelastic properties of human articular cartilage," *Journal of Applied Physiology*, vol. 31, no. 4, pp. 562–568, 1971.

[20] H. Stewart, H. Stewart, and K. Moore, "Compilation of reported biological effects data and ultrasound exposure levels," *Journal of Clinical Ultrasound*, vol. 13, p. 167, 1985.

[21] M. Ziskin and D. Petitti, "Epidemiology of human exposure to ultrasound: A critical review," *Ultrasound in Medicine and Biology*, vol. 14, p. 91, 1988.

[22] N. C. on Radiation Protocal and Measurement, "Exposure criteria for medical diagnostic ultrasound: I. criteria based on thermal mechanisms." Technical Report, June 1 1992. NCRP Rep No. 113.

[23] H. Socherek, *Medicine's New Vision.* Eaton, PA: Mack Publishing, 1988.

[24] A. Green, M. Modic, and N. Steinmetz, "Should you be using MRI?," *Patient Care*, pp. 26–37, Jan 30 1987.

[25] I. Pave, "High-tech tests that don't make you wince," *Business Week*, p. 164, May 9, 1988.

[26] K. Parker, S. Huang, R. Musulin, and R. Lerner, "Tissue response to mechanical vibrations for sonoelasticity imaging," *Ultrasound in Medicine and Biology*, vol. 16, no. 3, pp. 241–246, 1990.

[27] R. Lerner, S. Huang, and K. Parker, "Sonoelasticity images derived from ultrasound signals in mechanically vibrated tissues," *Ultrasound in Medicine and Biology*, vol. 16, no. 3, pp. 231–239, 1990.

[28] J. Holen, R. Waag, and R. Gramiak, "Representations of rapidly oscillating structures on doppler display," *Ultrasound in Medicine and Biology*, vol. 11, no. 2, pp. 267–272, 1985.

[29] J. Hermand, R. Lerner, S. Huang, and K. Parker, "Doppler shift techniques for speed of sound measurements and sonoelasticity images," in *Proc. 13th International Symposium on Ultrasonic Imaging and Tissue Characterization* (A. P. Inc, ed.), Linzer, 1988.

[30] S. Goss, R. Johnston, and F. Dunn, "Comprehensive compilation of empirical ultrasonic properties of mammalian tissues," *Journal Acoustical Society of America*, vol. 64, pp. 423–457, Aug 1978.

[31] I. Cespedes, J. Ophir, H. Ponnekanti, and N. Maklad, "Elastography: Elasticity imaging using ultrasound with application to muscle and breast in vivo," *Ultrasonic Imaging*, vol. 15, pp. 73–88, 1993.

[32] A. Skovoroda, S. Emelianov, M. Lubinksi, A. Sarvazyan, and M. O'Donnell, "Theoretical analysis and verification of ultrasound displacement and strain imaging," *IEEE Transactions Ultrasonics, Ferroelectrics, and Frequency Control*, vol. 41, pp. 302–313, May 1994.

[33] R. Dickinson and C. Hill, "Measurement of soft tissue motion using correlation between a-scans," *Ultrasound in Medicine and Biology*, vol. 8, pp. 263–271, Sept 1981.

[34] G. Trahey, S. Hubbard, and O. von Ramm, "Angle independent ultrasonic blood flow detection by frame-to-frame correlation of b-mode images," *Ultrasonics*, vol. 26, pp. 271–276, Sept 1988.

[35] E. Chen, W. Jenkins, and W. D. O'Brien, Jr., "Accuracy and precision of estimating tissue displacements from ultrasonic images," in *Proc. IEEE Ultrasonics Symposium*, vol. 2, pp. 1069–1072, IEEE Ultrasonics, Ferroelectrics, and Frequency Control, November 1992. Tucson, AZ.

[36] E. Chen, *Uncertainty in estimating tissue motion from ultrasonic images.* M.S. Thesis, University of Illinois, 1992.

[37] H. Adler and E. Roessler, *Introduction to Probability and Statistics.* San Francisco: Freeman and Co., 1962.

[38] J. Chen, W. Jenkins, I. Hein, and W. D. O. Jr, "Design of a residue number system digital correlator for real-time processing in ultrasonic blood flow measurements," in *Proc. IEEE Int. Symp. Circuits and Systems*, pp. 208–211, IEEE, 1989.

[39] E. Chen, I. Hein, R. Adler, P. Carson, and W. D. O'Brien, Jr., "A comparison of the motion tracking of ultrasonic b-mode tissue images with a calibrated phantom," in *Proc. IEEE Ultrasonics Symposium*, vol. 2, pp. 1211–1214, IEEE Ultrasonics, Ferroelectrics, and Frequency Control, October 1991. Orlando, FL.

[40] S. Foster, P. Embree, and W. D. O. Jr., "Flow velocity profile via time-domain correlation: Error analysis and computer simulation," *IEEE Transactions on Ultrasonics, Ferroelectrics, and Frequency Control*, vol. 37, no. 2, pp. 164–175, 1990.

[41] R. Wagner, S. Smith, J. Sandrik, and H. Lopez, "Statistics of speckle in ultrasonic b-scans," *IEEE Transactions on Ultrasonics, Ferroelectrics, and Frequency Control*, vol. 30, no. 3, pp. 156–163, 1985.

[42] E. Chen, W. Jenkins, and W. D. O'Brien, Jr., "The impact of various imaging parameters on ultrasonic displacement and velocity estimates," *IEEE Transactions on Ultrasonics, Ferroelectrics, and Frequency Control*, vol. 41, pp. 293–301, May 1994.

[43] B. Ramamurthy and G. Trahey, "Potential and limitations of angle-independent flow detection algorithms using radio frequency and detected echo signals," *Ultrasonic Imaging*, vol. 13, pp. 252–268, 1991.

[44] I. Hein and W. D. O'Brien, Jr., "Current time-domain methods for assessing tissue motion by analysis from reflected ultrasound echoes: A review," *IEEE Transactions on Ultrasonics, Ferroelectrics, and Frequency Control*, vol. 40, pp. 84–102, Mar 1993.

[45] M. O'Donnell and W. E. Engeler, "Correlation-based phase aberration correction in the presence of missing elements," *IEEE Transactions on Ultrasonics, Ferroelectrics, and Frequency Control*, vol. 39, no. 6, pp. 700–707, 1992.

[46] G. Trahey, S. Smith, and O. von Ramm, "Speckle pattern correlation with lateral aperture translation: Experimental results and implications for spatial compounding," *IEEE Transactions on Ultrasonics, Ferroelectrics, and Frequency Control*, vol. 33, pp. 257–264, May 1986.

[47] N. Smith, "Ultrasonic exposimetry system," tech. rep., Bioacoustics Research Laboratory, University of Illinois at Urbana-Champaign, 1995. Beckman Institute Technical Report.

[48] P. D. Jong, T. Arts, A. Hoeks, and R. Renman, "Experimental evaluation of the correlation interpolation technique to measure regional tissue velocity," *Ultrasonic Imaging*, vol. 13, pp. 145–161, 1991.

[49] W. Andrews, *Liver*. New York: Edward Arnold, 1979.

[50] T. Hargreaves, *The Liver and Bile Metabolism*. Des Moines: Meredith Corporation, 1968.

[51] H. Popper and F. Schaffner, *Liver Structure and Function.* New York: McGraw-Hill, 1957.

[52] H. Elias and J. Sherrick, *Morphology of the Liver.* New York: Academic Press Inc, 1969.

[53] R. Berne and M. Levy, *Principles of Physiology.* St. Louis: C.V. Mosby Company, 1990.

[54] A. Varder, J. Sherman, and D. Luciano, *Human Physiology.* New York: McGraw-Hill, 1985.

[55] B. Alberts, D. Bray, J. Lewis, M. Raff, K. Roberts, and J. Watson, *Molecular Biology of the Cell.* New York-London: Garland Publishing, 1989.

[56] B. Hete and K. Shung, "Scattering of ultrasound from skeletal muscle tissue," *IEEE Transactions on Ultrasonics, Ferroelectrics, and Frequency Control*, vol. 40, pp. 354–365, July 1993.

[57] S. Goss, R. Johnston, and F. Dunn, "Comprehensive compilation of empirical ultrasonic properties of mammalian tissues ii," *Journal Acoustical Society of America*, vol. 68, pp. 93–108, July 1980.

[58] R. Wagner, M. Insana, and S. Smith, "Fundamental correlation lengths of coherent speckle in medical ultrasonic images," *IEEE Transactions on Ultrasonics, Ferroelectrics, and Frequency Control*, vol. 35, pp. 34–44, January 1988.

[59] Y. Fung, *Biomechanics: Mechanical Properties of Living Tissues.* New York: Springer-Verlag, 1981.

[60] F. Silver, *Biological Materials: Structure, Mechanical Properties and Modeling of Soft Tissues.* New York: New York University Press, 1987.

[61] F. Beer and E.R. Johnston, Jr., *Mechanics of Materials.* New York: McGraw-Hill, 1981.

[62] American Cancer Society, "Cancer facts and figures." Technical Report, 1991.

[63] C. Kimme-Smith, "National cancer institute breast imaging workshop," *American Journal of Roentgenology*, vol. 158, p. 268, 1992.

[64] J. Martin, M. Moskowitz, and J. Milbrath, "Breast cancer missed by mammography," *American Journal of Roentgenology*, vol. 132, pp. 737–739, 1979.

[65] J. Berg, "Clinical implications of risk factors for breast cancer," *Cancer*, vol. 53, pp. 589–591, 1984.

[66] Z. Monostori, P. G. Herman, D. P. Carmody, T. M. Eacobacci, N. R. Capece, V. M. Cruz, S. Gentin, and F. M. Vernace, "Limitations in distinguishing malignant from benign lesions of the breast by systematic review of mammograms," *Surgery, Gynecology and Obstetrics*, vol. 173, pp. 438–442, Dec 1991.

[67] S. Ciatto, D. Morrone, S. Catarzi, M. R. D. Turco, S. Bianchi, D. Ambrogetti, and A. Cariddi, "Radial scars of the breast: Review of 38 consecutive mammographic diagnoses," *Radiology*, vol. 187, pp. 757–760, June 1993.

[68] K. N. Krecke and J. J. Gisvold, "Invasive lobular carcinoma of the breast: Mammographic findings and extent of disease at diagnosis in 184 patients," *American Journal of Roentgenology*, vol. 161, pp. 957–960, Nov 1993.

[69] E. Ueno, "Classification and diagnostic criteria in breast echography," *Jpn J Med Ultrasonics*, vol. 13, no. 1, pp. 19–31, 1986.

[70] E. Ueno, E. Tohno, S. Socda, Y. Asaoka, K. Itoh, J. Bamber, M. Blaszczyk, J. Davey, and J. McKinna, "Dynamic testing in real-time breast echography," *Ultrasound in Medicine and Biology*, vol. 14, pp. 53–57, 1988.

[71] W. Leucht, D. Rabe, and K. Humbert, "Diagnostic value of different interpretative criteria in real-time sonography of the breast," *Ultrasound in Medicine & Biology*, vol. 14, no. 1, pp. 59–73, 1988. Sup. 1.

[72] R. Adler, J. Rubin, P. Bland, and P. Carson, "Quantitative tissue motion analysis of digitized m-mode images: Gestational differences of fetal lung," *Ultrasound in Medicine & Biology*, vol. 16, no. 6, pp. 561–569, 1990.

[73] J. Fowlkes, S. Emelianov, A. Sarvazyan, A. Skovoroda, J. Pipe, R. Adler, and P. Carson, "Cancer detection using tissue elasticity imaging," 1995. submitted.

[74] A. Sarvazyan, A. Skovoroda, S. Emelianov, J. Fowlkes, J. Pipe, R. Adler, R. Buxton, and P. Carson, "Biophysical bases of elasticity imaging," *Acoustical Imaging*, 1995. in press.

[75] A. Skovoroda, S. Emelianov, M. Lubinksi, and M. O'Donnell, "Tissue elasticity reconstruction based on ultrasonic displacement and strain images," *IEEE Transactions Ultrasonics, Ferroelectrics, and Frequency Control*, 1995. submitted.

[76] M. Bertrand, J. Meunier, M. Doucet, and G. Ferland, "Ultrasonic biomechanical strain gauge based on speckle tracking," in *Proc. IEEE Ultrasonics Symposium*, vol. 2, pp. 859–863, IEEE Ultrasonics, Ferroelectrics, and Frequency Control, 1989.

[77] E. Chen, W. Jenkins, and W. D. O'Brien, Jr., "Biomechanical measurements of soft tissues with application to elasticity imaging," *IEEE Transactions on Ultrasonics, Ferroelectrics, and Frequency Control*, 1995. in press.

[78] E. Chen and M. Shin, "Measurement of tissue mechanical properties," tech. rep., Bioacoustics Research Laboratory, University of Illinois at Urbana-Champaign, 1995. Beckman Institute Technical Report.

[79] E. Bagley, W. Wolf, and D. Christianson, "Effect of sample dimensions, lubrication and deformation rate on uniaxial compression of gelatin gels," *Rheologica Acta*, vol. 24, pp. 265–271, 1985.

[80] G. M. J. Meunier, M. Betrand and R. Petitclerc, "Local myocardial deformation computed from speckle motion," *Computers in Cardiology*, pp. 133–136, 1988.

[81] P. Laugier and G. Berger, "Experimental results of ultrasonic monitoring of cryotherapy on in vitro skin samples of domestic pig," in *Proc. IEEE Ultrasonics, Ferroelectrics, and Frequency Control*, vol. 2, pp. 1045–1048, IEEE, 1992.

[82] L. Ryan, G. Lockwood, B. Starkoski, D. Holdsworth, D. Rickey, M. Drangova, A. Fenster, and F. Foster, "A high frequency intravascular imaging system for investigation of vessel wall properties," in *Proc. IEEE Ultrasonics Symposium*, vol. 2, pp. 1101–1105, IEEE Ultrasonics, Ferroelectrics, and Frequency Control, 1992. Tucson, AZ.

[83] A. Saada, *Elasticity, Theory and Applications.* New York: New York Pergamon Press, 1974. 395-428.

[84] I. Cespedes and J. Ophir, "Axial stress distributions between coaxial compressors in elastography: An analytical model," *Ultrasonic Imaging*, vol. 18, no. 8, pp. 667–673, 1992.

[85] T. Stedman, *Stedman's Medical Dictionary.* Williams and Wilkins, 25th ed., 1990.

[86] W. D. O'Brien, Jr., E. Chen, and W. Jenkins, "Accuracy, limits and tradeoffs in ultrasound displacement measurements and their implication to elasticity imaging," in *Proc. Acoustical Imaging Congress*, June 1995. Norway.

[87] J. Bendat and A. Pierson, *Random Data: Analysis and Measurement.* Wiley, 2nd ed., 1986.

[88] W. Walker and G. Trahey, "A fundamental limit on delay estimation using partially correlated speckle signals," *IEEE Transactions on Ultrasonics, Ferroelectrics, and Frequency Control*, vol. 42, pp. 301–308, Mar 1995.

[89] M. Parilla, J. Anaya, and C. Fritsch, "Digital signal processing techniques for high accuracy ultrasonic range measurements," *IEEE Transactions on Instrumentation and Measurement*, vol. 40, no. 4, pp. 759–763, 1991.

[90] I. Cespedes and J. Ophir, "Reduction of image noise in elastography," *Ultrasonic Imaging*, vol. 15, pp. 89–102, 1993.

[91] E. Chen, J. Novakofski, W. Jenkins, and W. D. O'Brien, Jr., "Ultrasound elasticity measurements of beef muscle," in *Proc. IEEE Ultrasonics Symposium*, vol. 3, pp. 1459–1462, IEEE Ultrasonics, Ferroelectrics, and Frequency Control, Nov 1994. Cannes, France.

[92] E. Chen, W. Jenkins, and W. D. O'Brien, Jr., "Performance of ultrasonic speckle tracking in various tissues," *Journal of the Acoustical Society of America*, Aug 1995. in press.

[93] E. Chen, R. Adler, P. Carson, W. Jenkins, and W. D. O'Brien, Jr., "Quantitative motion analysis of breast tumor motion," in *Proc. IEEE Ultrasonics Symposium*, IEEE Ultrasonics, Ferroelectrics, and Frequency Control, Nov 1995. (submitted) Seattle, WA.

VITA

Eric Chung-Jay Chen received the B.S. and M.S. degrees in Electrical Engineering in 1990 and 1992 from the University of Illinois. From 1990 to 1992 Mr. Chen was a network and computer systems administrator at the Coordinated Sciences Research Laboratory at the University of Illinois. In 1991, he was awarded a 3 year National Institutes of Health Radiation Oncology Trainee Fellowship. In the summer of 1993, Mr. Chen worked in the biomedical sciences division at Lawrence Livermore National Laboratory where he developed image analysis and visualization software for computer-aided-diagnosis of high resolution digital mammograms. From 1992-1995 Mr. Chen worked towards his doctorate in electrical engineering at the University of Illinois where he was a research and teaching assistant in the Bioacoustics Research Laboratory and in the digital signal processing group in the Coordinated Sciences Laboratory. His research interests include signal processing, medical imaging including MRI, CT, ultrasound, radar imaging and sonar. Mr. Chen has published 10 journal and conference papers in these areas.